ISTITUTO NAZIONALE DI FISICA NUCLEARE

ICARUS-85/01

INFN/AE-85/7
September 1985

SEARCHING FOR NEW UNDERGROUND PHENOMENA WITH HIGH RESOLUTION VISUAL TECHNIQUES AND MAGNETIC ANALYSIS

(ICARUS)

A PROPOSAL
FOR THE GRAN SASSO LABORATORY

CERN - Harvard - Milano - Padova - Roma - Tokyo - Wisconsin

Collaboration

SEARCHING FOR NEW UNDERGROUND PHENOMENA WITH HIGH RESOLUTION VISUAL TECHNIQUES AND MAGNETIC ANALYSIS

(ICARUS)

A PROPOSAL

FOR THE GRAN SASSO LABORATORY

CERN - Harvard - Milano - Padova - Roma - Tokyo - Wisconsin
Collaboration

IMAGING

COSMIC

AND

RARE

UNDERGROUND

SIGNALS

Abstract

We propose a very large volume (>4500 m^3) Liquid Argon or Methane homogeneous detector, fully and **continuously sensitive,** capable of bubble chamber quality images of spatial separation of about $1mm^3$ and operated in a **magnetic field.** The detector relies on a novel technique which we have developed during the last years of achieving very high purity liquids (< 1ppb of O_2 equivalent), in which electrons remain untrapped for periods of time in excess of one millisecond. Ionization electrons are collected over a two meter long path and they are sensed by three planes of collecting wires, which record a three-view **bubble chamber quality image** of all ionizing events occurring inside the chamber. The detector is self-triggering. Unlike a bubble chamber, ionization losses along the particle paths are accurately recorded, adding to the features of the high spatial resolution and of the magnetic field the possibility of **an accurate calorimetry** and of an **unambiguous K, π and μ separation** of slow or stopping particles. The experiment is intended to explore a large number of different phenomena, related both to elementary particle Physics and to Astrophysics, namely :

(1) **energetic muon(s)** entering from the walls of the cave, either produced in the atmosphere or by neutrino interactions in the rock;

(2) **neutrino interactions** in the detector volume;

(3) decay mode independant **nucleon instability;**

(4) **solar neutrinos, distant nuclear reactors, and galactic (anti)neutrinos** in the few MeV region;

(5) **monopoles and other similar exotica,** should they ever occur.

Participating Institutions.

At the present, the following Institutions are engaged in the realization of the proposed detector:

Institution	Address	Contact People (*)
1. **CERN**	Geneva, Switzerland	D. Schinzel
2. **Harvard**	HEPL Harvard University Cambridge, MA, 02138 USA	E. Aprile, K.L. Giboni
3. **Milano**	Dip. di Fisica dell'Università and Sezione dell'INFN Università di Milano, Milano, Italy	G. Bellini
4. **Padova**	Istituto di Fisica and Sezione dell'INFN Università di Padova, Padova, Italy	S. Centro, M. Baldo Ceolin
5. **Roma**	Dip. di Fisica dell'Università and Sezione dell'INFN Università "La Sapienza", Roma, Italy	M. Conversi, F. Massa
6. **Tokyo**	Cosmic Ray Research University of Tokyo, Tokyo, Japan	Y. Muraki
7. **Wisconsin**	Physics Department Univ. of Wisconsin, Madison, WI, 53706 USA	D. Cline, T. Smart

(*) The scientific spokesman is **C. Rubbia** , CERN/Harvard

Table of Contents.

1.-Introduction.

Since the initial proposal$^{1)}$ of a Liquid Argon Drift Chamber put forward by one of us in 1977, a large amount of work has been carried out at Harvard $^{2)}$ and elsewhere $^{3)}$ in order to ascertain the feasibility of the method and in particular in order to develop the technology of attaining the degree of purity ($<<1$ppb of O_2 equivalent) necessary to drift electrons over several meters in Liquid Argon or Methane. Much progress has been made (see Appendix II) and we believe that the technology needed to build a very large scale device is now at hand. A very simple purification technique, namely a commercial Oxisorb or equivalent device to remove Oxygen, followed by molecular sieves at low temperature in order to remove other polar impurities is largely sufficient to obtain (Fig.1) an Argon gas which, once

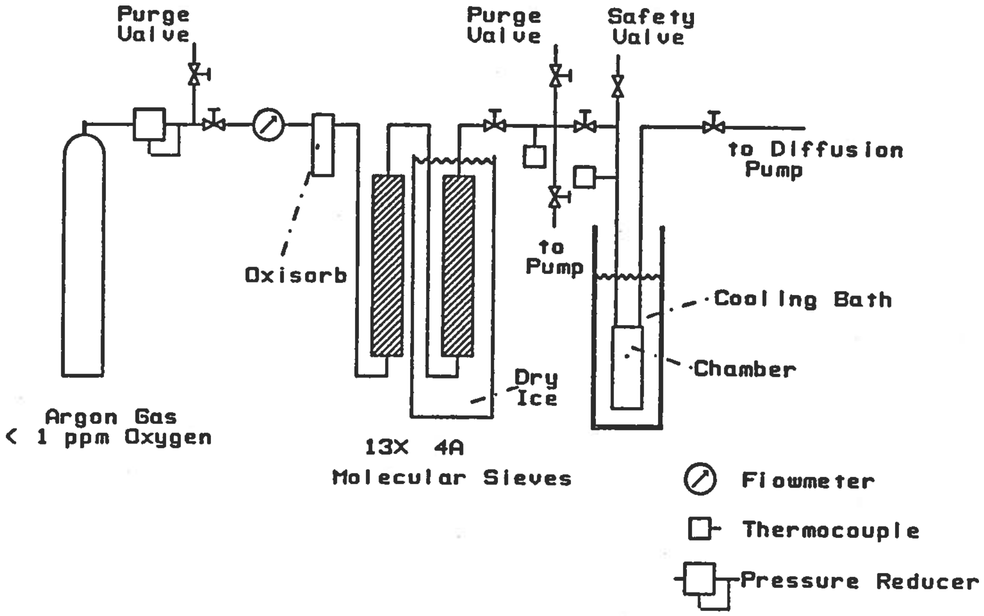

Figure 1. Gas purification system to achieve Argon purities in excess of 0.3 ppb Oxygen equivalent. From Ref. 2 and Appendix II.

liquefied, exibits consistently very long drift paths of electrons. This is obviously due to the fortunate fact, that at Liquid Argon temperature, most of the harmful impurities are frozen. The attenuation length for free electrons is to an excellent approximation proportional to the drift speed, namely to the strength of the electric field. This is evidenced in Fig. 2a, where one can see that already at fields of the order of 150 Volt/cm we observe an attenuation length of the order of 160 cm. Since the detector can operate with electric fields of the of order of 1.0 kV/cm, **attenuation lenghts well in excess of 10 meters are achievable.** This has lead to the choice in the present proposal of a maximum electron drift length of 2.3 meters at 1 kV/cm.

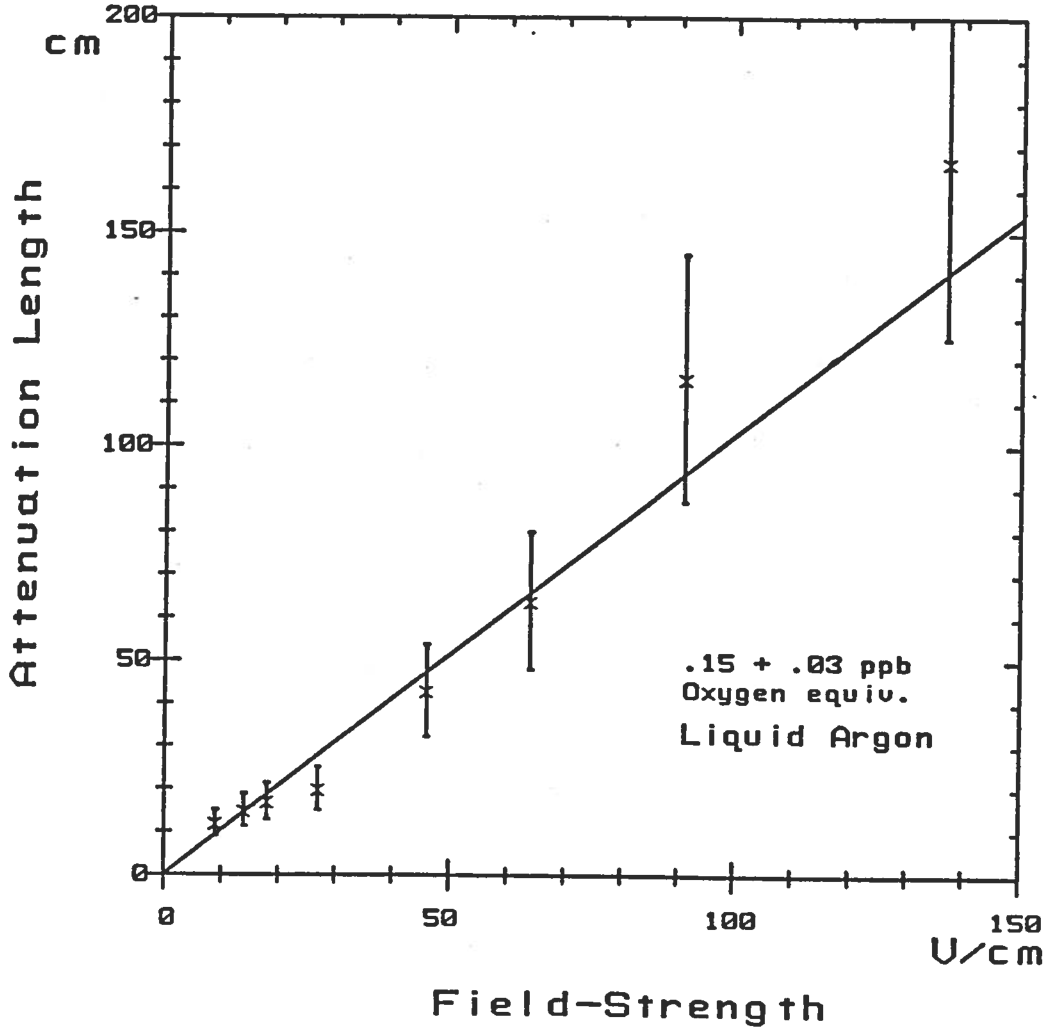

Figure 2a. Attenuation length for free electron in Argon, as a function of the drift field. Note that the extrapolation to the field of about 1.0 KV/cm, the attenuation length approaches 10 meters (Ref. 2).

On the basis of these technical advances we propose the realization of a very large volume (> **4500 m^3**) of Liquid Argon which is **continuously sensitive** and capable of bubble chamber quality images with a spatial **track separation** of about 2 mm. Work in progress at Harvard has shown that also Liquid **Methane,** as well as **Methane-Argon mixtures** (Fig. 2b and Fig 2c) are possible. This will provide an important ingredient, namely **free Hydrogen.** Free protons are an ideal target for low energy **antineutrinos** , which undergo the classic reaction:

$$\bar{\nu}_e + p \longrightarrow n + e^+$$

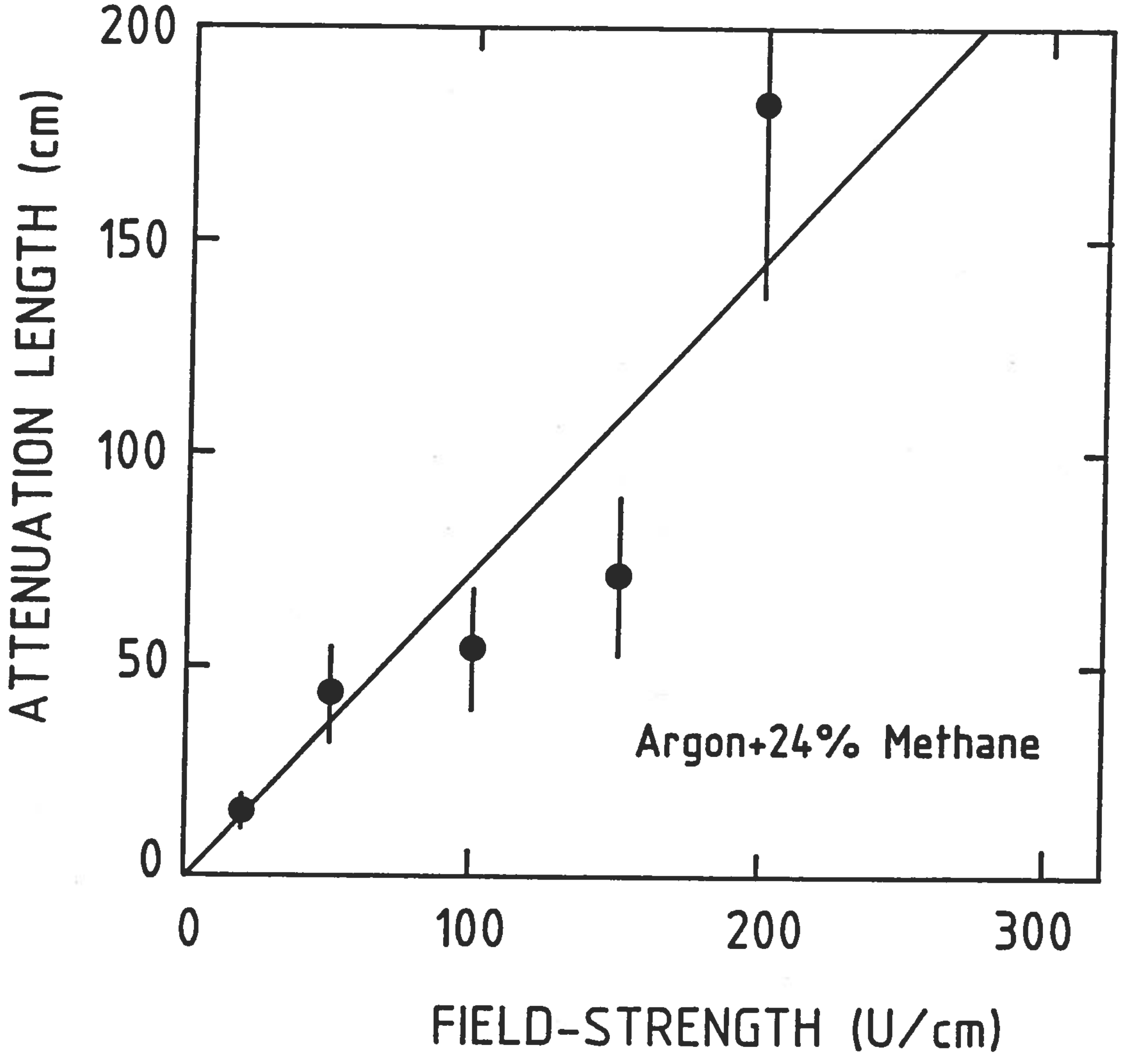

Figure 2b. Attenuation length for free electron in Argon-24% Methane mixture, as a function of the drift field. Note that the extrapolation to the field of about 1.0 KV/cm, the attenuation length approaches 6 meters.

Bound Nucleons have little or no cross section at low energies because of Pauli exclusion principle of the final neutron state and the nuclear binding threshold. The signature of the process is further improved by the positron annihilation and the (delayed) neutron capture by free protons. Equally important is the role of the free hydrogen in the search for **proton decay**. The decay of **free** protons, being unaffected by the Fermi motion and the secondary interactions with the rest of the nucleons, is perfectly matched to the extremely good angle and energy resolution (~2% at 1 Gev) of the cryogenic image chamber. Low energy **neutrinos**, as opposed to antineutrinos, have a large cross section on **neutrons.** We are considering the exciting possibility of even a partial fill with **Deuterated Methane**

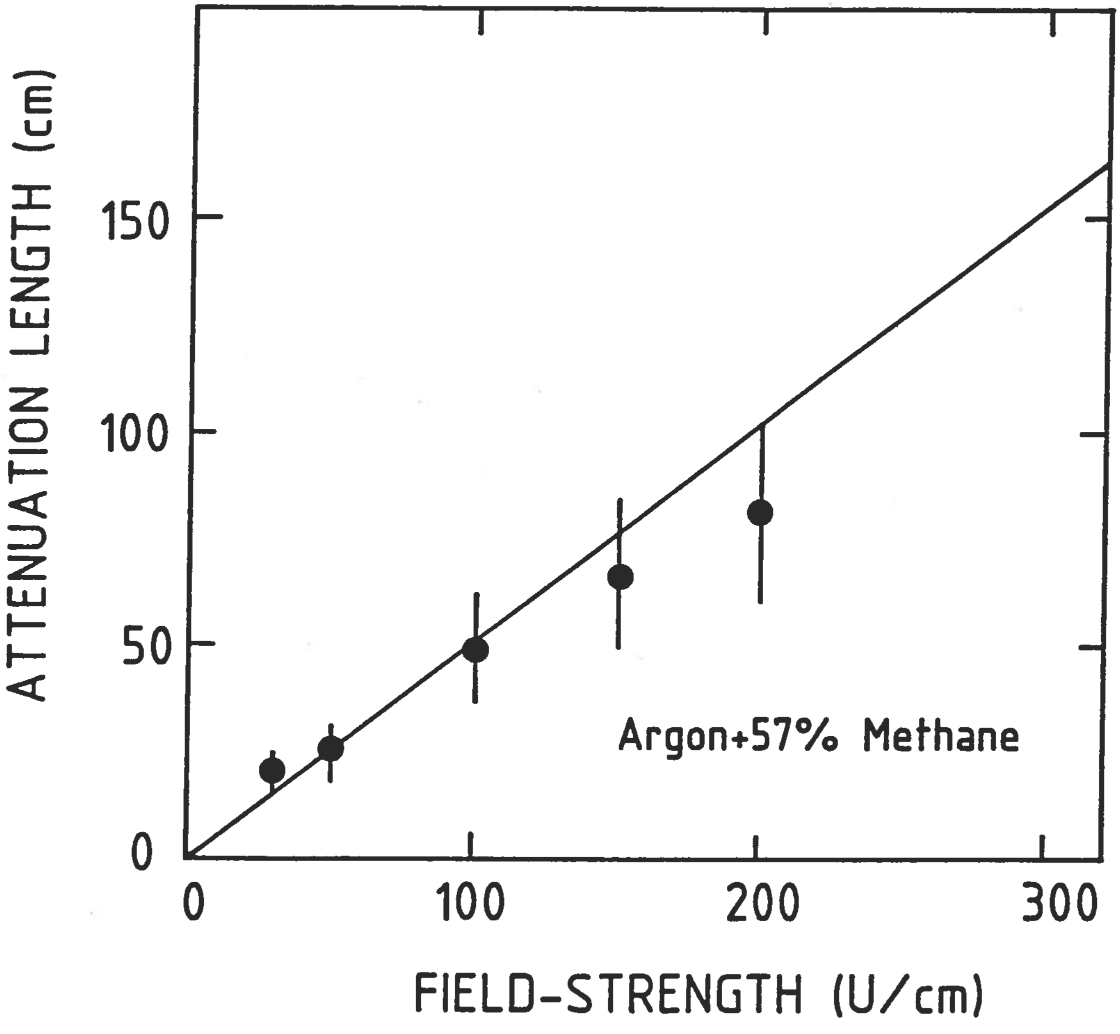

Figure 2c. Attenuation length for free electron in Argon-57% Methane mixture, as a function of the drift field. Note that the extrapolation to the field of about 1.0 kV/cm, the attenuation length approaches 6 meters.

mixed to Argon. Several hundred tons of heavy water are necessary to provide a meaningful amount of target. Such a large stockpile exists at present in Canada. The possibility of a loan is being investigated.

We propose to add to the cryogenic image chamber a gigantic **solenoid** of 15 m diameter and 25 m long, in order to generate an uniform **magnetic field** of 0.5 Tesla over the whole sensitive volume of the detector. The magnetic field permits for the first time the realization of a large acceptance underground detector capable of an accurate momentum determination of all tracks produced inside the sensitive volume or coming from the outside .

The **Gran Sasso Laboratory**4) provides an unique opportunity for the kind of apparatus proposed here, since it permits easy access for detector components of very large sizes and weight. Dimensions of the facilities available in the halls planned or under construction are unprecedented for underground experiments and they are such as to permit for the first time to assemble and operate sophisticated detectors in conditions so far available only in well equipped laboratories, like for instance CERN. Finally the large spatial separation between the different halls and the availability during operation with cryogenic liquids of an access tunnel and a wide exhaust pipeline totally independent of the road tunnel insures the **perfectly safe handling of huge amounts of cryogenic liquids** underground (see Appendix I) .

2.- Physics potentials of cryogenic image chamber.

The cryogenic image chamber proposed here has very unique features which are worth a detailed discussion. The drift-time technique and the continuous read-out permit to **record the complete electron image** produced by the ionizing event. In this respect, this device resembles very much a **bubble chamber**. The apparent "bubble" size, namely the size of an initial δ-function of electrons in the liquid, is determined by the diffusion of the electrons due to the drift time and to the intrinsic time and space resolution of the read-out. The resultant "bubble" size is of approximately 1 mm radius, quite similar to the performance of the famous Gargamelle bubble chamber. The centroid of the "bubble", can be determined much more accurately, since it involves interpolations of the timing and charge signals. Calculations5) in the case of an optimal noise-to-signal ratio show that resolutions of approximately 200 μm are achievable. However taking into account the actual conditions of the read-out, we prefer to take the more conservative value of 500 μm, mostly dominated by the noise in the input amplifier. The accuracy of the momentum measurement of charged tracks traversing the detector is primarily determined by measurement errors and multiple scattering. The radiation length of pure Argon is l_r = 14.0 cm, close to the one of heavy Freon, while the one of pure methane is as large as l_r = 73.0 cm. For a very high energy muon traversing the whole detector, the maximum detectable transverse momentum is given by the formula:

$$p_{max} = 0.037 \frac{l^2 B}{\sigma}$$

where l is the length of the particle track in the plane normal to the field in meters, σ is the error in the sagitta, conservatively set to 0.1 mm and B is the field in Tesla. For B= 0.5 T and l = 12 m we find the remarkable result, **p_{max}= 25 TeV.** Since the average muon momentum entering the apparatus is about 4 TeV, the momentum accuracy offered by the detector is in general very good. On the other end of the momentum scale in the case of slow tracks where multiple scattering is dominant, the momentum error is independent of the momentum $\Delta p/p = 0.24\ l^{-1/2}$, where l is the track length in meters. In the case of pure methane filling, the error is a factor 0.228 smaller, namely $\Delta p/p = 0.06\ l^{-1/2}$. Note that the collision length in Liquid Argon is quite short, namely 80.9 cm and therefore very long tracks are unlikely for hadrons.

The cryogenic image chamber, in contrast to the bubble chamber, (where ionization measurements are rather inaccurate), is also a superb **calorimeter.** The excellent quality of calorimetric measurements in a pure Argon calorimeter has been very extensively investigated, both with Montecarlo techniques 6) and experimentally 7). The resolution of low energy electrons and photons 6) is shown in Fig. 3 and it is well fitted (see Fig. 4) by a formula of the type: $\sigma/E = 0.0168\ E(GeV)^{-1/2}$, or about a 1.6% r.m.s. resolution at 1 GeV. Photons and electrons have quite similar behaviours.These predictions are well confirmed experimentally7), as shown in Fig. 5. The energy response, as anticipated, is perfectly linear, as shown in Fig. 6. Hadrons of significant energy normally undergo additional secondary interactions in the Argon (Fig. 7a). The energy response to such an hadronic cascade is equally good, as shown in Fig. 8. Finally it is possible to determine the angle of emission of a photon or an electron from a weighted average of the energy depositions of the electromagnetic cascade with good resolution, as shown in Fig. 9. The relative response 7) of the Argon calorimeter to fast tracks is quite independant

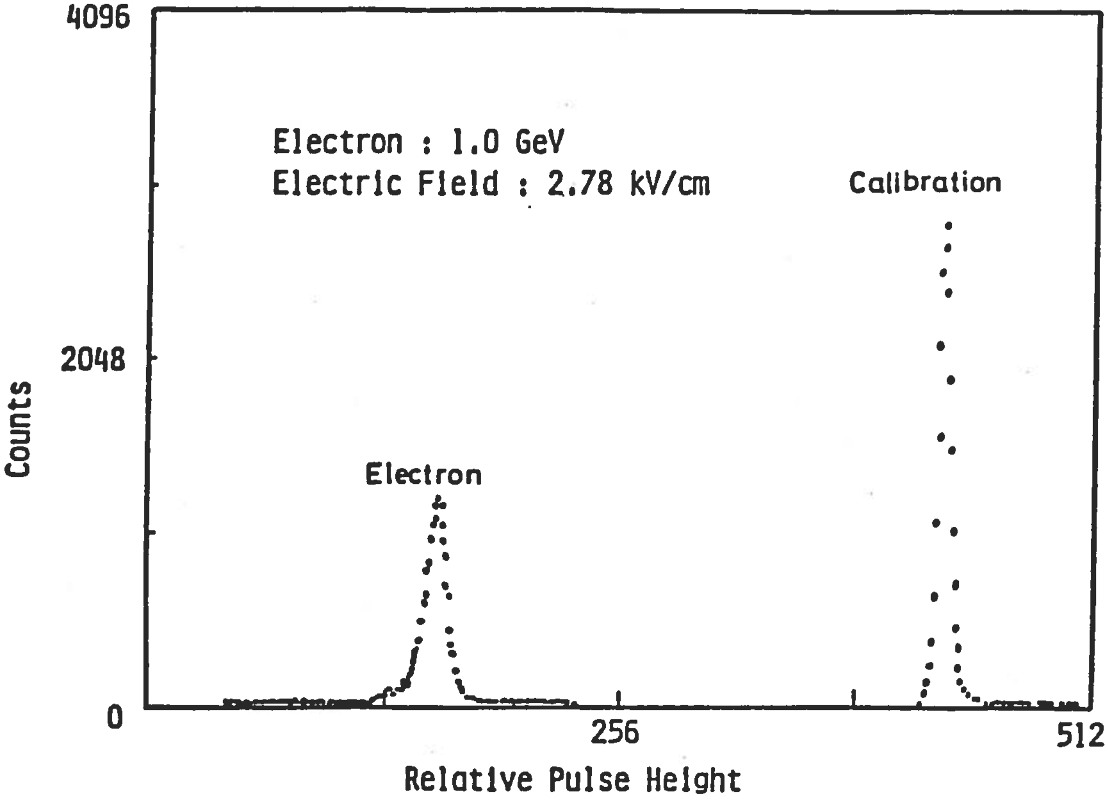

Figure 3. Experimental pulse height spectrum of 1 GeV/c electrons from the KEK accelerator in a total absorption pure Liquid Argon calorimeter[7].

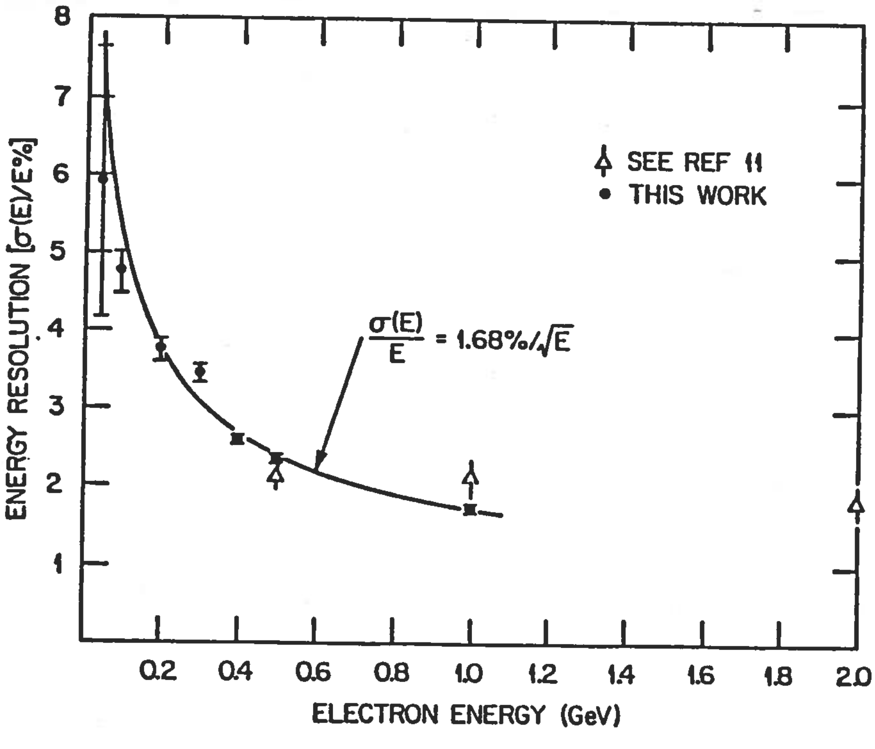

Figure 4. Expected Resolution, according to EGS Montecarlo for electrons in the energy range 50 MeV to 1 GeV, from Ref. 6. The data are well represented by an inverse square root law.

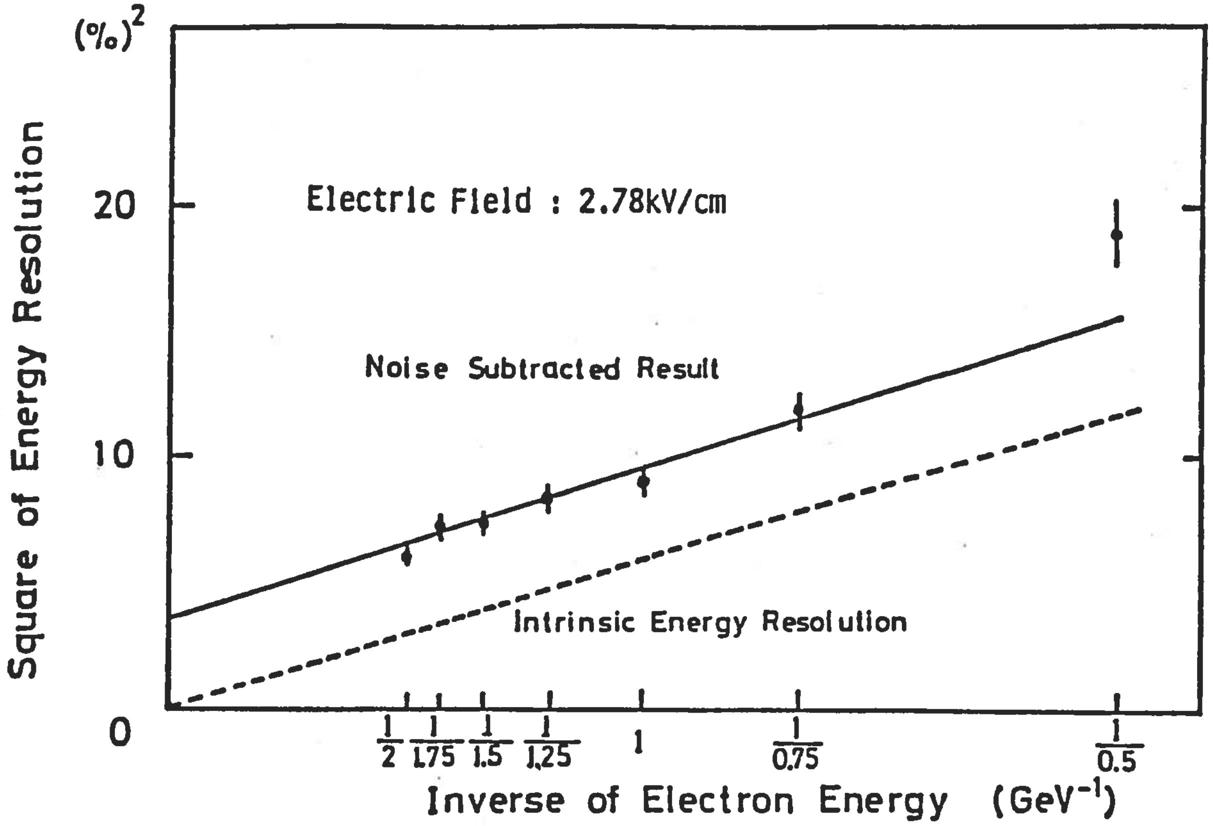

Figure 5. Experimental resolution for electrons in Liquid Argon$^{7)}$. Results are in qualitative agreement with the Montecarlo data after subtraction of electronic noise.

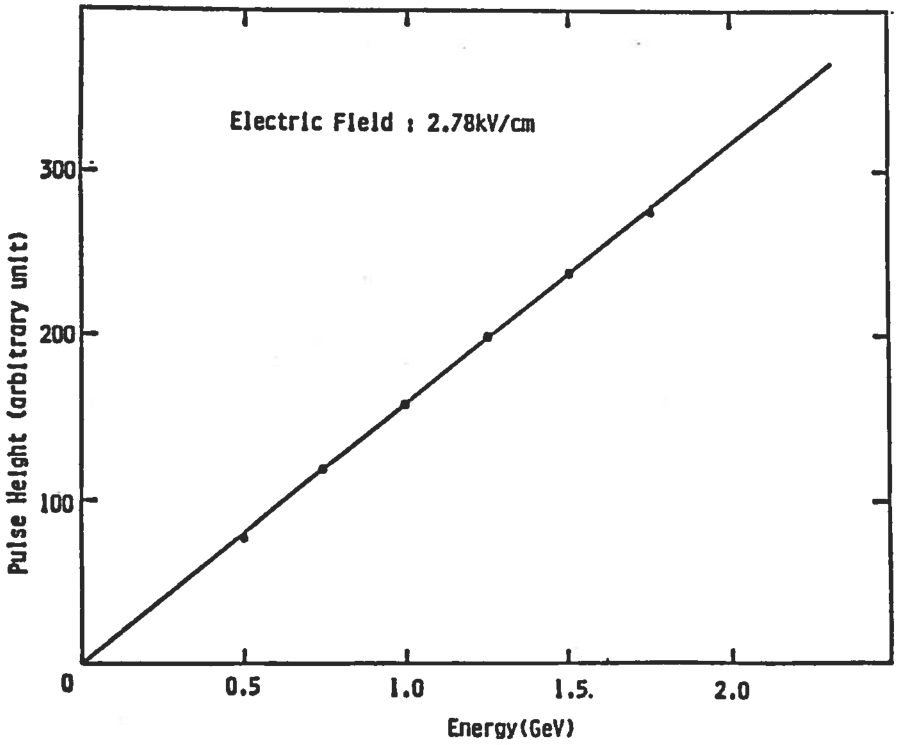

Figure 6. Experimental linearity of response of the pure Liquid Argon calorimeter$^{7)}$.

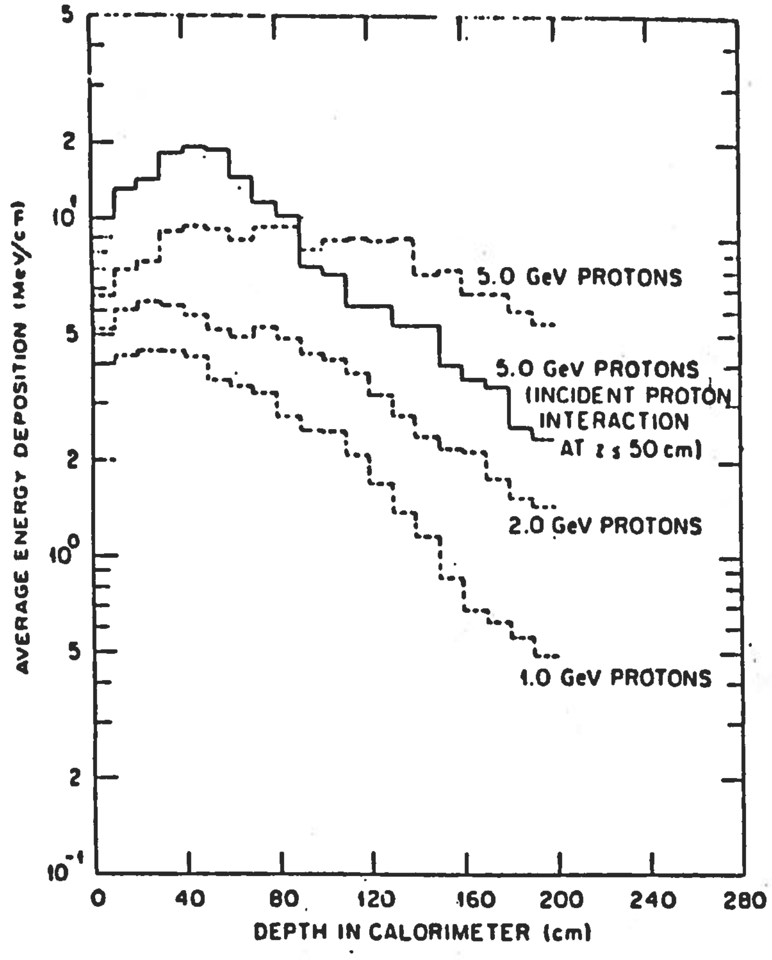

Figure 7a. Attenuation of hadronic cascade for hadrons (protons) of energy range 1 - 5 GeV, according to Montecarlo calculations[6].

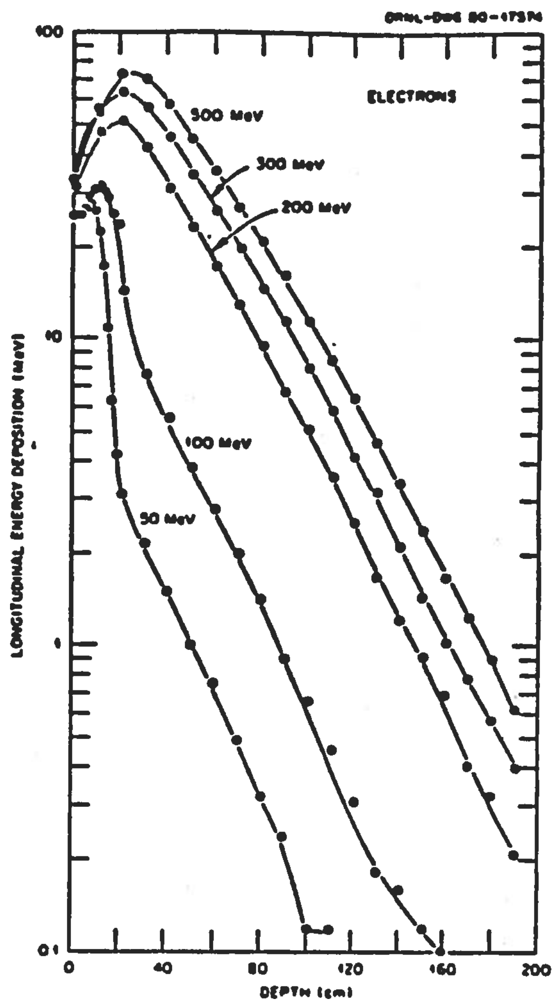

Figure 7b. Longitudinal energy deposition in Liquid Argon for electrons in the range 50 - 500 MeV[6].

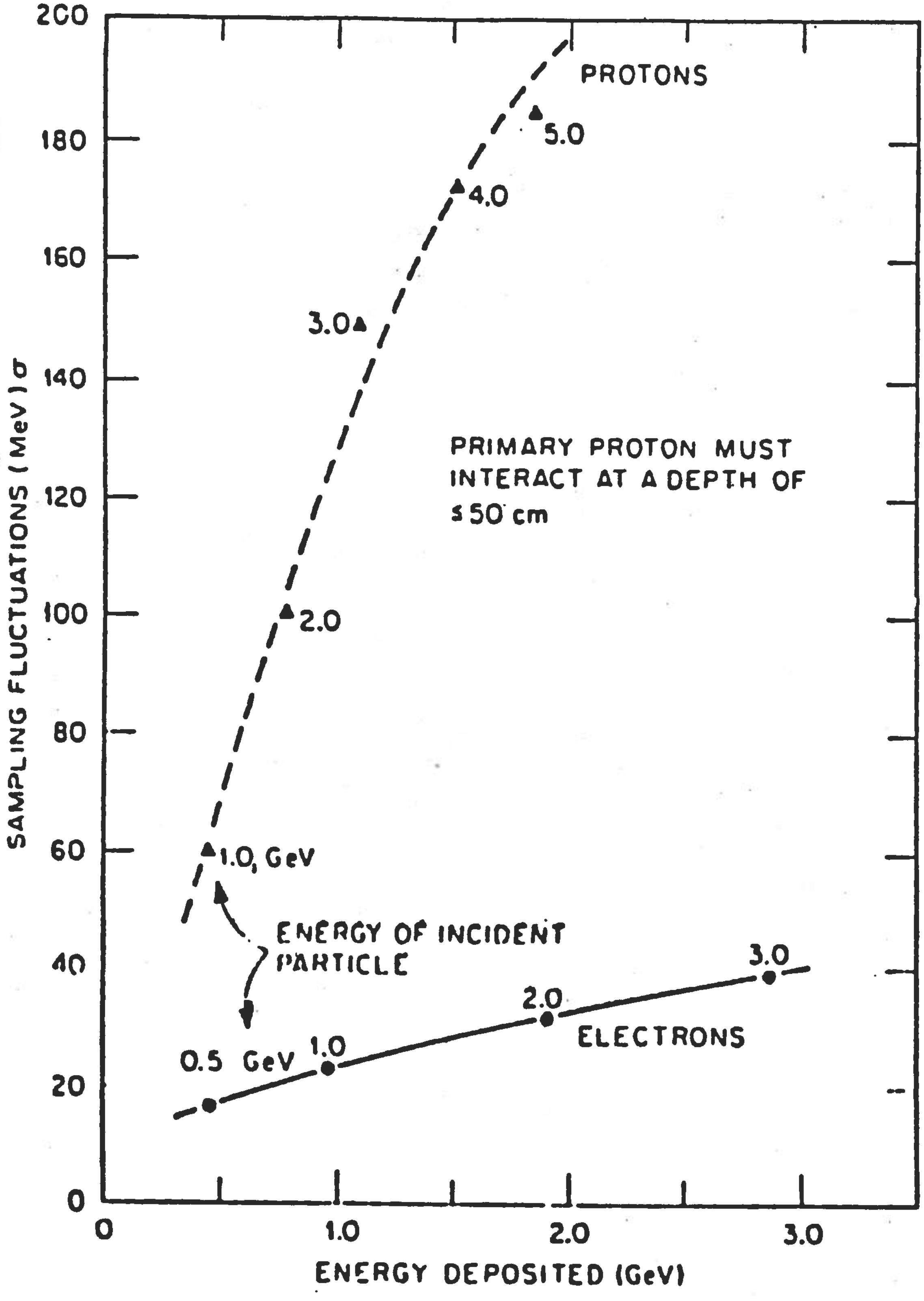

Figure 8. Sampling fluctuations for electrons and protons6).

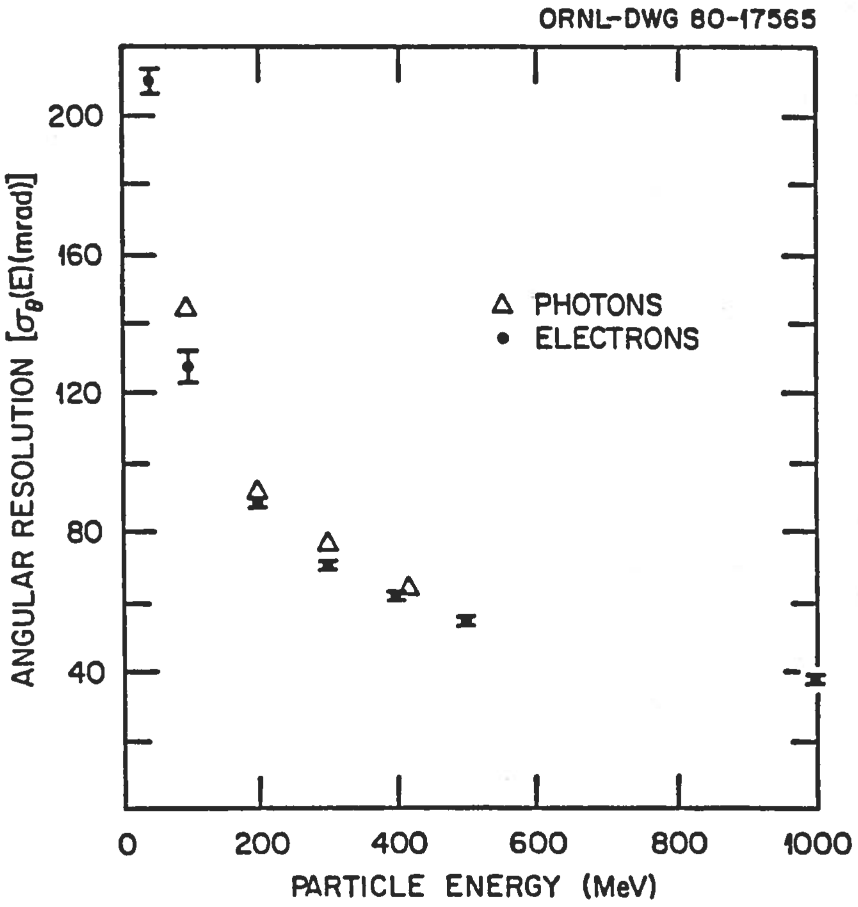

Figure 9. Angular resolution for photons and electrons, according to Montecarlo calculations[6].

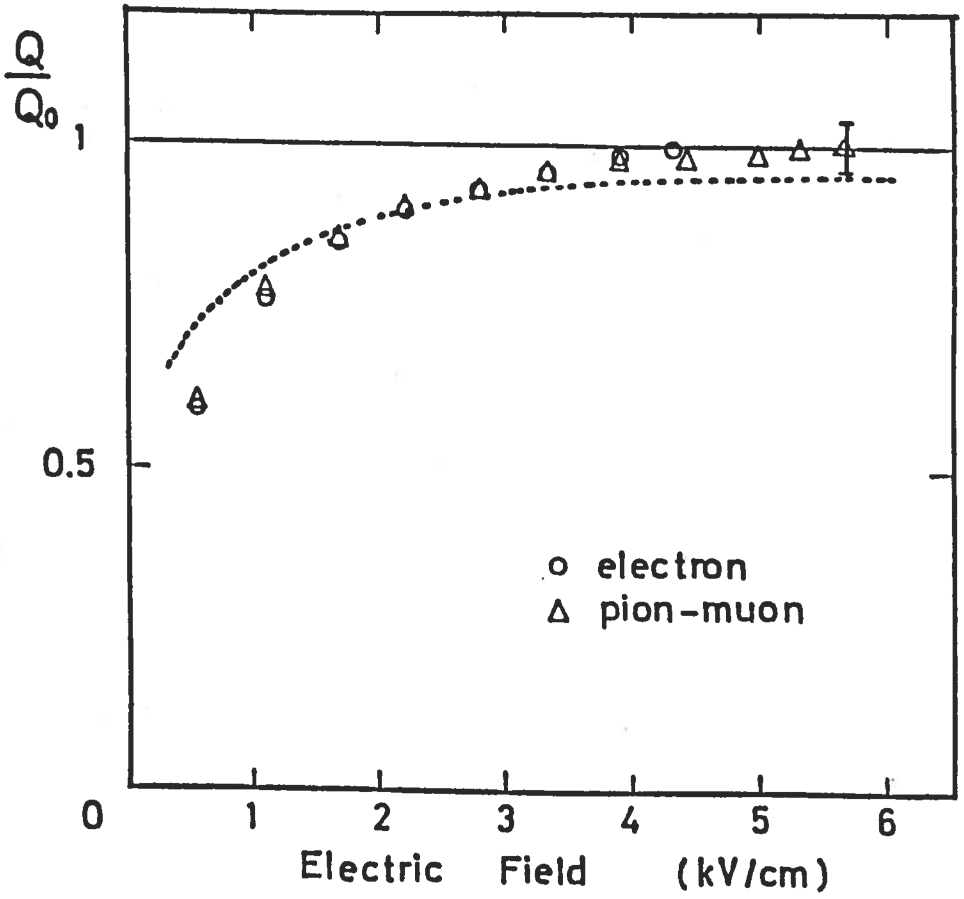

Figure 10. Normalized charge collection as function of the electric field for stopping e, μ, and π measured in the KEK beam[7].

of the strength of electric field used to collect the charges (Fig. 10). The drop of the collected charge for smaller values of the field is due to the effects of geminate recombination in the liquid.

Finally the possibility of measuring continuously the ionization along the track permits **the identification of the nature of the particle** with the help of the ionization vs. range relationship (Fig. 11). Separations between K and p are entirely trivial. Instead, π-μ distinction is marginal. However at end range pions and muons behave quite differently. It is worth mentioning that the time delay due to the μ - ϵ decay introduces a significant gap in the track of the decay electron because of the drift velocity effects, namely 2 mm/μs.

The main feature of our apparatus is the one of detecting **any ionizing phenomenon** occurring within its volume and above a given energy threshold. It appears reasonable to set the trigger threshold to about 4.0 to 5.0 MeV equivalent to minimum ionization. The extreme purity of the liquid needed by the detector and the fact that many different impurities freeze out at low temperature insures that the radioactive background is small and that the trigger rate is dominated by cosmic rays traversing the volume. Note that a relatively simple trigger processor can be used to select only pre-assigned regions of the detector volume. This is easily achieved, since the read-out is recording continuously the information from the detector storing it in a memory. Data are lost only when the event memory is overwritten by the newly produced coordinates. Using a generous memory size we can allow plenty of time for selecting the type of events of interest. Therefore the detector is essentially bias free and it detects simultaneously a very broad class of events.

We now discuss briefly a number of possible phenomena, keeping in mind that just like in a bubble chamber, all types of **unexpected phenomena** will be observable as well.

2.1.-Proton Decay. The advances that the proposed detector will bring in the search for proton decay are relevant. Due to the tracking capability and the high resolution of the drift chamber, proton decay events have an unambiguous signature and can be much more easily separated from the background of neutrino induced reactions. The limitations of the present generation of large proton decay experiments, namely the limited vertex, energy, tracking and particle identifications in the presence of much larger neutrino backgrounds can be very easily overcome.

The detector, if filled with pure Argon, will have an active mass in the vicinity of 6500 tons corresponding to **3.8×10^{33} nucleons.** In absence of competing

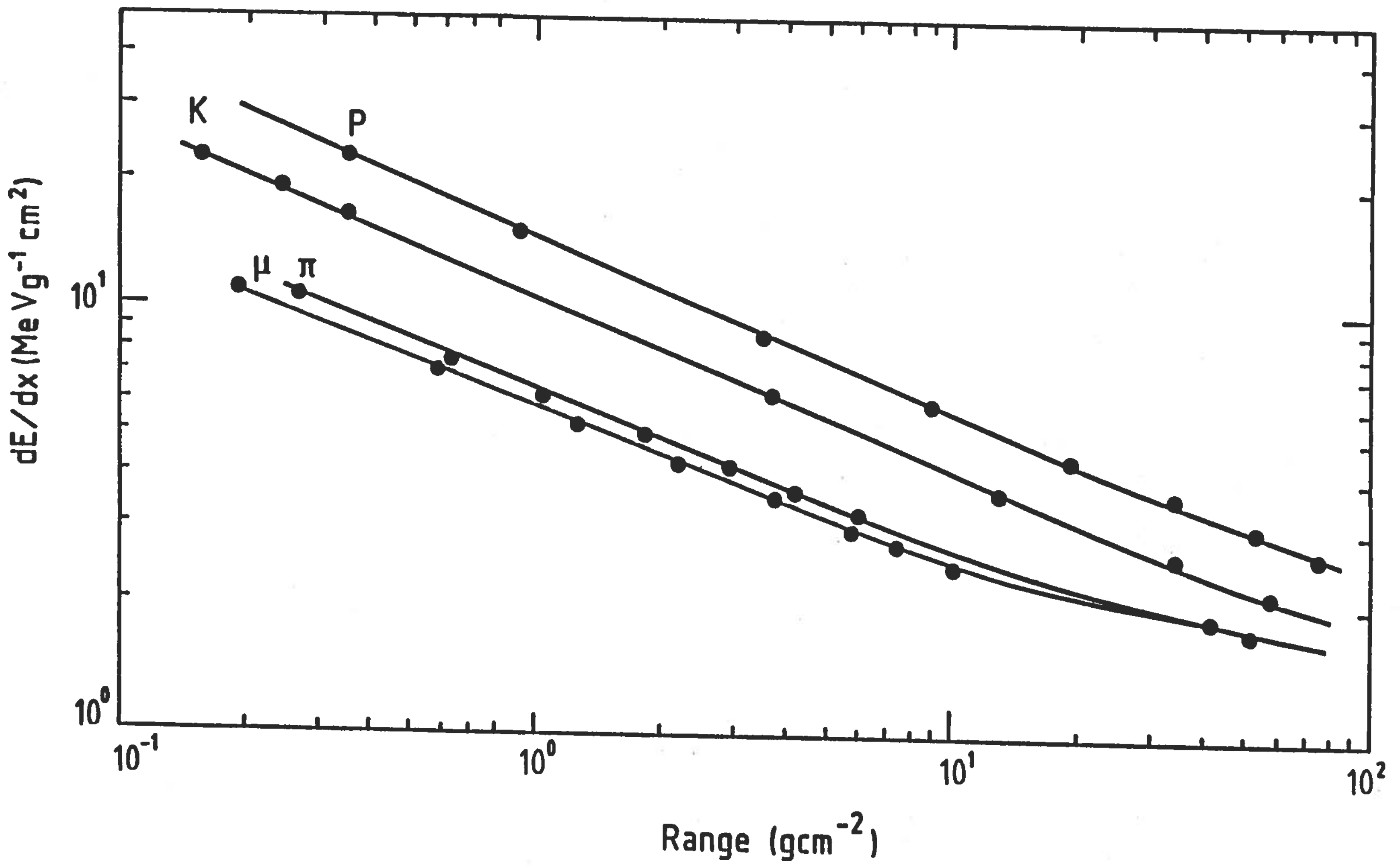

Figure 11. Energy loss vs. range in Argon for different particles. One can see that particle identification can be easily carried out between protons, kaons and (pions & muons).

backgrounds, in slightly more than one year of live time it should be possible to set limits on τ/B of the order of $2x10^{33}$ years at 90% c.l.. These limits are typically **two orders of magnitude longer** than present results. If Argon is replaced with pure Methane, the lower target mass of 1930 tons is more than compensated by the advantages of the presence of pure Hydrogen, amounting to 490 tons or $\mathbf{3.0x10^{32}}$ **free protons.**

The number of interactions due to cosmic neutrinos is well known from experiment and it amounts to about 160 events / kiloton / year, namely about 1040 events /year for Argon filling. The main advantage of the present proposal over the several already existing detectors is therefore that it provides a much more powerful rejection of these events, thus permitting the full utilization of the active mass and a high detection efficiency for proton decay processes. We believe that the kinematics of the neutrino induced interactions are sufficiently different from that of proton decays in order to identify them unambiguously. An elaborate Montecarlo is in progress to clarify this point.

2.2-Direct Observation of Solar Neutrinos from the ^{8}B Cycle. Solar neutrinos represent one of the most interesting areas of neutrino astronomy. In spite of the fact that the potential feasibility of obtaining information concerning the sun by means of neutrino astronomy became evident a long time ago 8), there exists so far only the Davis experiment 9) capable of detecting solar neutrinos. This radio-chemical experiment has an energy threshold of 0.814 MeV and is mainly sensitive to the Be - ^{8}B neutrinos from the reaction $^{37}Cl(\nu_e, e^-)^{37}Ar$.

The current observed flux from the sun is 2.2 ± .4 SNU, in sharp contradiction with the prediction of about 7 SNU from the standard solar model10). One SNU is equivalent to 10^{-36} captures per target atom per second. This "solar neutrino problem" has prompted a variety of solutions ranging from neutrino oscillations 11), neutrino decay 12), to a very large variety of non-standard solar models 13).

To solve this fundamental problem radio-chemical and geo-chemical experiments need to be complemented by direct counting experiments. With sensitivity to direction and energy an electronic detector can demonstrate unambiguously that solar neutrinos from a particular reaction have been detected.

The high density and the excellent spatial and energy resolutions of the proposed Liquid Argon image chamber make this novel type of detector especially suited for the first direct observation of **solar neutrinos** from the ^{8}B decay with the help of ν_e**- e scattering.** This is the dominant process occurring in Argon

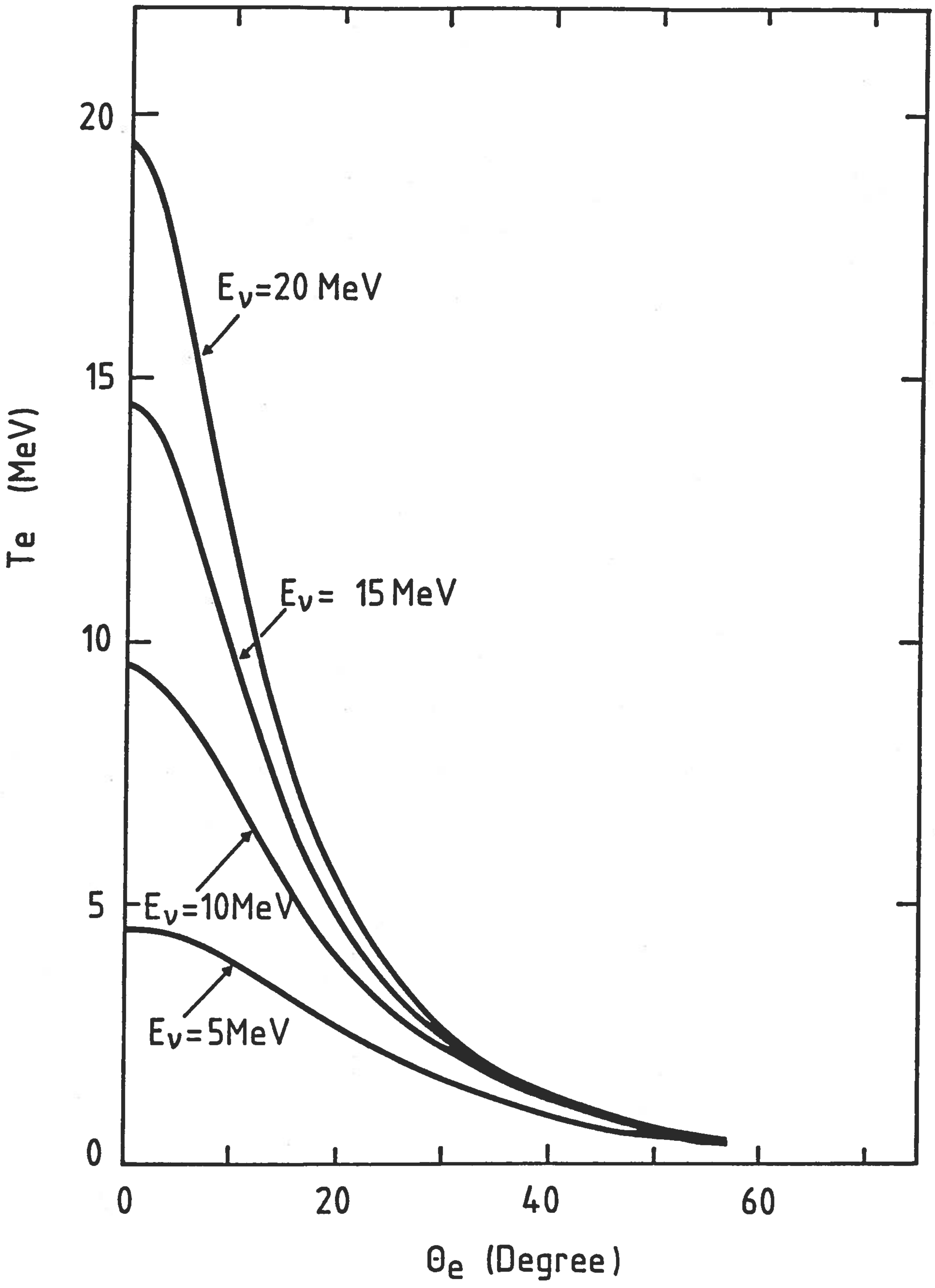

Figure 12. Kinematics for elastic neutrino-proton scattering

since binding energies supress the corresponding process on neutrons. Kinematics favours very small scattering angles and the process is highly directional (Fig. 12). This permits the correlation of the effect with the position of the sun and it insures a convincing subtraction of other backgrounds. The end-point of the electron spectrum is related to the end-point of the neutrino spectrum (Fig. 13). Therefore one can test also the ^8B origin of the effect.

The shape of the ^8B neutrino spectrum is proportional to $E_\nu{}^2(E_{max}-E_\nu)^2$ with an end-point E_{max} = 14 MeV. The number of events can be directly calculated taking a total flux of $2x10^6$ $cm^{-2}sec^{-1}$, which is obtained from the experimental value of the observations of Davis et al. The expected rates for 4500 m^3 of Liquid Argon **($1.7x10^{33}$ target electrons)** are listed in Table 1. The event rate depends sensitively on the threshold energy for electron detection.

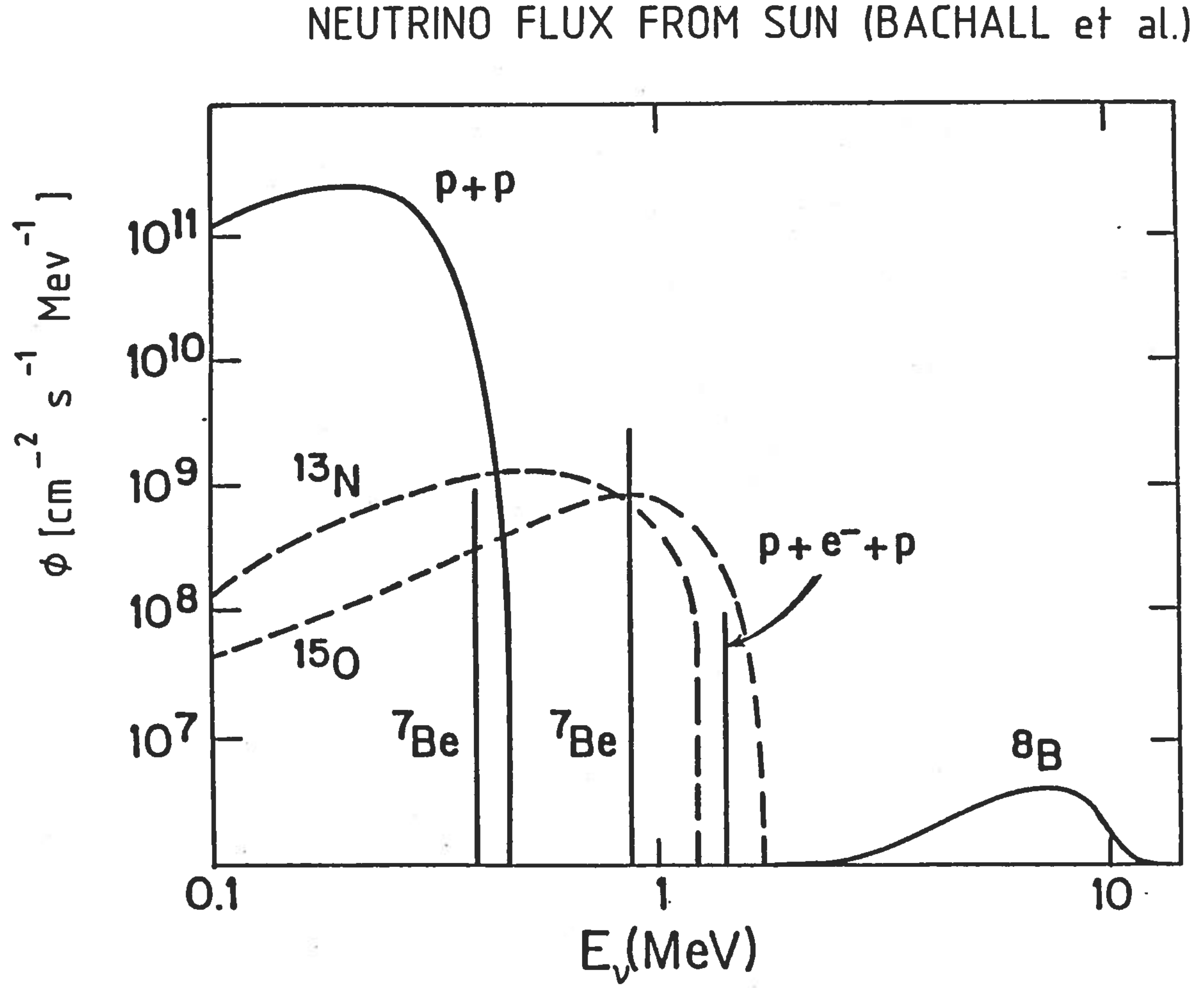

Figure 13. Solar neutrino fluxes according to theoretical calculations[10)].

Table 1-Event Rates for ^{8}B Neutrino Detection

Detection Threshold E_{thr}	Number of Events per day
0 MeV	20
4 MeV	9.3
7 MeV	3.0

The number of events is obviously proportional to the number of electrons of the detector, i.e. for a pure Methane filling the event rates are reduced by a factor 2.36.

The position of the Sun is known at all times and the angle and energy of the recoil electron can be connected to the kinematics of the process. The accuracy with which the angle of the electron can be measured is determined by the multiple scattering in the liquid. In these experiments the magnetic field must be kept off, since otherwise the electron track will be hopelessly curled. Assuming that a least square fit to a straight line is performed on the initial part of length λ (cm) of the electron track , the accuracy in the projected angle determination is :

$$\psi = \frac{2.16}{E_e} \sqrt{\lambda} \qquad \text{for Argon}$$

or

$$\psi = \frac{0.94}{E_e} \sqrt{\lambda} \qquad \text{for pure Methane}$$

where E_e is the electron energy (in MeV). Assuming $\lambda = 1$ cm, and $E_e = 10$ MeV, we find $\psi = .216$ radians (12.3^0) for Argon and $\psi = 0.094$ radians (5.4^0) for pure Methane.The energy of the electron is determined from the total energy loss to about 5%. The determination of the angle ψ is not accurate enough in order to permit the reconstruction with a reasonable precision of the energy of the initial neutrino. It provides however a very powerful rejection criterion against background.

2.3.- Search for other sources of low energy neutrinos and antineutrinos. The Sun is very probably the strongest natural source of ν_e in the MeV range . The Davis experiment is isotropically sensitive to all sources of ν_e and sets an upper limit to other processes. The cross section of the Davis reaction is strongly energy dependent (i. e., $\sigma \sim E^{3.7}$) and relatively few neutrinos of higher energy could also account for the observed effect, further complicating the problem of the missing solar neutrinos. It is a fortunate circumstance that the background coming from cosmic rays is quite low at least up to 50 - 100 MeV. Therefore we have an interesting detection " window ", in which one can search for novel neutrino sources.

Our detector is sensitive to several neutrino-initiated processes, with cross sections determined by the choice of the filling. In the case of pure Argon, because of the nuclear binding energy threshold and the Pauli principle, the dominant effect of incident neutrinos is limited to the electrons of the target, namely:

$$\nu_x + e \longrightarrow \nu_x + e$$

where the symbol ν_x stands for any type of neutrino or antineutrino. Cross sections of reactions on electrons are quite small, as one can see in Table 2.

<u>Table 2.- Neutrino-electron cross sections in the MeV range</u>

Reaction	Cross section (units of 10^{-45}cm^2)
$\nu_e + e$	$8.91 * E_\nu$ (MeV)
$\bar{\nu}_e + e$	$3.73 * E_\nu$ (MeV)
$\nu_\mu + e$	$1.45 * E_\nu$ (MeV)
$\bar{\nu}_\mu + e$	$1.24 * E_\nu$ (MeV)

However, just like in the case of the solar neutrinos, this is more than compensated by the directionality of the kinematics, which permits to dispose of a sort of rudimentary neutrino telescope with an angular resolution of approximately 10°. In order to preserve directionality, to reduce the background due to radioactivity and to insure detectability, we must set an energy threshold of at least 4 MeV for the recoil electron. The recoil electron spectrum is significantly different for the four possible kinds of neutrinos, as a consequence of the parity violation and helicity effects in the neutral and charged current channels (Fig. 14).

The main background process are of course due to natural radioactivity. Presence of impurities inside the liquid may of course give rise to electrons . There are relatively few nuclei which can give rise to electrons of several MeV and the ultra high purity of the Argon in our detector is of course the necessary pre-requisite.

In addition to these effects, which can be settled only experimentally, there are photons from radioactivity of the walls, electrodes, etc. which are strongly attenuated in the Argon and therefore are to be kept under control with geometrical cuts. The fact that the drift-path is as long as 2.15 m insures ample leverage for subtraction of these backgrounds. Finally, the possibility exists to produce short lived nuclei due to cosmic ray induced interactions (muons, neutrons, etc.), which then decay with relativly high energy electrons. This is probably the main background in the energy region around 10 - 15 MeV. The most effective way of removing such backgrounds is the one of keeping an accurate record of all previous ionizing events which have occurred in the region immediately neighboring the recoil electron. This is relativly easy in our case, since the detector is continuously and totally sensitive. The flux of cosmic rays deep underground in the Gran Sasso Laboratory is sufficiently low to demand the absence of nuclear reactions in the region of the event up to several hours before the occurrence of the recoil electron with no appreciable loss of sensitive time.

Additional processes can be used to evidence the presence of a significant neutrino flux in the Gran Sasso laboratory. A pure Methane filling will add a large number of free protons. They provide a significant cross section for **anti-neutrinos,** according to the process:

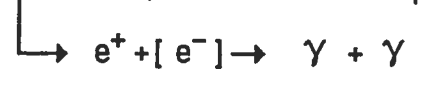
$$\bar{\nu}_e + p \longrightarrow e^+ + n$$
$$n \longrightarrow \text{slow down +capture}$$
$$e^+ + [\,e^-\,] \longrightarrow \gamma + \gamma$$

which has a threshold of 1.80 MeV. The cross section is easily calculated according to standard V-A interaction. Since the neutron recoil energy is quite small the energy of the positron is quite close to the one of the incident neutrino.

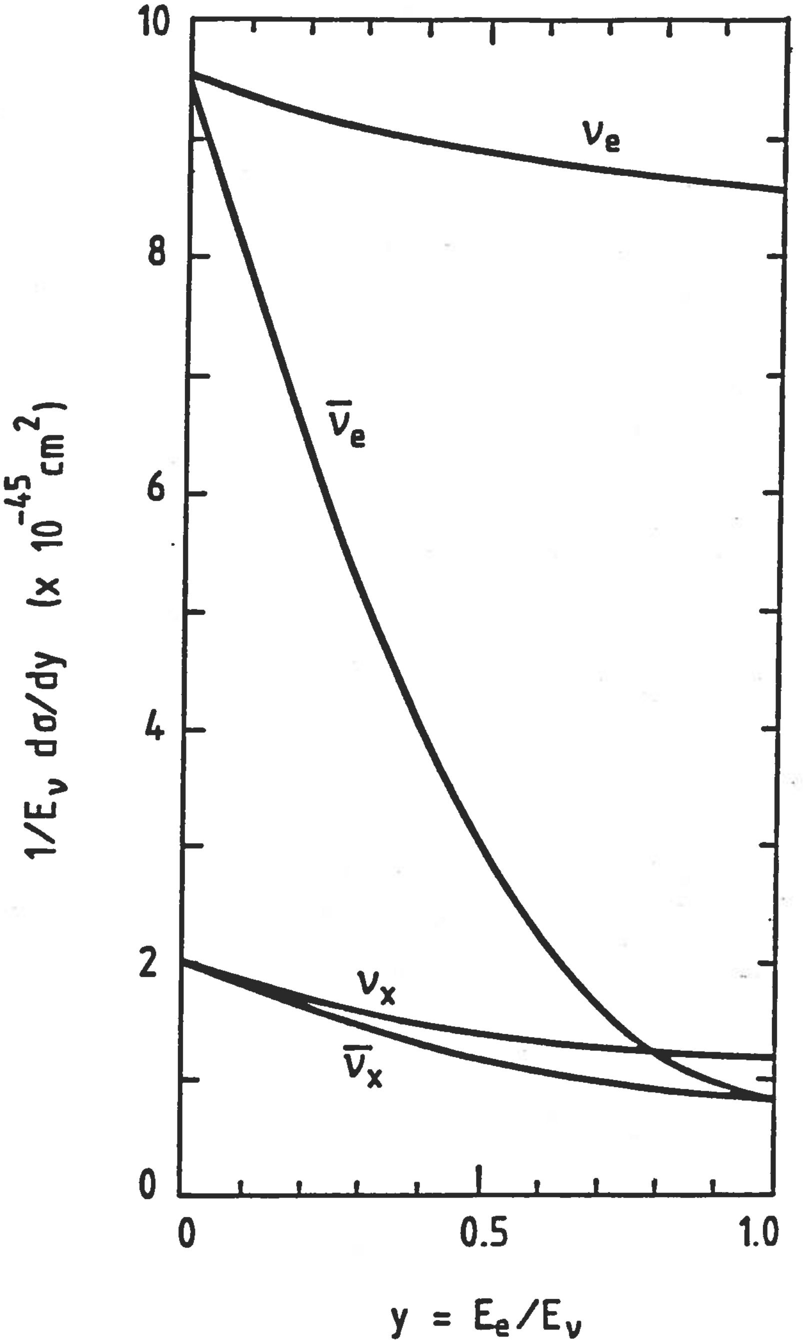

Figure 14. Electron energy spectrum for different types of neutrino-electron scattering. In the formulae the approximation $E_\nu >> m_e$ has been applied.

Finally, by adding deuterated Methane one can detect **neutrino** through the reaction

$$\nu_e + (n) \longrightarrow p + e^-$$

which has the threshold at 1.44 MeV. Because of the Fermi motion the electron spectrum is somewhat widened (Fig. 15). The cross section is given in

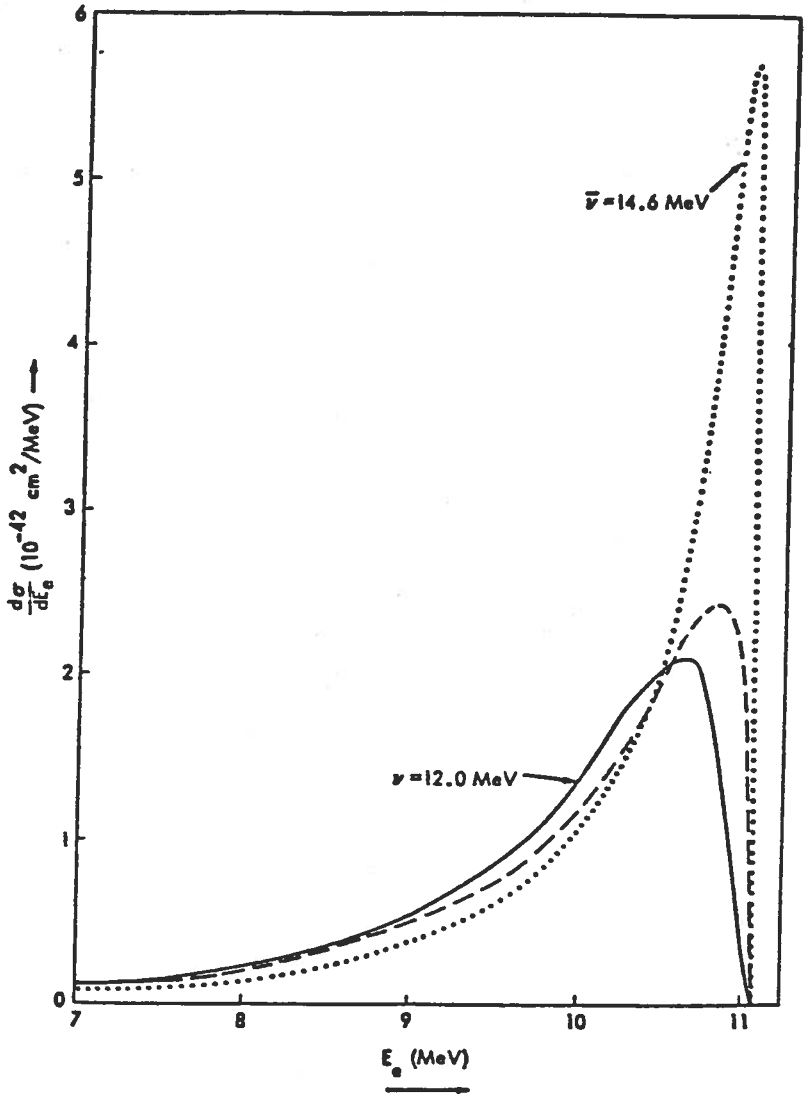

Figure 15. Electron spectrum from Deuterium disintegration by neutrinos (Ref.14). The electron spectrum is shown by the continuous line; the broken line is the corresponding distribution in the case of the "uncharged" proton.

Fig. 16. The experimental signature for such a process is some what weaker, since one records simply an electron without sharp angular constraints. Note that there is also the equivalent process on the proton of the Deuterium which is initiated by anti-neutrinos and has an energy threshold of 4.04 MeV (Fig. 16) .

Which sources of (anti-)neutrinos are observable at the Gran Sasso? The search for anti-neutrinos from the **gravitational collapse of a star in our galaxy** is one of the most fundamental processes in astrophysics. During the collapse of a star three stages of neutrino emission can be identified (see Fig. 17):

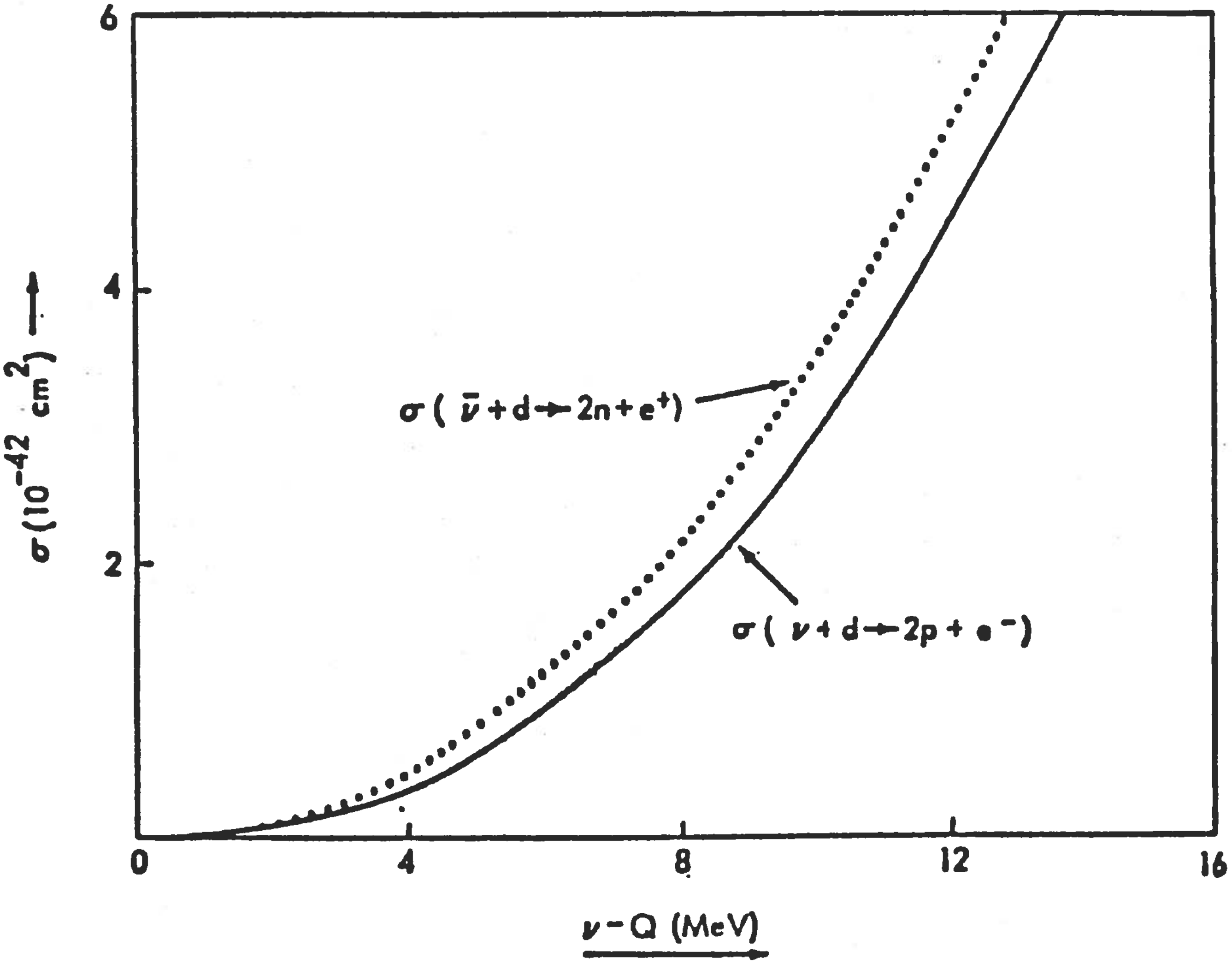

Figure 16. Cross sections for neutrino and anti-neutrino initiated processes in Deuterium. The cross sections are plotted vs. (E_ν-1.44) MeV for the reaction on neutrons (solid line) and vs. (E_ν-4.04) MeV for the corresponding anti-neutrino reaction on protons (Ref. 14).

i) Neutronization : only ν_e are emitted with a peak luminosity of 10^{59} ν_e /sec in a short burst of a few milliseconds.

ii) Deleptonization: before full trapping and formation of the neutrino sphere; neutrino and anti-neutrino emission continues for about 1 sec.

iii) Cooling : the neutrino emission continues from the neutrino sphere during the Kelvin cooling of the newborn neutron star for several seconds.

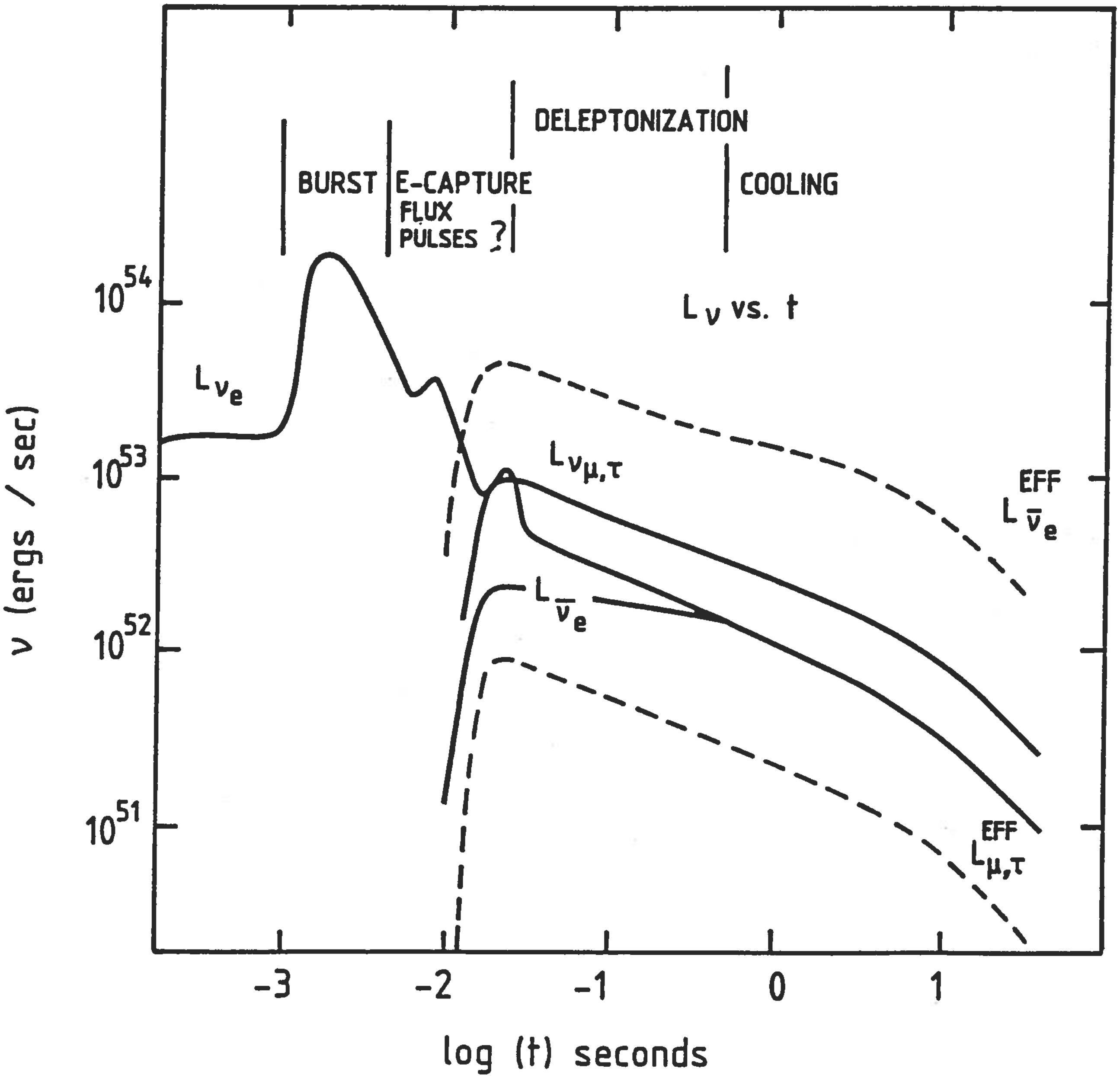

Figure 17. Time dependance of the neutrino emission after Supernova collapse.

The energy of the neutrinos and anti-neutrinos is of the order of 10 MeV. The expected rate for supernovæ explosions in our Galaxy is only **one every 10 - 30 years,** making individual detection very problematic. A much greater rate of supernova explosions is expected in the whole Universe. An alternative detection method could be to see the **cumulative effect** of all these explosions. Presumably supernova explosions have been occurring at a constant rate for most of the history of the Universe and as a consequence a **diffuse background of neutrinos and anti-neutrinos** must exist. The flux of neutrinos and antineutrinos at the earth's surface has been calculated by Krauss et al.15), taking into account the effect of expansion. If the Universe had a constant supernova frequency the net effect of the expansion is to reduce the neutrino energy by a factor 3/5 compared to what could be expected otherwise. The mean energy of about 10 MeV at time of emission becomes therefore red-shifted to about 6 MeV. Assuming 10^{53} erg emitted per supernova explosion and 1/20 years average occurrence in a volume of 1 Mpsec^3, Krauss et al.15) find :

$$N(\nu,\bar{\nu}) = 4.7 * 10^3 \ \mathrm{cm}^{-2} \mathrm{sec}^{-1}$$

made roughly of half neutrinos and half anti-neutrinos peaked at 6 MeV. Let us now compare with the help of Fig. 18 the anti-neutrino flux from supernova explosions to that from other sources of neutrinos and anti-neutrinos in the same energy domain :

i)-**Solar neutrinos** are much more abundant. For instance the ^8B contribution alone is about $2x10^6 \ \mathrm{cm}^{-2}\mathrm{sec}^{-1}$, even after scaling down the flux according to the Davis' result. Therefore the solar neutrino flux will mask all other possible extraterrestial sources in the 0.1-15 MeV range, including relic supernovae. However anti-neutrinos are conspicuously absent from all major solar reactions. Therefore the detection of **extragalactic sources** must be limited to **anti-neutrino** events.

ii)- A large flux of anti-neutrinos is expected from **natural radioactivity.** The contribution with the highest anti-neutrino energy comes from the ^{238}U decay chain. The total flux from all decays is of the order of $10^7 \ \mathrm{cm}^{-2}\mathrm{sec}^{-1}$ with an end point of 3.3 MeV. Clearly a very good resolution is required to separate a supernova signal above this energy.

iii)- **Nuclear reactors** and thermonuclear explosions are powerful man made sources of anti-neutrinos with an energy up to 8.5 MeV due to the the decay of fission isotopes. A power station emits anti-neutrinos with an average energy of about 4.0 MeV. In the immediate vicinity of the Gran Sasso Laboratory there are at present at least three nuclear power stations of significant intensity, listed in Table3. However, very important contributions are expected from very distant power stations, scattered all over Europe (Fig. 19) . It is interesting to note that the contribution of the power stations in the United States amounts to about 6% of the observed signal. A fair estimate [16)] of the total flux gives approximately 3.0 x10^5 $cm^{-2}sec^{-1}$. Over the next several years, in view of the power stations under construction, it may exceed 10^6 $cm^{-2}sec^{-1}$.

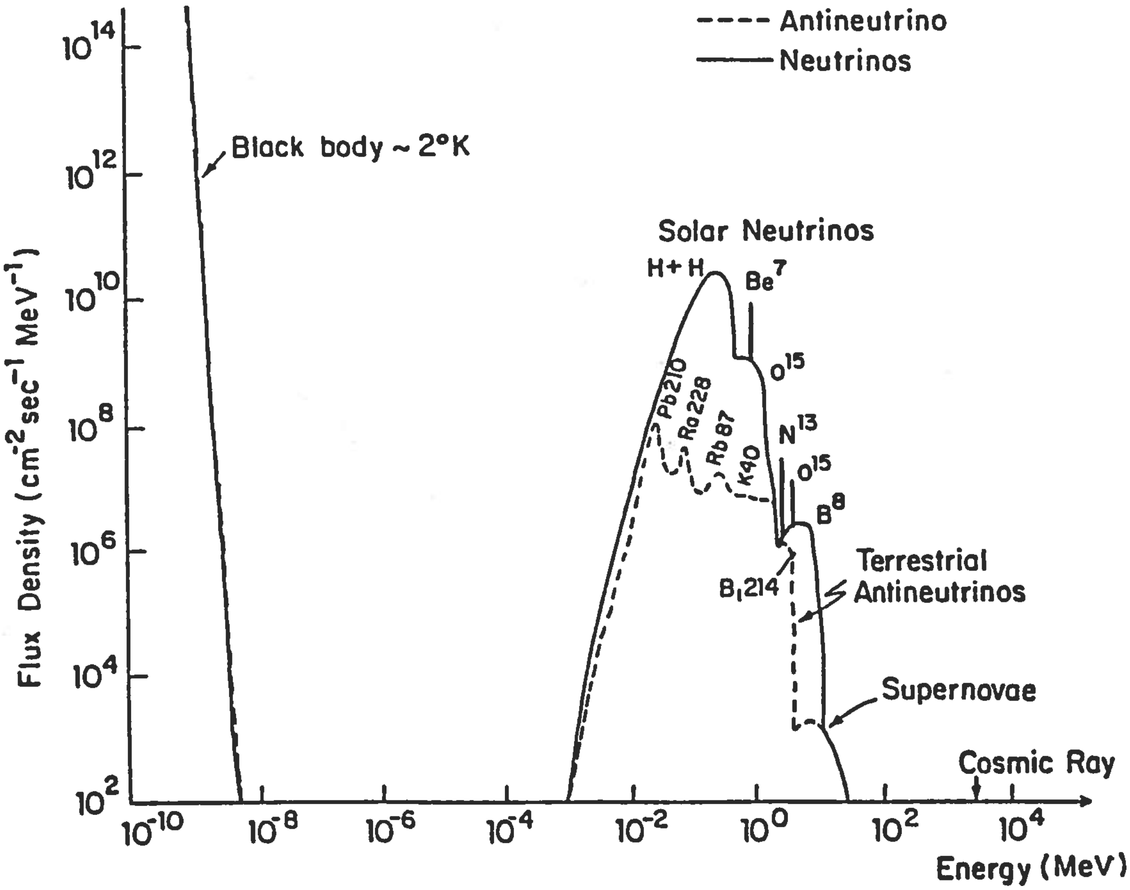

Figure 18. Neutrino and anti-neutrino fluxes on earth, according to Krauss et al. (Ref. 15). Note that the cosmic ray flux is neglegibly small at low energies.

Cross sections for all these processes, integrated over the spectrum and for the requirement that the recoil energy of the electron (or the positron) exceeds 4 MeV are given in Table 4. The event rates can be estimated for three typical detector conditions, namely:

i) pure Argon, corresponding to 1.7 10^{33} electrons

ii) pure Methane, corresponding to 3.0 10^{32} free protons and finally

iii) a 10% mixture of deuterated Methane, namely 100 tons of Deuterium or 3.0 x10^{31} neutrons.

The pure Argon detector is mainly sensitive to the signal coming from electrons of the target, which is significant for its directionality. Pure Methane enhances the anti-neutrino signal, with the powerful signature of the positron annihilation and the neutron capture. Rates are summarized in Table 5.

Table 5.- Rates of low energy neutrino events .

PROCESS	FLUX cm^{-2} s^{-1}	ARGON	METHANE	10% CD_4
Sun ^8B	2.0 10^6	8. ev/day **directional**	3.2 ev/day **directional**	5.58 ev/day **wide angle**
Far away Reactors	3.0 10^5	0.03 ev/day **directional**	7.5 ev/day **annihilation &capture**	<0.3 ev/day
Relic Supernovæ	5.0 10^3	0.02 ev/day	0.50 ev/day **181 ev/year** **annihilation &capture**	0.050 ev/d **18/year**

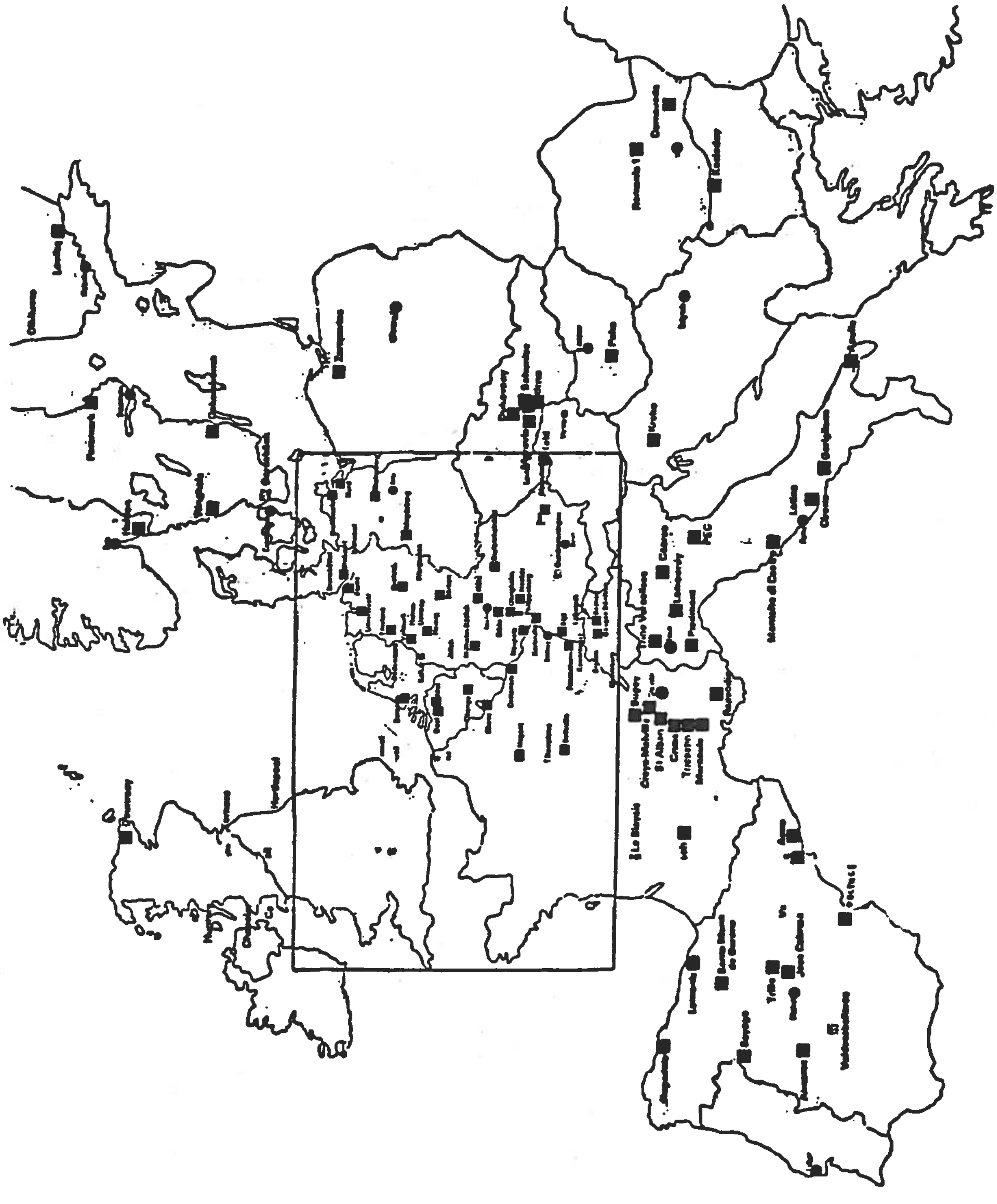

Figure 19. Map of Europe with distribution of power reactors.

Table 3.- Contribution of Far away Nuclear Power Stations.

Country	Total power M WATT	Flux contribution KW/KM^2
1. Italy		
Latina	(150.)	(23.8)
Trino Verc.	(260.)	(1.7)
Caorso (Piac)	(375.)	(9.2)
Total	1,285	34.7
2.France		
Total	27,668	51.5
3.West Germany		
Total	12,243	21.5
4.Switzerland		
Total	4,004	12.5
5.Spain		
Total	3,667	3.3
6.East Germany		
Total	1,830	2.1
7.Czechoslovakia		
Total	1,320	3.1
8.Hungary		
Total	880	3.0
9.Austria		
Total	692	2.5
10. Yugoslavia		
Total	615	5.7
TOTAL EUROPE	41,673	138.8

Table 4 .- Spectrum averaged cross sections.

PROCESS	SPECTRUM $\langle E \rangle$ MeV	PARTICLE TYPE	$\langle \sigma \rangle * 10^{45}$ cm^2 $E_e > 4$ MeV		
			$\nu - e$	$\nu - p$	$\nu - n$
Supernova Collapse	10 MeV	ν_e (50%)	64.10	----	2603.
		$\bar{\nu}_e$ (50%)	15.90	10300.	----
Relic Supernovae	6.6 MeV	ν_e (50%)	31.60	----	1277.
		$\bar{\nu}_e$ (50%)	6.12	4074.	----
Far away Reactors	4.1 MeV	$\bar{\nu}_e$	0.786	979	----
Sun ^{8}B	7.0 MeV	ν_e	27.39	----	1077.

In view of the tremendous importance of detecting the diffuse neutrino radiation from supernovæ collapses, we must consider backgrounds with more detail. An energy cut at about 10 MeV must be applied to the data in order to remove the background coming from nuclear power stations (Fig. 20) This reduces the event rate by about a factor two, which is acceptable. The angular distribution of the positron is peaked in the direction opposite to that of the neutrinos :

$$d\sigma/d\Omega = (1 - \cos \Theta_{\nu e})^2$$

This property can be used to verify the isotropic nature of the signal, since most of the power stations are located north of the Laboratory. The energy cut should also reduce to a neglegible level the background coming from radioactivity.

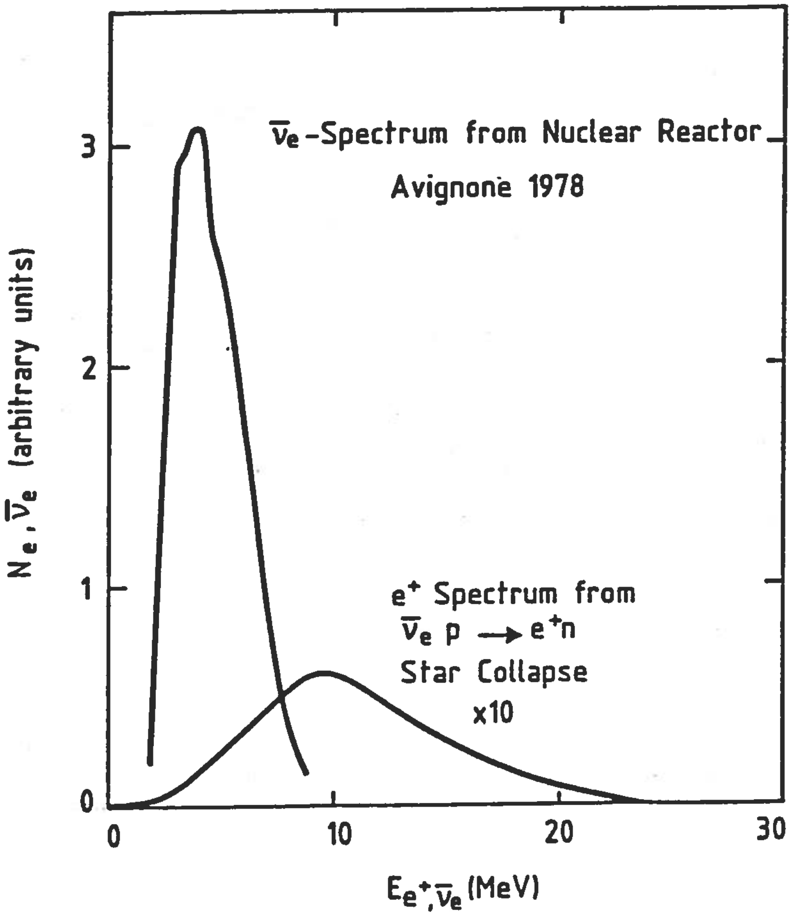

Figure 20. Comparison between the expected neutrino spectrum from far away nuclear reactors and the expectations of relic neutrino signal according to Krauss et al. (Ref. 15). Spectra have been normalized to the expected fluxes.

Finally the cosmic ray background is very low, as shown in Fig. 21. Even taking into account the **large uncertainties in the predictions of the neutrino flux,** a search for diffuse background from supernovæ collapses remains an exciting part of our program.

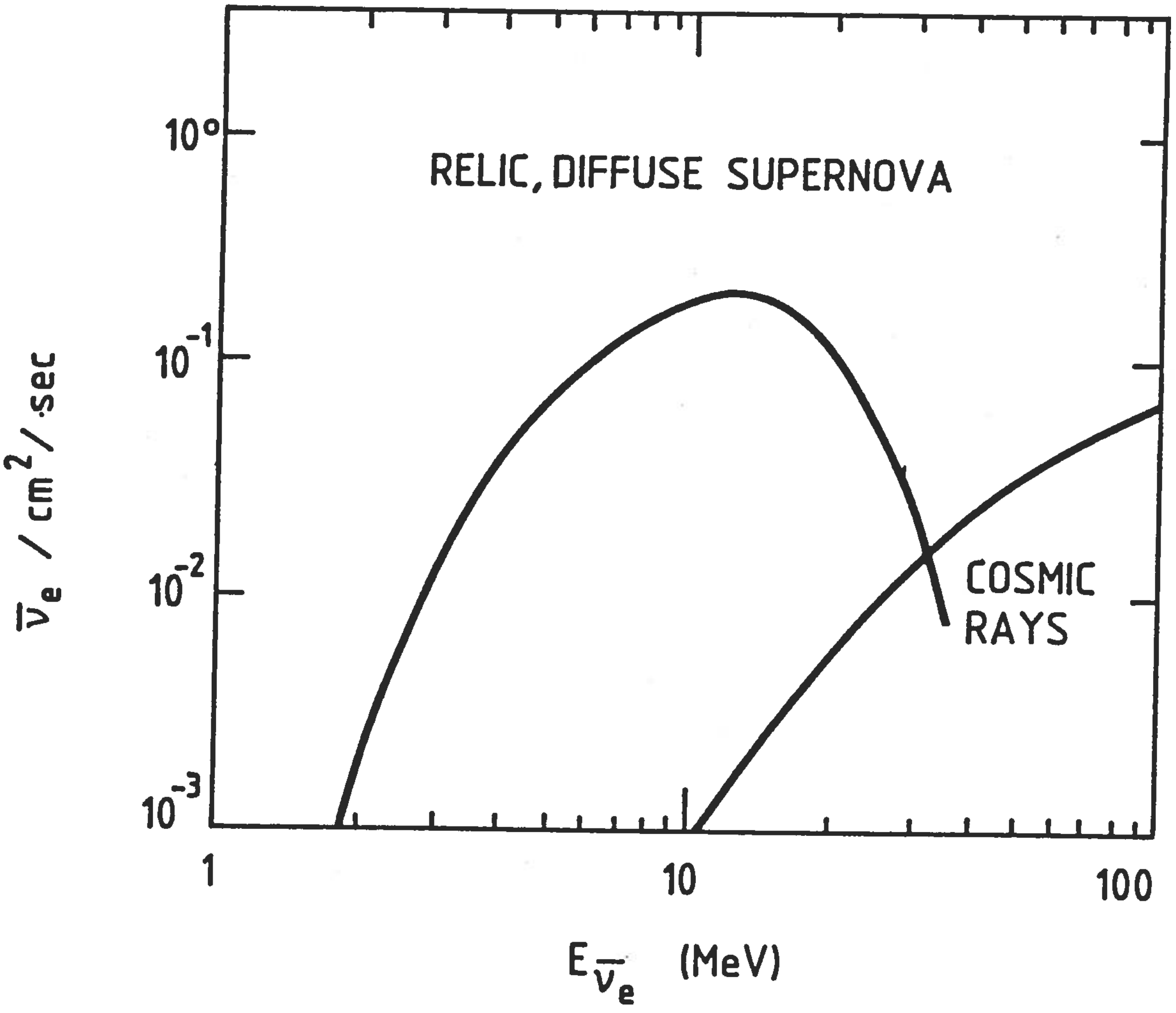

Figure 21. Comparison between the expectation for the relic neutrino background and the cosmic ray background. One can see that below 30 MeV, the cosmic ray background is small.

Table 6. Parameters of a typical Supernova collapse [17]

Quantity	ν_e	$\bar{\nu}_e$	ν_μ , ν_τ etc.	
Total number	2.7	2.0	8.0	(x 10^{57})
Total energy,erg	4.5	3.3	13.3	(x 10^{52})
#/cm^2 @ 1 kparsec	2.4	1.8	7.2	(x 10^{13})

A sudden supernova collapse will induce in our detector a burst of events, lasting several seconds [17]. In the case of the Argon filling, the main detection channel is the ν-e scattering, which has the interesting property of being highly directional. In a simple model [17], the properties of the neutrino emission are given in Table 6. Using these numbers and the cross sections of Table 4, we find at 1 kpc 3,600 events on electrons in the case of Argon filling and 74,000 events for pure Methane. Assuming a range of 13 kpc, corresponding to 75% of our Galaxy, we find 21 highly directional e-ν scattering events for Argon and 440 antineutrino proton scattering events for Methane filling. Clearly, in both cases a **collapse cannot be missed over most of the Galaxy.** Of course such events may never occur during the period of the experiment, since it is expected to take place only a few times every century. Special provisions have to be made on the read-out, in order to insure that such a large instantaneous event rate does not run into dead time problems.

2.4. Neutrino Oscillations. The detection of neutrino events coming from far away can provide informations on the existence of neutrino oscillations. The flux from reactors is in principle calculable, provided an accurate record is kept of their mode of operation. The spectrum shape can in principle be determined from an experiment performed close to the reactor, of which there are at present several in progress. Eventually a small scale Liquid Methane device could be operated in the immediate vicinity of one of the high power reactor in order to determine accurately the absolute flux and the spectrum of the recoil positrons. The positron spectrum is then compared with the one recorded at the Gran Sasso Laboratory. Our experiment provides an average baseline of about 550 km to neutrinos from the power reactors of Table 3, to be compared to the typical flight path of about 50 m of the experiment in progress today. Even more powerful could be the study of the solar neutrinos. The flight-path is then 100 Million km, corresponding to a sensitivity in the mass difference δm^2 of about 10^{-12} eV^2. In principle the ν-e scattering is sensitive to all forms of neutrinos, while the Davis experiment and the Deuterium fillings measure only the neutrino-electron component. However the cross section for ν_τ and ν_μ is about 15% of the one for ν_e, due to the differences in the couplings and of the y-distributions. In the case of a complete neutrino oscillation mixing, the Argon experiment would then record a neutrino flux only about 30% higher than the Davis experiment, which is very marginal. Unfortunately the energy distributions of the recoil electrons for neutrinos of different types are quite similar (Fig. 14) and a separation based on the spectral shape is very difficult. The only way of detecting the presence of an appreciable transition probability between the different neutrinos is a **precision experiment** in which one compares at the few percent level the rate observed from electron scattering and the one coming from Deuterium filling, where the reaction

$$\nu_e + (n) \longrightarrow p + e^-$$

is compared with:

$$\nu_x + e \longrightarrow \nu_x + e$$

where the symbol ν_x stands for any type of neutrino or antineutrino. The values of both cross sections are almost perfectly known and the rate of events is in principle adequate for a few percent determination of the ratio of the cross sections. Incidentally, there is a 6% rate change over the yearly cycle due to the elliptic orbit of the Earth around the Sun.

Additional informations on neutrino oscillations may becollected indirectly, provided the presence of the relic supernovæ neutrino background is detected.

2.5-Atmospheric Neutrinos. Atmospheric neutrino events are not simply background to the search for nucleon decay. They are per se a very interesting signal, which relates for instance to the study of neutrino oscillation over a baseline of the order of the earth diameter. The proposed detector can nicely recognize different types of neutrino interactions, namely ν_μ, ν_τ and ν_e, as well as measuring accurately kinematics. Neutrino oscillations can be detected using atmospheric neutrinos that have traversed the earth :

$$\nu_\mu \rightsquigarrow \nu_e + N \longrightarrow e + X$$

$$\nu_\mu \rightsquigarrow \nu_\tau + N \longrightarrow \tau + X$$

In the case of $\nu_\mu - \nu_\tau$ oscillations the use of atmospheric neutrinos is the only technique to improve the present limits on this oscillation. This is because of the need to observe ν_τ interactions with energy above τ threshold, i.e. $E_\nu > 5$ GeV. Thus L / E_n, where L is the flight path and E_ν is the neutrino energy, is always much less than 1 m / MeV for terrestrial experiments but can be of order 10000 km / 5 GeV = 2000 m / MeV for atmospheric neutrinos. The process

$$\begin{array}{l} \nu_\tau + N \longrightarrow \tau + X \\ \qquad\qquad\quad \hookrightarrow n(\pi) + \nu_\tau \end{array}$$

can be detected through the reconstruction of the invariant mass of the multi pions from the τ decay and is another example of the need for a high resolution magnetic spectrometer. The signature for τ production is shown in Fig. 22. The rate of ν_μ and ν_τ events with $E_\nu > 5$ GeV is approximately 100/year in 5000 tons.The signature for τ production is shown in Fig. 23. The expected production cross section is given in Fig. 24 indicating the necessity of using high energy neutrinos to produce τ's efficiently.

2.6.-Search for very high energy point-like neutrino sources. High energy neutrino astronomy is another interesting new development made possible by the present detector, because of its large area coupled to magnetic analysis of traversing muons. Very high energy neutrino ν_μ's interact in the rock surrounding

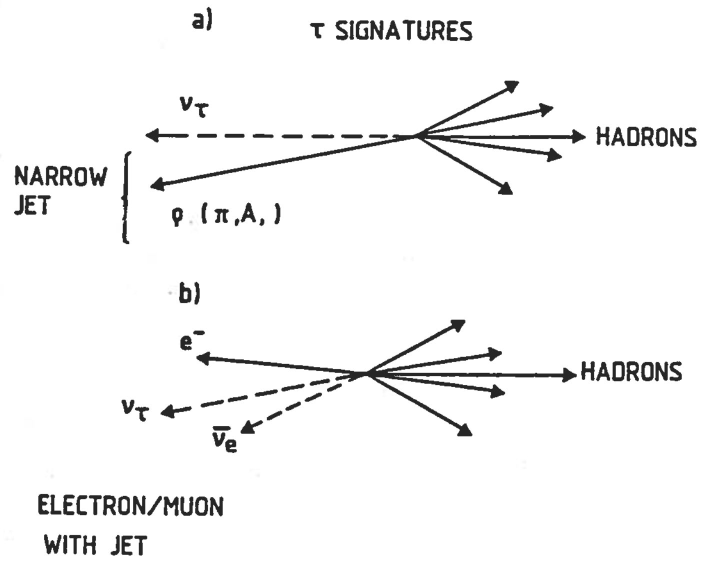

Figure 22. Topological signatures for τ neutrino events

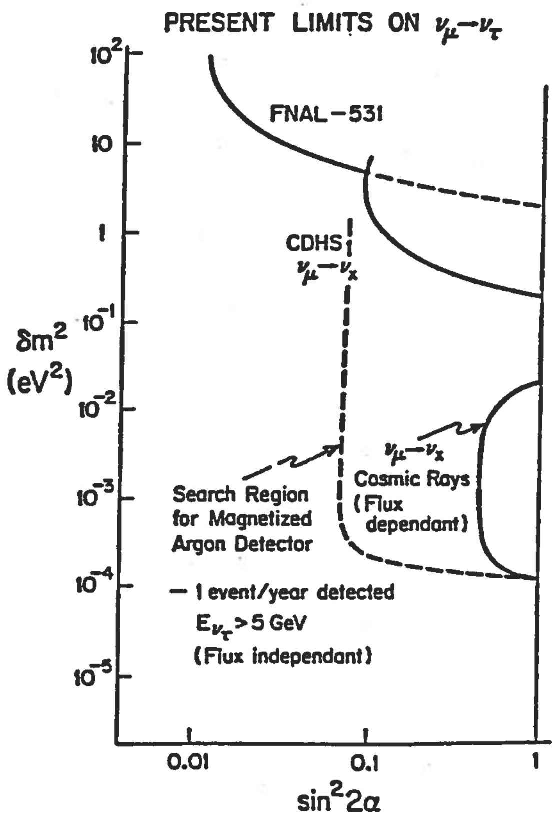

Figure 23. Limits on ν_T mass oscillations which can be set with atmospheric neutrinos and one year of data taking. Accelerator experiments are also shown for comparison.

the detector. Secondary penetrating muons traverse a large amount of material before reaching the detector resulting in a very high effective target mass. Recently, very intense sources of gamma rays in the range 1-10^4 TeV have been observed with a spectral power law of the type E^{-2}. These ultra high energy gamma rays are observed only during two very short intervals, in contrast with softer X-rays which are modulated more or less following a sinusoidal cycle. The *Cyg* -X3 and the *Vela*- X1 are examples of such pulsars made presumably of closely interacting binary systems. It is very likely that the emission of of the gamma rays is due to π^0 - decays. A corresponding process leading to ν_μ emission is then naturally associated with $\pi^\pm$ production and decay. Because ν_μ emitted are not affected by the shielding of the companion stars, they should be present during the whole eclipse time and the intensity will be correspondingly larger (about a factor 10). A neutrino flux with spectrum law of the type E_ν^{-2} is detected very efficiently, since both the neutrino cross section and the average muon momentum (and hence the effective "target" length) grow linearly with E_ν, thus cancelling the spectral index of -2. Therefore the differential spectrum of the "detected" neutrinos is essentially flat and the high energy portion of the neutrino spectrum gives the dominant contribution . Eventually the W-propagator, the interaction losses of the muons in the rock and possibly the end-point of the neutrino spectrum will cut off the spectrum of the muons traversing the apparatus .

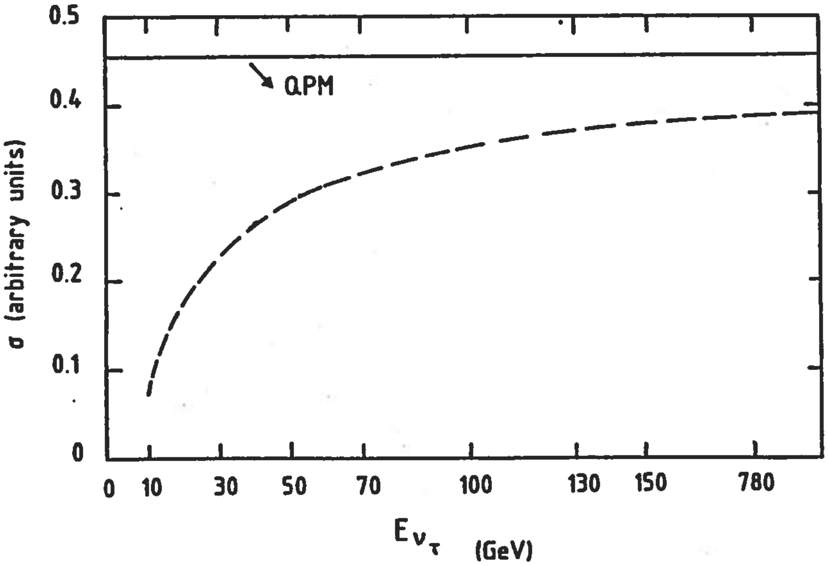

Figure 24. Cross section for detecting neutrino taus. The need for high energy events is apparent.

There are indications that in the center of our Galaxy there is a very compact and massive object. It is impossible to observe it optically because of the dense material surrounding it. Neutrinos instead propagate freely and therefore they could be detected, provided they are emitted in a sufficient number.

There are several active galaxies and very bright objects like the *3C 273* and the *Cen*-A which could be strong neutrino emitters, provided a mechanism for proton acceleration exists, similar to the one leading to the electron acceleration which is responsible for the electromagnetic syncrotron radiation (from radio to X-rays) which is currently observed.

Detection of such high energy neutrino sources is only possible provided the background due to atmospheric cosmic ray interactions is reduced. The very large flux of downward going muons limits observation to approximately one half of the sky, namely to the southern hemisphere. Even the sample of the up-going muons can be significantly contaminated by neutrinos produced by cosmic rays in the atmosphere. The rate of isolated upward muons from these neutrinos is about $2.0 \times 10^{-12} cm^{-2} s^{-1}$, namely, about 1 ev/day through the sensitive volume of our apparatus. This background can be effectivly reduced increasing the muon detection threshold. For $E_\mu > 100$ GeV, the muon flux is reduced to about 1/week; for $E_\mu > 1$ TeV we are at the level of 1/month.

Gaisser and Stanev [18)] have calculated the rate of upward muons induced by an arbitrary spectrum of neutrinos. The spectrum of muons at the detector is shown in Fig. 25. One can express the result as probability that a neutrino of energy E_ν directed toward the detector produces an upward detectable muon of energy above a threshold $E_\mu > 2$ GeV, 100 GeV and 100 TeV respectively. Thresholds have minimal effects on the detection efficiency of the higher energy muons from neutrinos coming from the *Cyg*-X3. Besides reducing the background due to atmospheric neutrinos, the energy threshold sharpens dramatically the angular resolution. With a threshold of $E_\mu > 100$ GeV the angular resolution becomes better than 1 degree r.m.s. For a given point source and a 90% geometrical acceptance cone we must accept muons pointing to the source within a solid angle of $\Omega/2\pi = 4.0 \times 10^{-4}$ reducing the cosmic ray accidental background to about 0.02 ev/year.

The detectability of a cosmic neutrino source in our detector depends on the spectral law index γ (defined by the shape of the neutrino spectrum $E_\nu^{-\gamma}$), on the distance and on the total radiated power. It is also necessary that the source is located in such a way as to give upward going muons in the detector. The time averaged exposed area of our detector in galactic coordinates is shown in Fig. 26. For instance, in the case of the *Cyg* -X3 the time averaged area is about 100 m^2. According to Gaisser and Stanev [18)] for $\gamma = 2.0$ and $E_\mu > 100$ GeV the rate of muons is 1.3×10^{-8} of the neutrino flux with $E_\nu > 2$ GeV. Therefore the flux needed to observe 5 ev/year is $1. \times 10^{-5}$ $\nu/cm^2/s$. At a distance of 10 kpc this corresponds to a neutrino luminosity of the order of $3 \times 10^{-41} \ln E_{max}$ Gev sec^{-1} or 5×10^{39} erg/sec. A recent estimate [19)] of the total cosmic ray output of *Cyg*-X3 is of ~ 10^{39} erg/sec. Unfortunately the X-ray luminosity is about two orders of magnitude less. Therefore the detection of the neutrino emission may be marginal, mainly because the position of the *Cyg*-X3 is at the edge of the detection window. A much better sensitivity is expected for the *Vela*-X1 and for active Galaxies like the *Cen*-A and the *3C 273*.

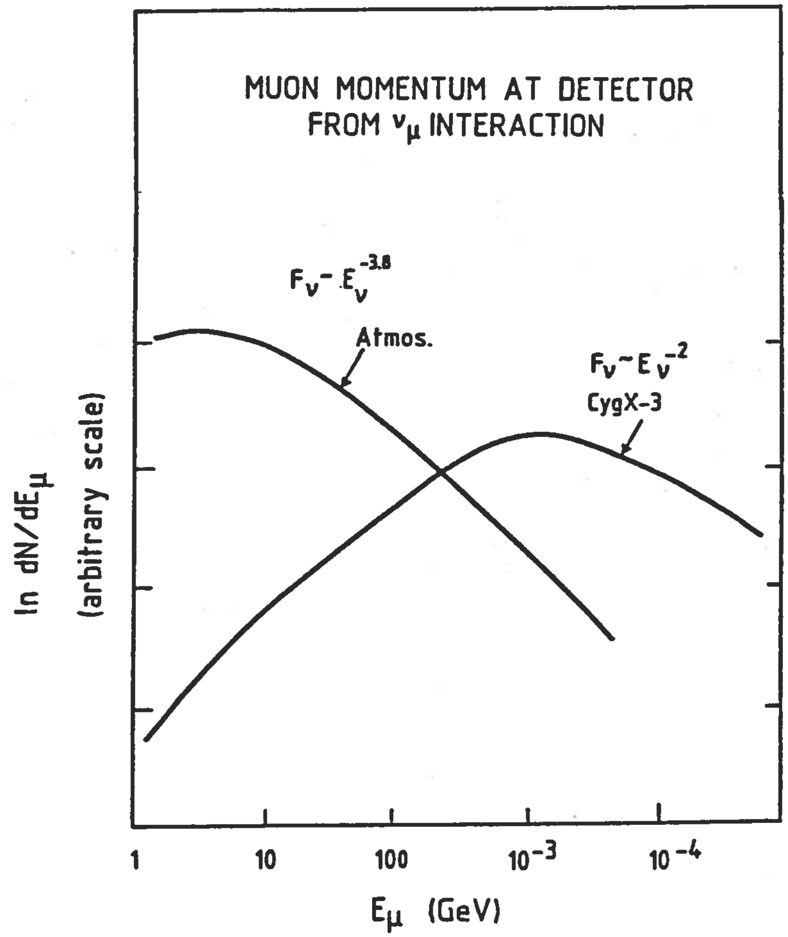

Figure 25. Muon momentum spectrum from cosmic ray neutrino events and expectations from neutrinos produced by the *Cyg*-X3 emission of neutrinos with spectrum similar to the one observed for γ's. From Gaisser and Stanev [18)].

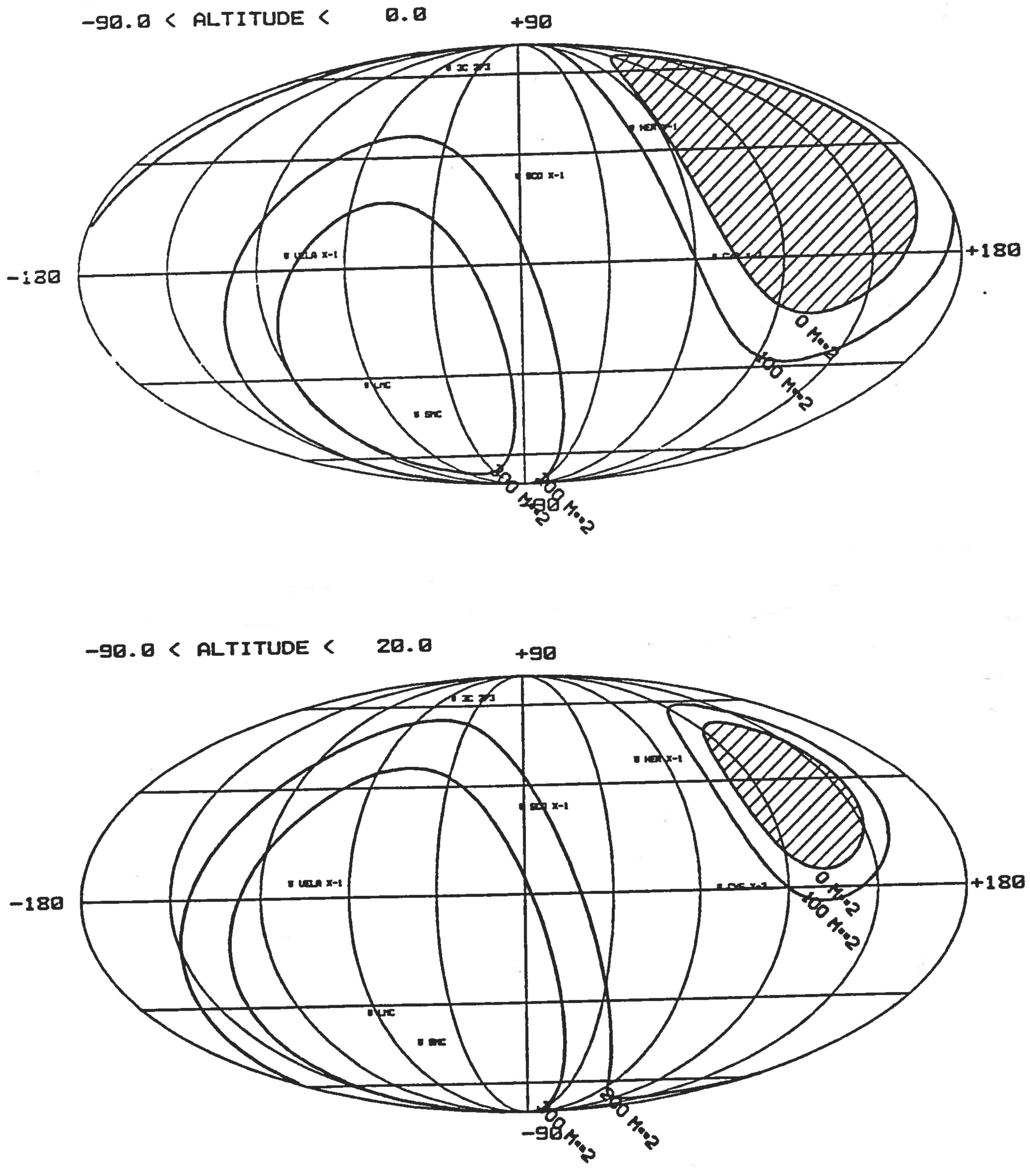

Figure 26. Time averaged exposure for the galactic coordinate plane. In the top graph only upward events are retained. In the lower picture the azimuthal angle has been relaxed to 20^{o} above the horizon.

2.7-What is happening on the Cygnus-X3 ? Recently several groups[20)-23)] have reported the observation of energetic atmospheric showers (10^{12} - 10^{15} eV) from X-ray binaries like *Cyg*-X3, *VELA*-X1 and *LMC*-X-Y. The nature of the incident particles is unknown, but their alignment with a point source at a distance larger than 10 kpsec, their energy and the existence of a galactic magnetic field, indicate that the primaries must be electrically neutral. For this reasons and because of the fact that *Cyg*-X3 is a known keV X-ray emitter, a photon interpretation has been assumed. A possible origin could be the production of very energetic protons (10^{17} eV) in the binary star producing neutral and charged pions in the collision with the stellar atmosphere. In this case high energy neutrinos from the decay of charged pions should also be produced. The photon interpretation, however, **has no direct experimental evidence.** It is actually questioned by the Kiel EAS results at 10^{15} eV which are not muon-poor as they should be for γ-rays and by the recent observation of possible signals of high energy muons from *Cyg*-X3 by two underground proton decay detectors[24),25)]. Fig. 27 shows the phase distribution for the muon events reported by the NUSEX - collaboration. These events cannot be interpreted as conventional neutrino interactions in the rock and are very unlikely to be produced by γ-rays. They hint a perhaps entirely new phenomenon in very high energy cosmic sources. Further investigations with underground detectors are extremely important. Our detector will combine a momentum analysis of the incoming muons with a much larger geometrical acceptance. A better separation will then be possible between the spectrum of muons associated to ordinary hadronic cascades and the potential new source responsible for the effect. It may be worth pointing out that the " image " reconstructed using the muon observations of the NUSEX group is much wider than the experimental resolution. If interpreted as an effect of the transverse momentum of the muon secondaries produced in the collision, it would imply an average p_t of about 250 GeV !

2.8.-Search for Monopoles. A search for superheavy monopoles predicted by some grand unified theories has been carried out for the last few years. Various detectors have been used including superconducting coils with SQUIDS [26)], thick scintillator detectors [27)] and other techniques [28)]. One of these experiments [28)] has probed below the Parker Bound [29)] that is set by the existence of the galactic magnetic field. From other cosmological considerations restrictive limits on the flux of magnetic monopoles can be obtained. The first limit that can be set comes from the overall cosmic mass density of the universe. This gives a limit on the average flux of

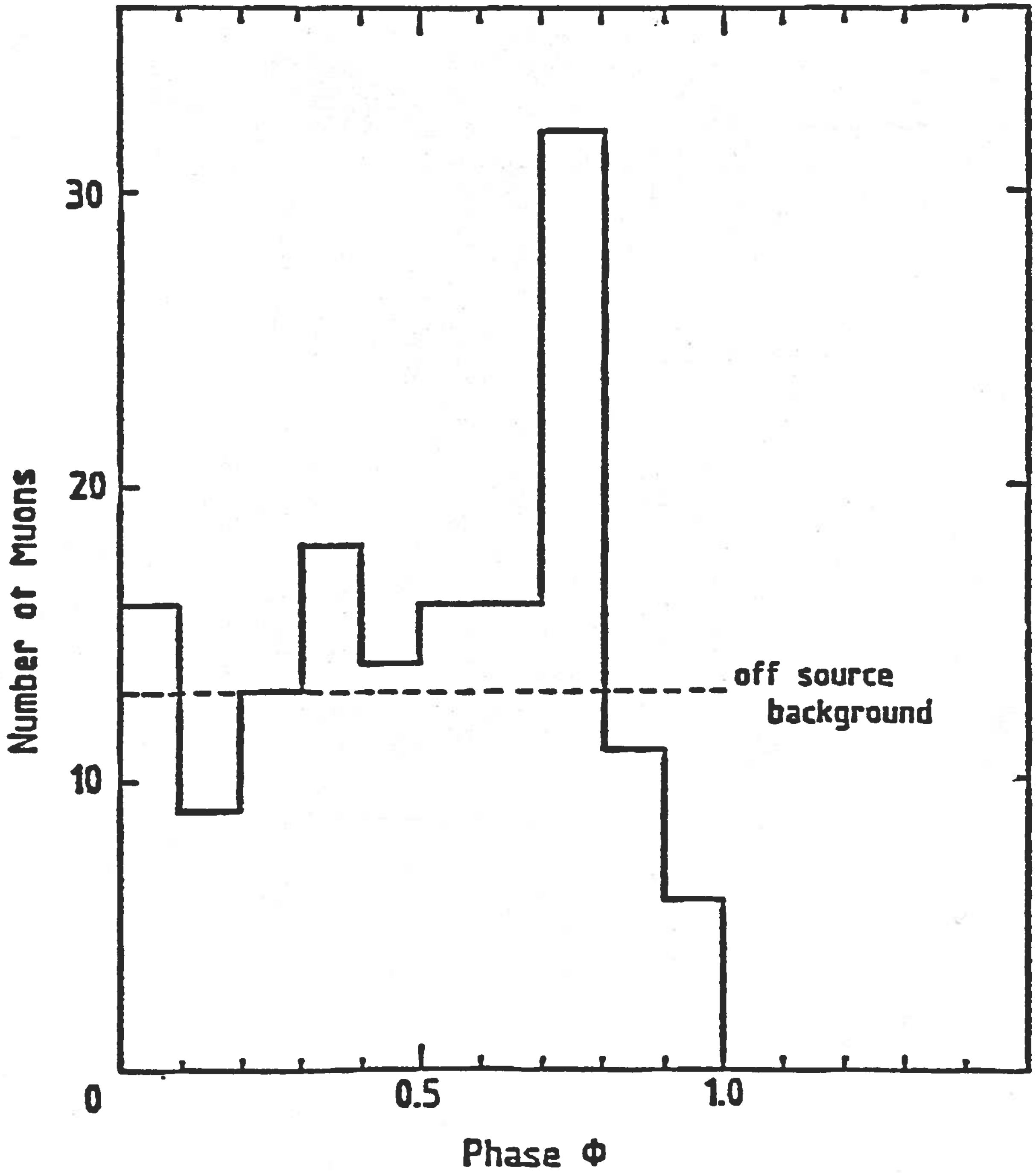

Figure 27. Main signal from the *Cyg*-X3 reported in the underground experiment of the NUSEX collaboration [25]. The signal is not due to neutrinos since it is apparent only in the angular range at shallow depths.

monopoles:

$$< F > \leq 3 * 10^{-15} [10^{16}\, \mathrm{GeV} / M_m] \;\; \mathrm{cm}^{-2}\, \mathrm{s}^{-1}\, \mathrm{sr}^{-1}$$

Of course the local flux of monopoles could be larger.

The magnetic field of the galaxy sets a limit (the original Parker limit) of[30]:

$$F_{\mathrm{Galaxy}} \leq 10^{-15} \left(\frac{M_m}{10^{17}\, \mathrm{GeV}} \right) \quad \mathrm{cm}^{-2}\, \mathrm{s}^{-1}\, \mathrm{sr}^{-1}$$

$$\boxed{M_m \geq 10^{17}\, \mathrm{GeV}}$$

$$F_{\mathrm{Galaxy}} \leq 10^{-15} \quad \mathrm{cm}^{-2}\, \mathrm{s}^{-1}\, \mathrm{sr}^{-1}$$

$$\boxed{M_m < 10^{17}\, \mathrm{GeV}}$$

The magnetic fields of rich clusters of galaxies gives a more stringent bound on the average flux[30]

$$\langle F \rangle \leq 10^{-18} \quad \mathrm{cm}^{-2}\, \mathrm{s}^{-1}\, \mathrm{sr}^{-1}$$

The magnetic fields in white dwarfs and neutron stars give even more stringent limits such as[31]

$$\langle F \rangle \leq 5 \times 10^{-24}\, \tau_{10}^{-2} \quad \mathrm{cm}^{-2}\, \mathrm{s}^{-1}\, \mathrm{sr}^{-1}.$$

where τ_{10} is the age (in 10^{10} years) of the pulsar. However, these limits are likely to be more speculative.

If we invoke the Rubakov effect of nuclear catalysis by monopoles a variety of new limits can be set[32]

$$F_{\mathrm{Galaxy}} \leq 10^{-21} \left(\frac{\sigma_m}{10^{-28}} \right)^{-1} \quad \mathrm{cm}^{-2}\, \mathrm{s}^{-1}\, \mathrm{sr}^{-1}$$

where σ_m is the cross-section for monopole catalysis (normally expected to be greater than µb's). For the cases of white dwarfs and neutron stars M. Turner points out that main sequence stars should capture significant numbers of monopoles if $M_m < 10^{18}$ GeV, and this improves the limit to [32)]

$$\langle F \rangle \leq 10^{-27} \left(\frac{\sigma_m}{10^{-28}} \right)^{-1} \mathrm{cm}^{-2}\ \mathrm{s}^{-1}\ \mathrm{sr}^{-1}$$

These latter flux limits are far below the original Parker bound and would preclude a terrestial real time detection of monopoles 32).

Another technique to search for monopoles is to use the fact that they pick up a significant ^{27}Al content as they pass through the earth. The Al + monopole system when passing through mica will cause dislocations. The null search for such "dislocation tracks" in old mica has yielded a flux limit of [28,33)]

$$\langle F \rangle \leq 10^{-17}\ \mathrm{cm}^{-2}\ \mathrm{s}^{-1}\ \mathrm{sr}^{-1} \qquad \boxed{v_M \sim 10^{-3} c}$$

This limit is subject to the assumption that the monopoles do not carry a proton already and thus reducing the effective binding potential. However, in that case the monopoles passing up through the earth would frequently be stripped and thus capable of picking up an ^{27}Al nucleus before passing through the mica.

It appears very likely that the present monopole flux limit is well below the Parker bound. In the present detector it is possible to look for monopoles through the unique ionization in the Argon detector. Using a well known geometry theorem 34) the detector is equivalent to a planar detector of 813 m^2, namely approximately the area of the proposed MACRO detector. Therefore the volume and the area detectors appear quite competitive in detecting any unknown but isotropic particle flux, namely about 10,000 m^2 sterad. At the Parker bound, 10^{-15} $cm^{-2}\ s^{-1}\ sr^{-1}$, we expect as many as 3 events /year.

A novel technique to detect monopoles if the flux is above $10^{-21} cm^{-2} sec^{-1} sr^{-1}$ and if the Rubakov effect exists, is to observe low energy neutrinos ($\sim$ 100 MeV) from the sun due to the monopoles being trapped. Thus the detection of neutrinos from the vicinity of the sun could be the best way to search for GUT monopoles 35). With the help of the proposed detector, mainly because of its large mass and the sensitivity to low energy neutrinos pointing toward the Sun, it would be possible to improve the limit to the incredible value of one million times lower than the Parker bound !

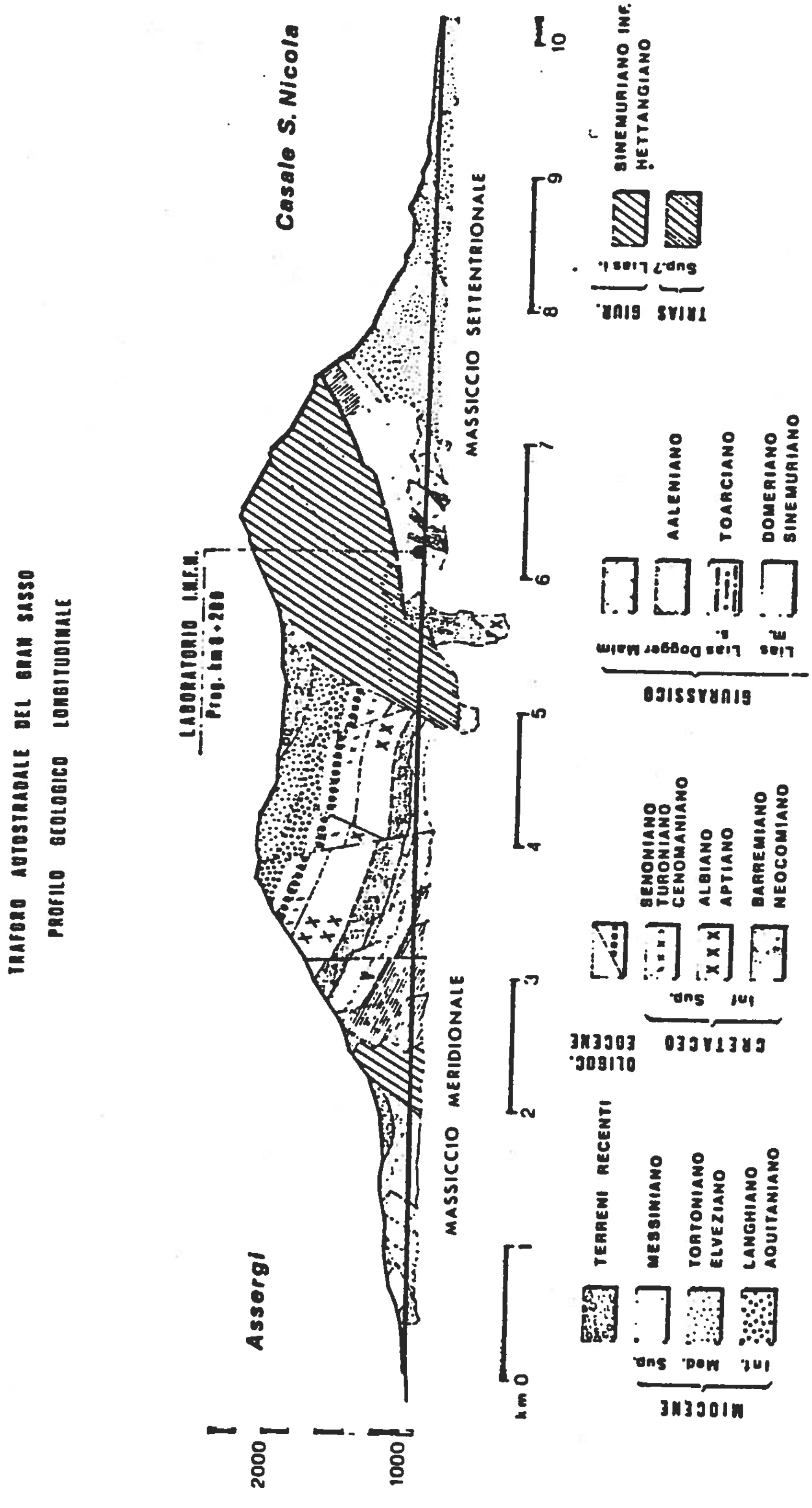

Figure 28. General layout of the Gran Sasso tunnel and the location of the laboratory.

3.-The Gran Sasso Laboratory.

The Laboratory 36) (Fig. 28) is located under the Gran Sasso mountain in Central Italy, at about 100 km from Rome. The Rome-Teramo highway traverses Gran Sasso through a 10 km long tunnel (Fig.29). Three experimental halls will be available for underground physics at about 6 km from the west entrance of the tunnel. The geographical coordinates of the Gran Sasso Laboratory are 42°27'09" North and 13°34'28" East. The minimum overburden thickness is 1500 m of rock or 4000 m.w.e. (meter water equivalent) and consists primarily of calcareous limestone ($CaCO_3$), with an average density of 2.6 g/cm^3. The geological profile of the Gran Sasso mountain is schematically indicated in Fig. 28 36).

A schematic view of the Laboratory is shown in Fig. 30. At the present time the hall A and hall B are nearly complete. Excavation of the hall C, dedicated to the present proposal, is underway. It will have a total length of 100 m and a width of 20 m. The original design of hall C has been modified to respond to the needs of the proposed experiment.

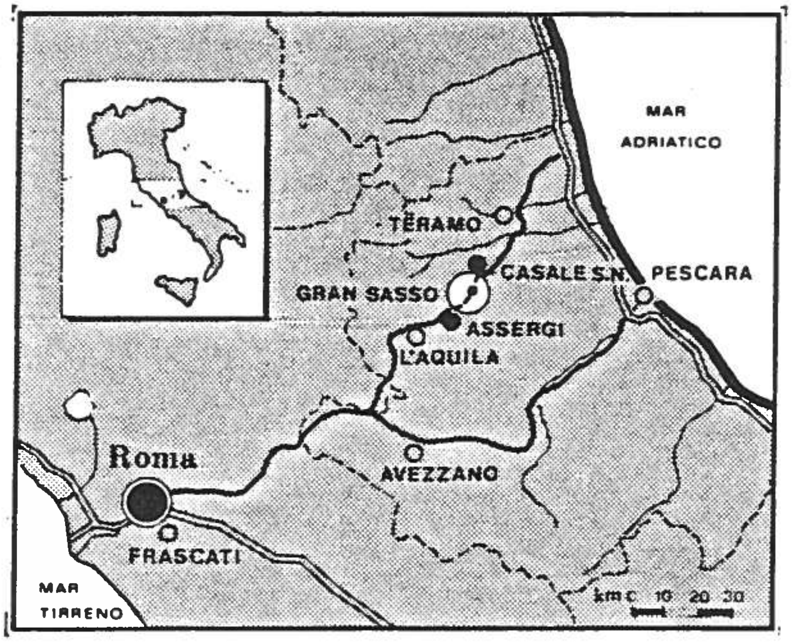

Figure 29. The location of the Gran Sasso Laboratory within Italy. The Laboratory is at less than two hours of uninterrupted Highway from the Fiumicino International Airport serving Rome. Largest lorries (TIR) can enter the Laboratory through a wide entrance, directly connected to the two-lane Highway & Tunnel.

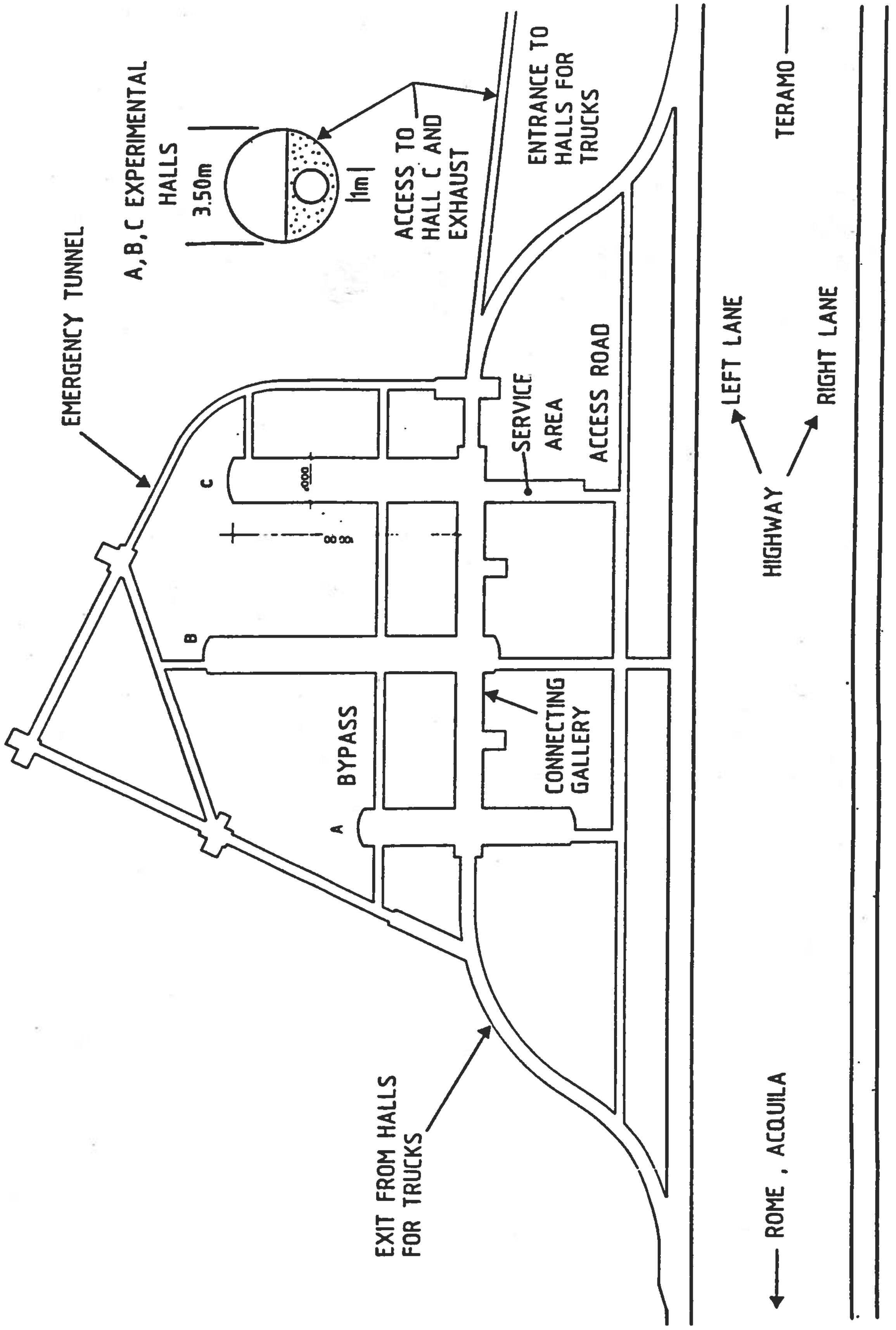

Figure 30. General layout of the Gran Sasso Laboratory.

The γ - activity of the rock in different locations of the already excavated hall B has been studied [37)] and the measured γ - spectrum reveal lines from the naturally occurring radioactive isotopes ^{214}Bi, ^{40}K, and ^{212}Pb. There is no significant dependence on the location,where the samples of rocks were collected. Due to the excellent quality of the limestone the radioactivity is remarkably low, lower than in the Mont Blanc Laboratory. Preliminary results on neutron background [38)] indicate also an extremely low activity of $< 5\ 10^{6}$ neutrons $sec^{-1}sr^{-1}cm^{-2}$.

4.- Detector

4.1. General layout. It is assumed that the new Laboratory Hall "C" (Fig. 30) will be dedicated to the experiment. The volume of the cavity is approximately 32,000 m^3. The present design responds to the needs of the present experimental proposal. Inside this structure we must locate:

1) The **detector dewar,** containing about 4500 m^3 of liquid Argon, or alternatively liquefied Methane. Also Argon-Methane mixing and Argon with a modest amount of deuterated Methane have been considered.

2) The **storage dewars,** in which the cryogenic liquid can be transferred and dumped, would such a need arise.

3) The **magnet coil,** generating an horizontal magnetic field of about 0.5 Tesla, with the associated power supply and water cooling equipment.

4) The **external muon identifier,** a set of large area muon detectors in order to determine the direction of high energy tracks by time of flight.

5) The **cooling and purification equipment** for cryogenic liquids. Heat losses of the dewar are not negligible and must be compensated. Furthermore, since purity must be kept extremely high, continuous purification of the target material in liquid form is performed .

A schematic view of the laboratory hall with the different detector components is shown in Fig 32 .

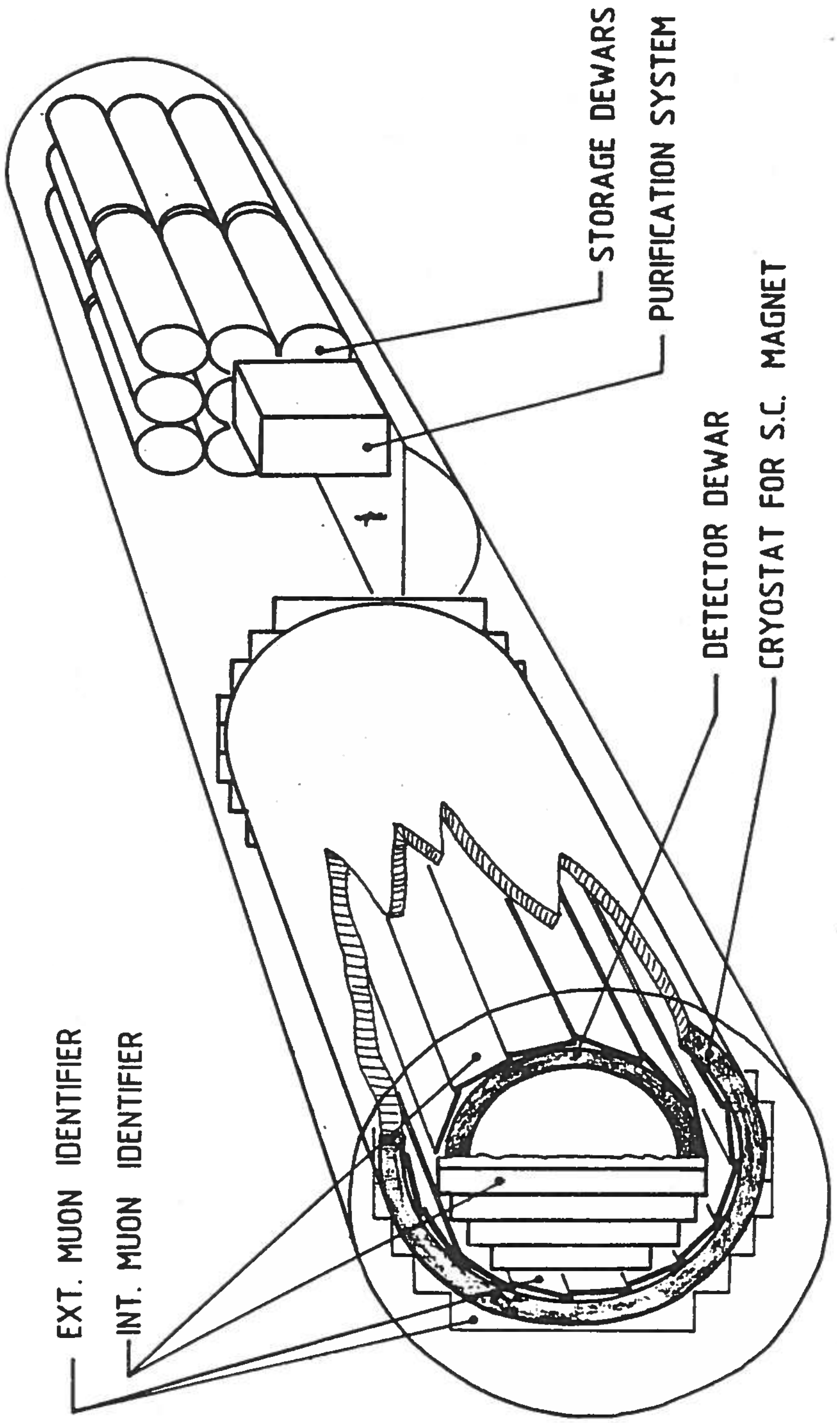

Figure 32. Artist's view of the ICARUS detector.

For safety reasons, the storage dewars are located at a lower level, in order to make use of gravity to dump the liquid in the alternative that all other methods should have failed. These dewars are kept cold at all times in order to insure that the transfer can be performed rapidly and without significant boiling of liquid.

The shape of the detector dewar is roughly cylindrical, of about 14.0 meters external diameter and 30 meters long. The major axis is horizontal. Once the steel structure is welded in place, access to to its interior is made possible by a number of men port holes. Since the inside of the detector must remain extremely clean and free of dust, a special SAAS entrance facility is needed. Plenty of space must be left around the dewar for the solenoid and the external detectors. It is envisaged to support the main dewar (the weight is in excess of 5000 tons !) on pillars resting on the bottom floor of the cave.

A considerable amount of empty unused space must be left around the detector. This might seem at first sight as a considerable waste of resources. In fact this is not so, since the excess volume of the cavity is essential for a safe operation of the cryogenic equipment, reducing the shock of a sudden overpressure produced by accidental spill of a large amount of cold liquid, vaporizing immediately on contact with materials at room temperature.

The 30 m long detector will be placed at the far end of the 100 m long hall. During construction the remaining space will be used to assemble the major detector items (e.g. winding the magnet, constructing the dewar, etc.). After the large detector parts are installed this space will house the storage dewars and the cooling and purifying system . Access is possible only via an entrance port, located in the upper part of the cave in order to insure that no liquid can escape outside the cavity. **Multiple, hermetic doors** must insure that the whole cavity may become highly overpressurized by an accidental spill of cryogenic liquid with no detectable effect for the environment of the main laboratory and for the road tunnel. These doors must be constructed such as to close automatically under the effect of the overpressure and such as not to open when such an overpressure exists. They must withstand the pressure resulting from the evaporation of the whole liquid. They are the main protection element in case of a catastrophic accident. Safety depends primarily on their operation !

An exhaust pipe of about 1.0 m diameter and 4.5 km length is foreseen in order to expel the gas in case of necessity. This pipe will be an independent tube running in a separate access tunnel directly out of the Laboratory. Alternatively, we are considering making use of a pipeline of the type used for oil drilling, connecting directly the top of the mountain to the Laboratory C. A special drilling technique must be used in order to insure that the pipeline is aiming precisely at the Laboratory's Hall C. A feasibility study has been carried out for us by AGIP-ENI, the nationalized Italian oil company.

Human access to the main cave will be severely restricted during the data taking periods with cryogenic liquids. In the case of Methane, it may be advisable to remove the Oxygen in the whole cave, flushing the air in the cavity with Nitrogen or Argon. Fresh air can be established in few hours, with the help of the ventilation of the tunnel capable of providing as much as 80,000 m^3/hour of fresh air. During the flushing operations of the atmosphere of the cave, the air-inert gas mixtures can be evacuated through the exhaust pipe or if in not too large a quantity, dumped directly in the tunnel, after diluting it with many volumes of fresh air in order not to impair the quality of the underground environment.

We now proceed to a detailed dicussion of all the major components of the ICARUS detector.

4.2.The principle of operation of the Cryogenic Imaging Chamber.

The imaging of the ionizing events inside the cryogenic volume of the detector is made possible because of (1) the long lifetime of the drifting electrons (in excess of one millisecond) and (2) the sensitivity of modern FET-input charge sensitive amplifiers that are capable of sensing an electron signal produced by a few millimeters of minimum ionizing tracks. The read-out of the information therefore follows very closely the techniques used traditionally in the case of ionization chambers, since in both instances there is no gas amplification. However the read-out cannot be simply a charge collecting process, since a **non-destructive** read-out is necessary to insure a simultaneous imaging in at least three different views and the determination of the so-called $t = 0$ signal which provides the measurement of the drift time and hence of the distance travelled by the drift electrons.

A short survey of the theory of charge image effects is now given, following closely the classic discussion of the case of a proportional chamber. The process of imaging with cryogenic liquids can be easily understood starting with a simple geometry of two planar electrodes at distance d with a potential difference V, imersed in a medium, either liquid or gas (Fig. 33). Let us assume that electrons can move freely under the influence of the electric field E, with a constant drift velocity $v_d(E)$ and that they have no appreciable attachment to impurities.

The effect of a charged particle passing through the liquid on the external circuit can be estimated from the "work" performed by the electric field in order to keep the charges moving:

$$dW = E\, e\, (v^{+} + v^{-})\, dt = V\, i_{o}\, dt$$

where i_o is the current in the circuit. This relation can be written as :

$$i_{o} = e\, (v^{+} + v^{-}) / d$$

Since the electron mobility is several orders of magnitude larger than the one of positive ions, only electrons will contribute significantly to the current :

$$i_{o} \sim e\, v^{-} / d$$

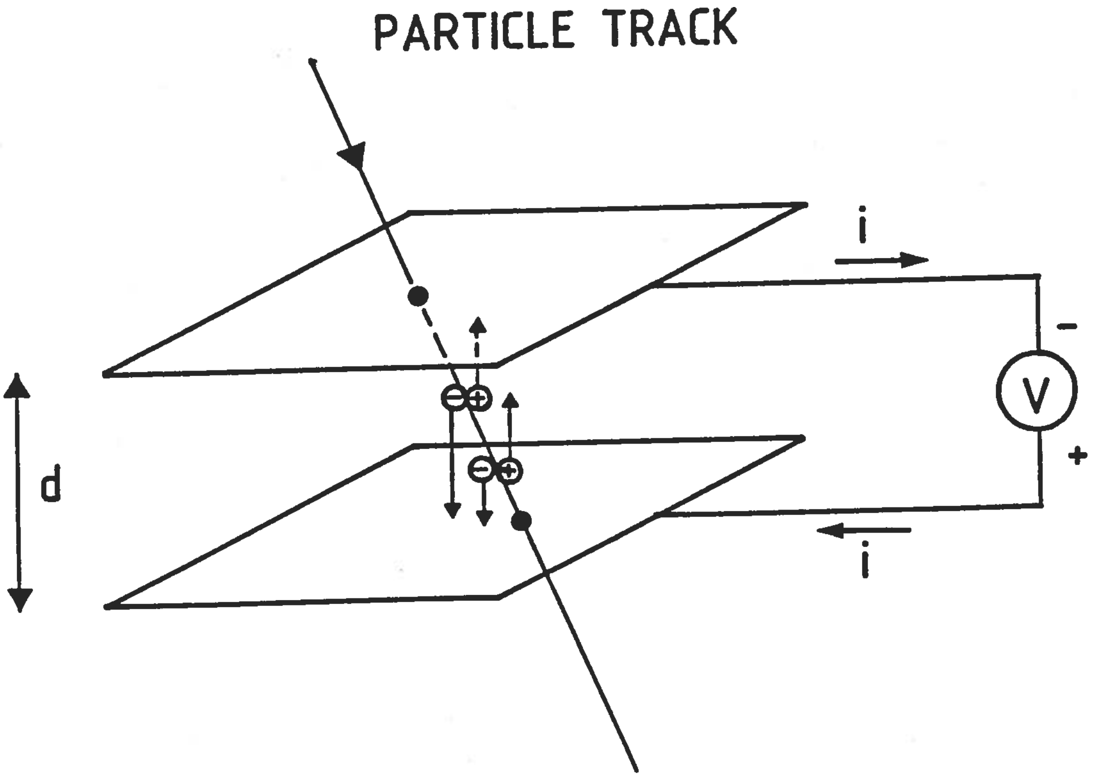

Figure 33. Schematic diagram of a pair of electron-ion produced inside a plane electrode detector. The current flowing in the power supply is observed.

The signal observed from a single electron starting at position x within the gap is then :

$$Q^{-}(x) = \int_{x}^{d} i_{o} \cdot dt = e \cdot \frac{v^{-}}{d} \cdot \frac{(d-x)}{v^{-}} = e \cdot \frac{(d-x)}{d}$$

Note that the signal $Q^{+}(x)$ produced by the positive ion starting at the same place is :

$$Q^{+}(x) = e\, x / d$$

which insures that the sum of $Q^{+} + Q^{-}$ is always one elementary charge. Because of the much smaller mobility of ions, the signal Q^{+} is spread out over a much longer time, which makes the possibility of imaging with positive charges unpractical.

If the collecting electrode is electrically subdivided into several, separate segments (Fig. 34), the current flowing through each segment of area ds at a distance r is :

$$di \sim ds / r^{2}$$

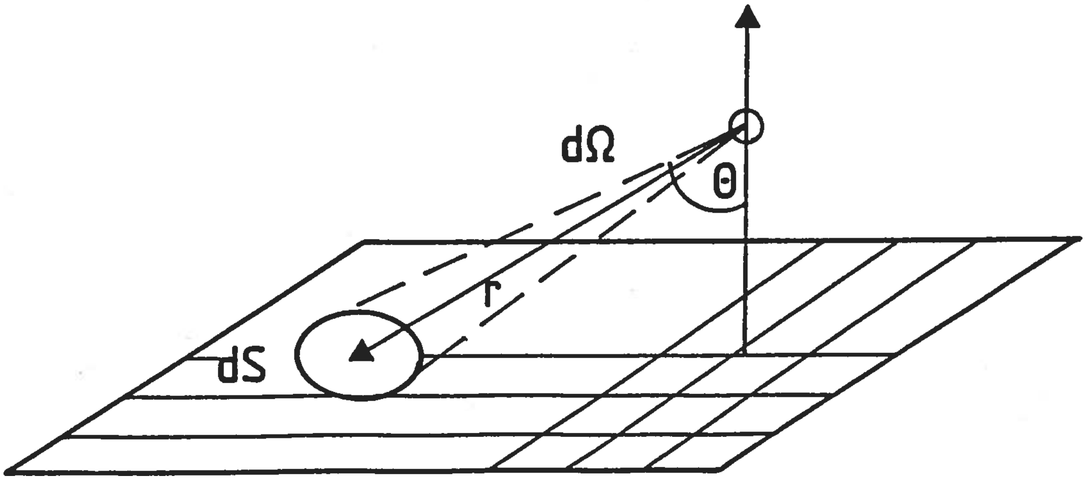

Figure 34. Collection of image charges from a segmented electrode.

As the solid angle of a segment is given by :

$$d\Omega \sim ds / r^2$$

then the current through ds is proportional to the solid angle $di \sim d\Omega$. We remark that the signal is due to the images of the charges of the electrons and is not produced (as sometimes incorrectly assumed) by a simple electron collection.

If we replace solid electrodes with wire planes or grids, we can preserve the electrons and we can realize a non - destructive read-out. The transparency of a grid to electrons drifting along field lines has been calculated in the literature and it is a function of the ratio of the fields E_P and E_Q in front and after the grid respectively and of the ratio $r = 2\pi r/d$, where r is the wire mesh radius and d the wire spacing. The curve is given in Fig. 35, taken from Ref. 39. For equal field values at both

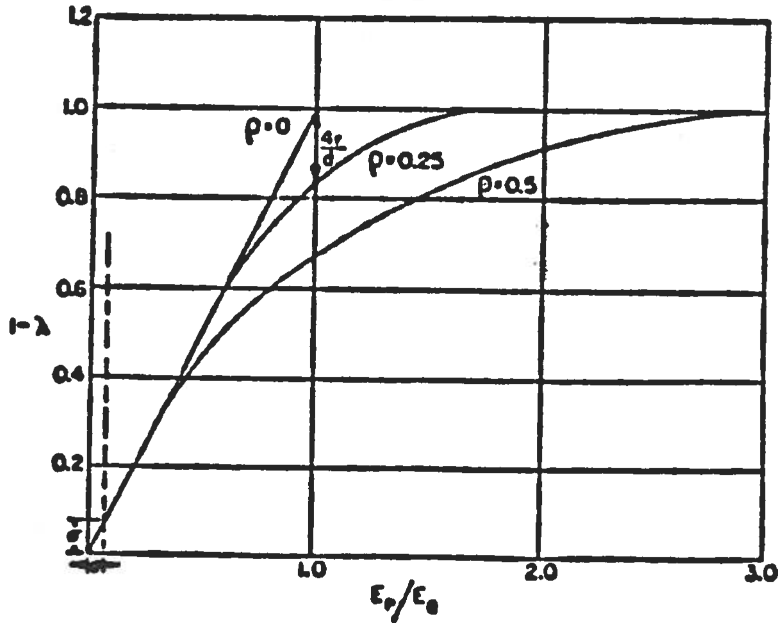

Figure 35. Fraction of field lines which do not intercept the grid[39].

sides of the grid, namely $E_P = E_Q$, the transparency is given by 1-4r/d, namely exacly **twice** the geometrical cross section of the grid itself. For fields after the grid E_P, significantly larger than the field E_Q before the grid, the following condition must be satisfied:

$$\frac{E_P}{E_Q} > \frac{1+\rho}{1-\rho} \qquad \boxed{\rho = 1 + \frac{2\pi r}{d}}$$

This condition has to be balanced against the requirement that the grid is providing an efficient shielding of the electric field perturbations.If we define as the shielding effect of the grid the fraction of field change in E_Q which is reflected on E_P, namely $\sigma = dE_P/d\,E_Q$:

$$\sigma = \frac{dE_P}{dE_Q} = \frac{d}{2\pi p}\log\left(\frac{d}{2\pi r}\right)$$

Where p is the distance between the grid and the next electrode, assumed to be continuous. Curves of constant grid inefficiency are shown in Fig. 36. Note that inefficiencies of a few percent are acceptable .

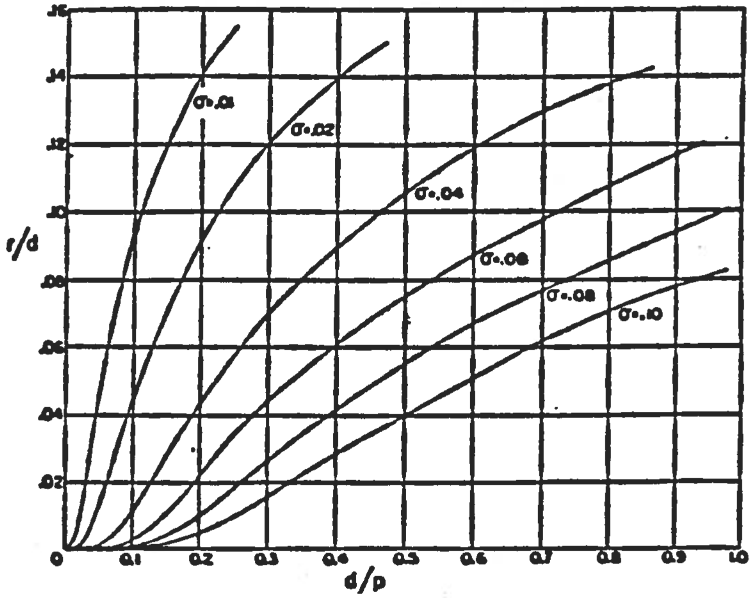

Figure 36. Curves of constant inefficiency s for a grid (Ref. 38).

A typical geometry of a read-out with three consecutive wire planes is shown in Fig. 37. The corresponding field line distribution for this example is given in Fig. 38. The electrons will follow the field lines, and the very same electrons can be sensed in a succession of several planes of stretched wires. While approaching the plane, electrons will induce on each plane a charge. When electrons are moving away, of course the opposite charge will be recorded. After integration, the resultant pulse is approximately triangular in shape (Fig. 39).

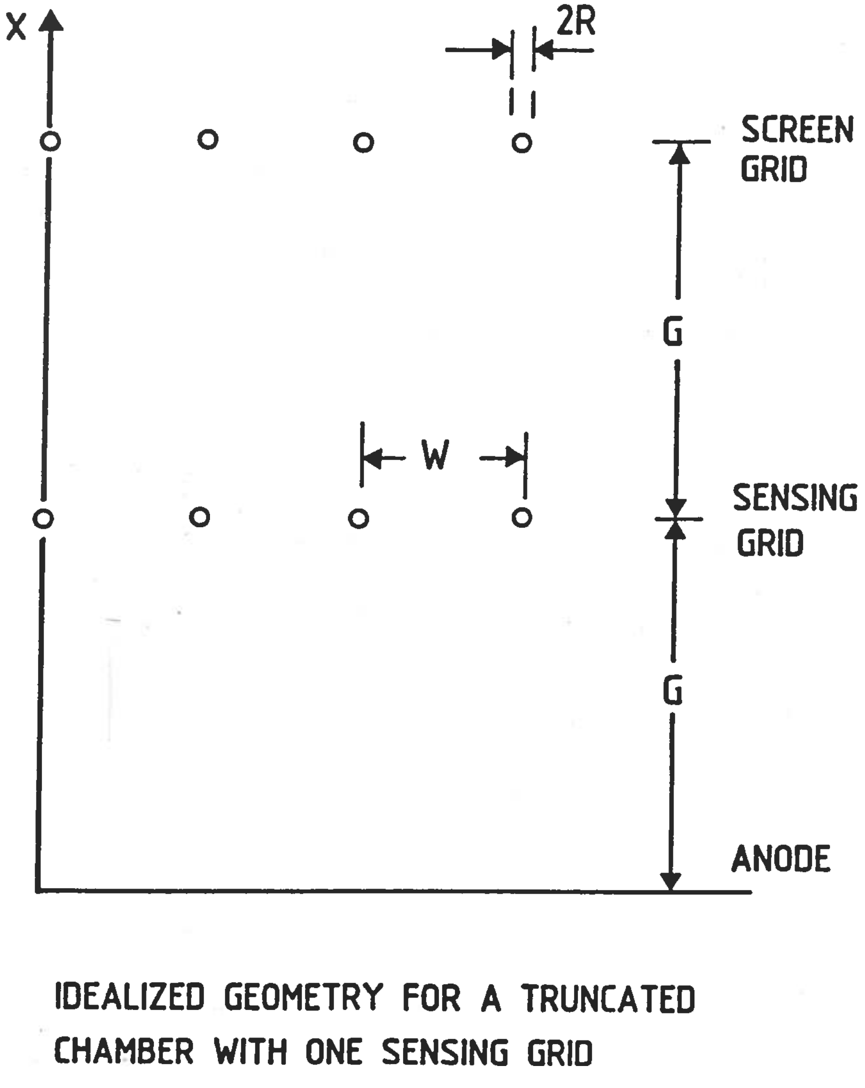

Figure 37. Typical electrode configuration for a read-out plane . The first grid is used to shield the sensing grid which follows . The last electrode can be used to collect the electrons, or may be another read-out.

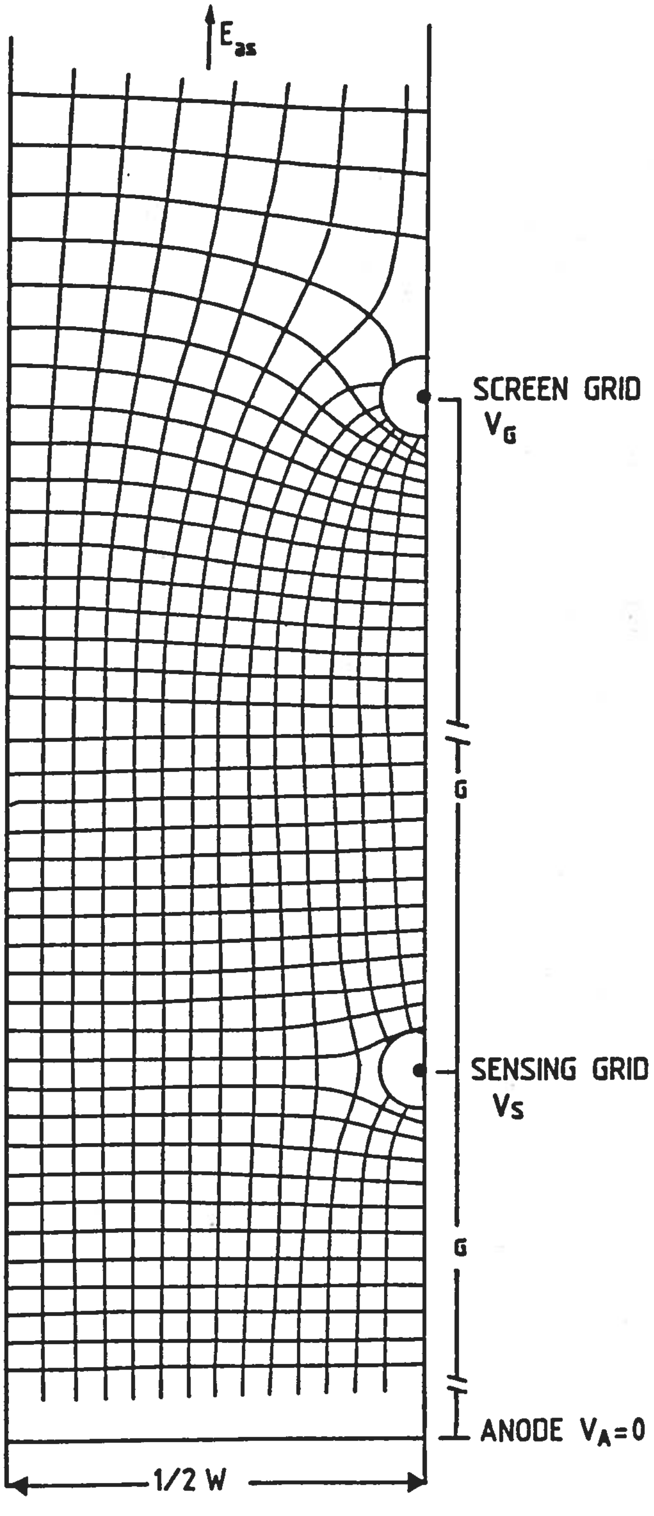

Figure 38. Field line configuration for the grid geometry of Fig. 37.

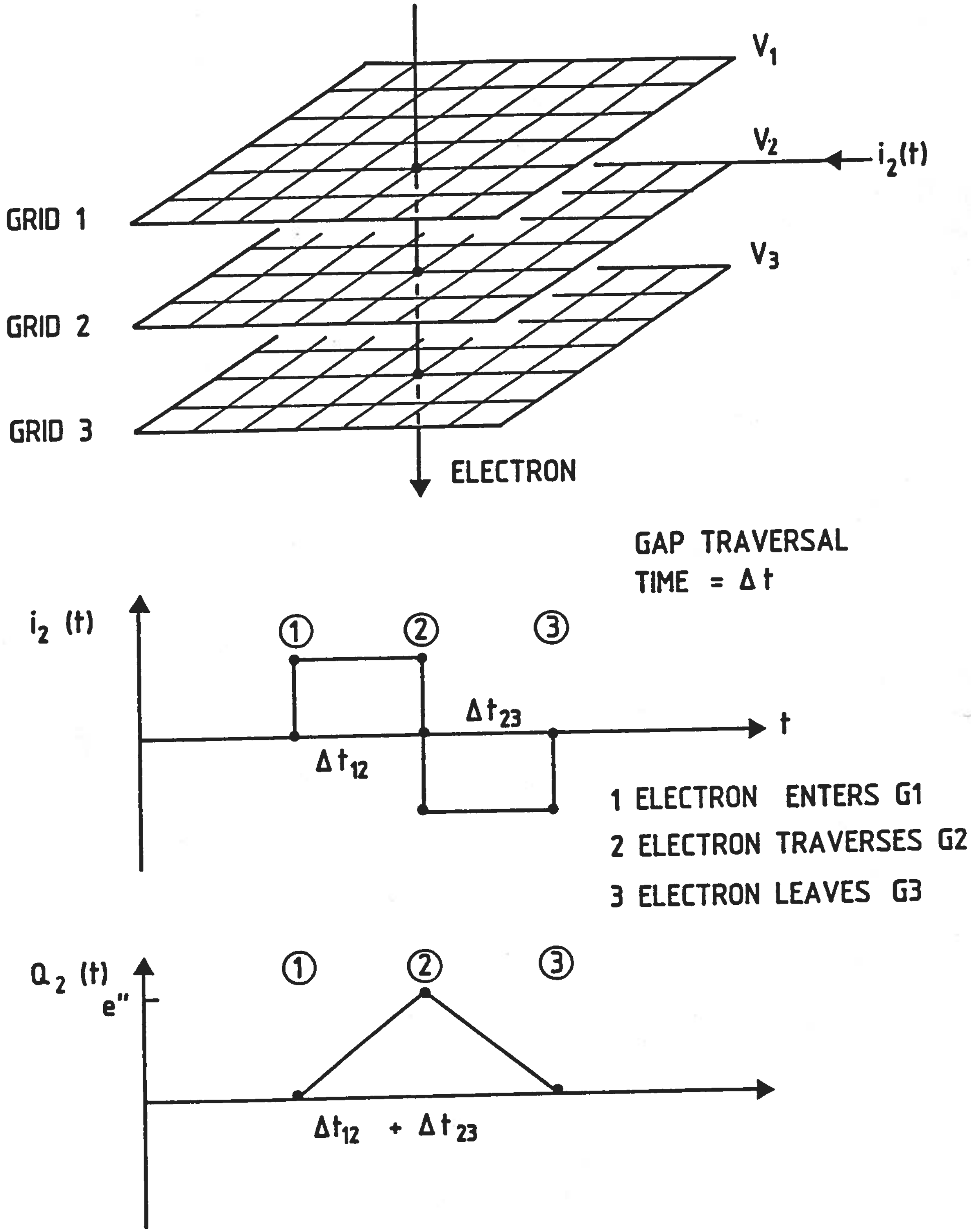

Figure 39. Principle diagram of pulse formation by imaging the drifting electrons on a transparent grid (non-destructive read-out).

A detailed analysis of the induced signals for the geometry of Fig. 40 has been performed by Gatti et al. [39]. The expected signals of tracks are shown in Fig 41a. The parameter in the diagram is the height h (in units of wire spacing W) of the start point above the first plane. For different incident angles θ of inclined tracks the pulse shape is given in Fig. 41b. The obtained space resolution is shown in Fig. 42a and the signal to noise ratio in Fig. 42b. In this analysis, filters were applied to the signals to improve the signal to noise ratio. Note that no pulse shaping is foreseen for the proposed read-out. However, the filter functions can be applied by software on the digitized data. This digital filtering has the advantages that even for very long signals the true waveform is recorded and that the function applied to the data can be optimized depending on the inclination of each track. The signal of the first plane is " prompt ", i.e. it starts at the moment in which the ionizing particle traverses the chamber. Therefore the initial time t_0 of the event is also recorded.

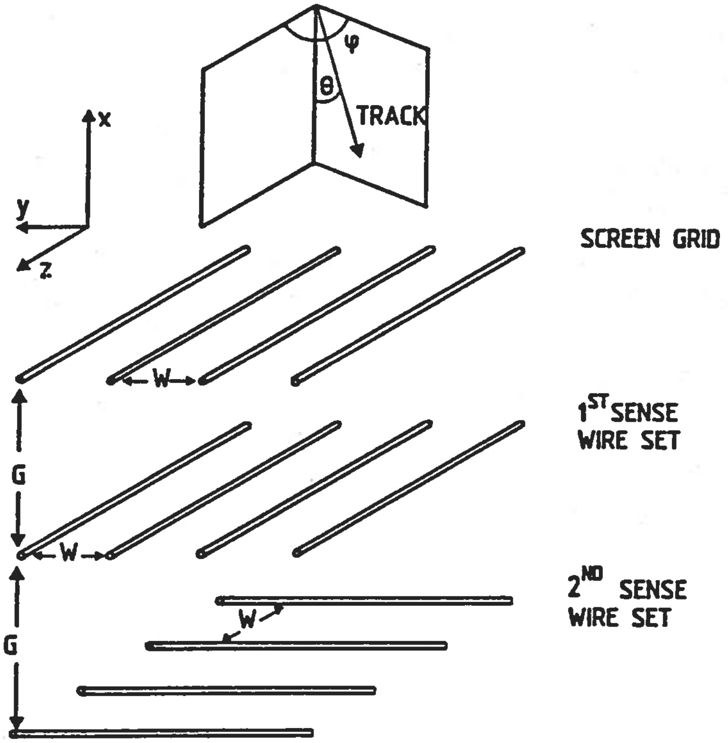

GEOMETRY OF THE GRIDS AND REFERENCE FRAME

Figure 40. Geometry of the grids and reference frame used in the calculations of Ref. 39.

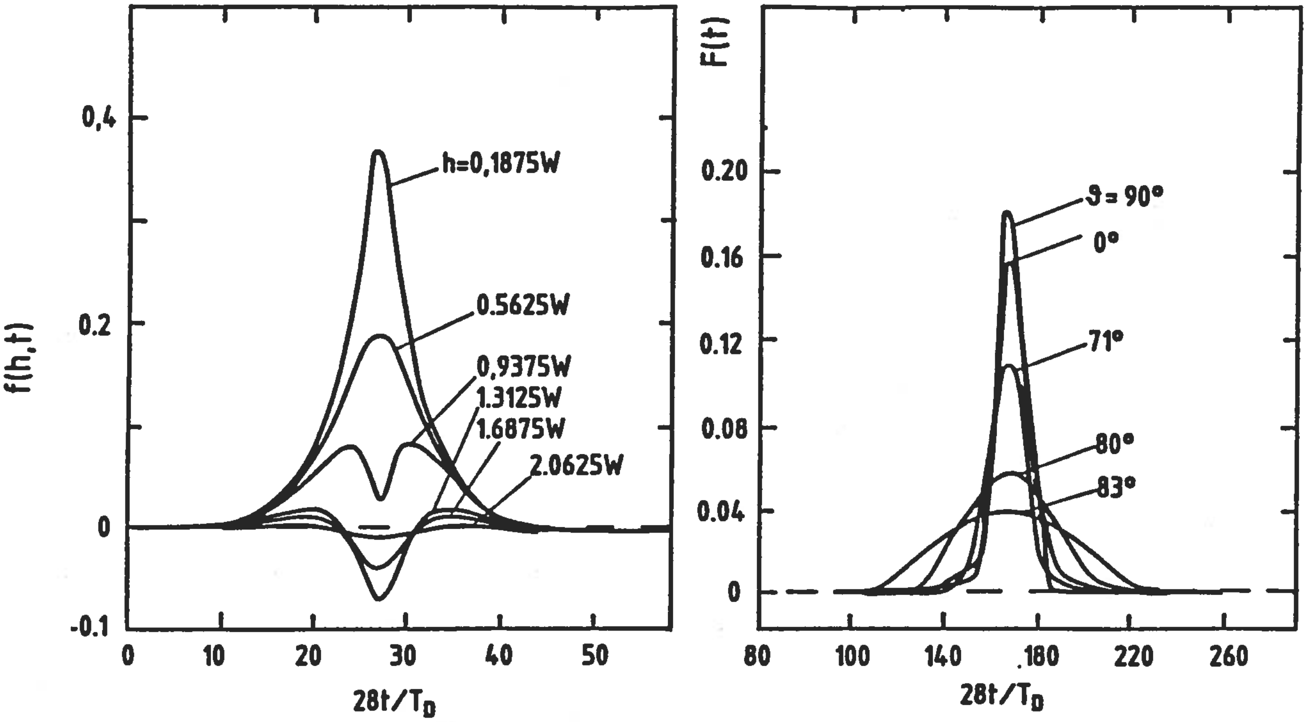

Figure 41. (a)Pulse shape according to hit position of the track,in units of grid spacings; (b) as a function of the incidence angle θ (see Fig. 40).

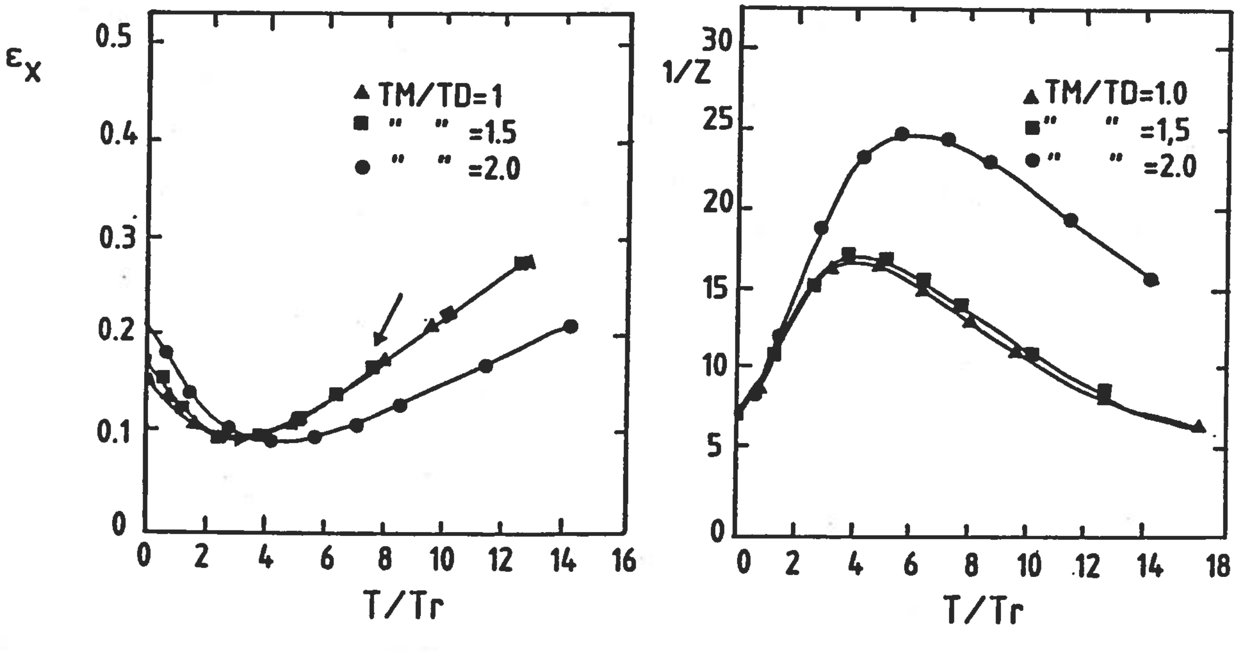

Figure 42. (a)Spatial resolution ε, for different values of shaping parameters. Units of e are millimeters; (b) signal to noise ratio 1/Z, for minimum ionizing track and optimal filtering and small electrode capacitance.

For Liquid Argon chambers with very high spatial resolution [40)] the diffusion of the drifting electron cloud has been studied. The width s of the electron cloud will grow with the path d according to :

$$\sigma = D\cdot\sqrt{d} \qquad \text{with} \quad D = .28\ \mu m/\sqrt{mm}$$

Even for a maximum drift path of 2.3 m and a low field of 1 kV/cm the diffusion will stay below 2 mm corresponding to our wire spacing.

4.3. Read-out geometry of the Image chamber. Mechanical stability considerations suggest that the shape of the detector should be cylindrical. The detector has the dimensions of 14 m diameter and 30 m length. The read-out electrodes, the cathode planes, and the field-shaping wires are mounted in this cylinder. The number of read-out planes is determined by the maximum drift length which is considered to be acceptable. A maximum drift length of 2.3 m corresponds to a geometry with three planes parallel to the cylinder axis and with drift spaces on both sides. In order to achieve such a drift path an impurity concentration in the Argon of less than 0.6 ppb Oxygen equivalent is required. This valuecan be easily reached according to the results of the tests with Liquid Argon chambers at Harvard (Appendix II) .

The electrodes have to be designed as self-supporting structures to avoid severe problems arising from different thermal contraction of the chamber vessel and the wire material. The read-out planes will be parallel to the cylinder axis of the dewar. Three planes are foreseen with separate sense wires for the two sides of the plane. The diameter of the detector will thus be divided in 3 x 2 drift-spaces of 2.3 m length. For each drift-space 3 wire planes (Fig. 43) will measure the coordinates; one direction will be parallel to the cylinder axis, the other two have stereo - angles of 15°.

A shielding grid will separate the sense wire region from the drift space. The signals of these grids are also read out. They will be used to define the start time t_0 of an event, as they are prompt signals starting as soon as the ionization electrons begin to move in the field. The capacitance of this grid must be kept very low in order to detect signals corresponding to a small energy loss in the sensitive volume. This is achieved by placing the first grid at a significant distance (of order 10 cm) from the rest of the read-out electrodes. The charge output for a number of typical cases is

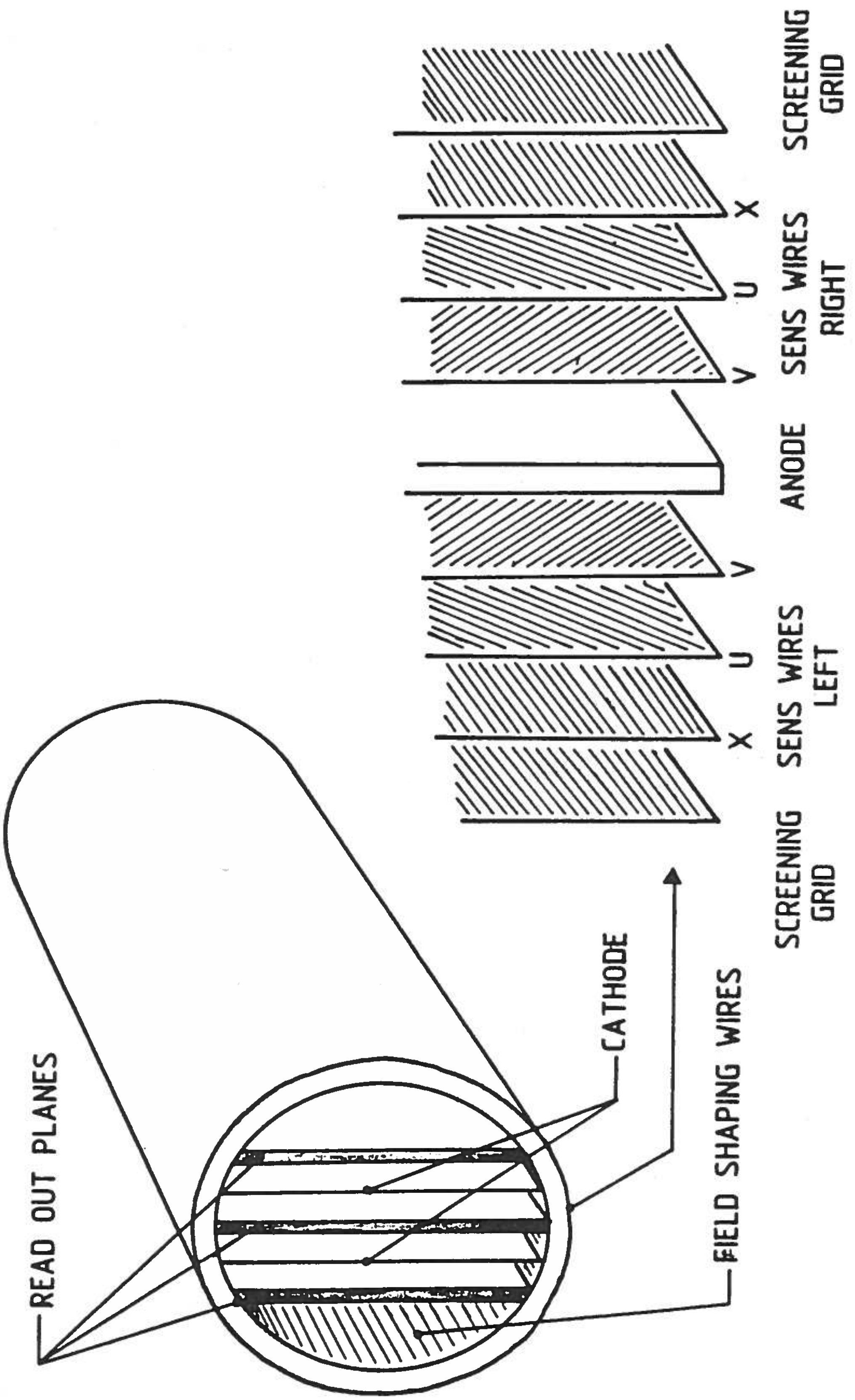

Figure 43. Layout of read-out planes and cathodes in the detector dewar.

listed in Table 7. As soon as the event has occurred a current starts flowing in the grid, given by $i_o = Q\,v^-/d$, where Q is the total charge deposited by the event, v^- is the electron drift velocity and d is the gap width. In our case $d/v^- \approx 10^{-3}$ sec, and in the time of the order of 2 μsec only 1/500 of the charge delivered is collected through the grid. For an electron of 4 MeV we have a signal equivalent to 200 electron charges, which is too small to be detected! Of course the signal current is continuing to flow and on a longer time scale, a larger charge is collected. Therefore the precision of the $t = 0$ determination and hence the localization of the event inside the tank is a function of the amount of energy lost. For instance if we wish to determine the position of the electron of the previous example to about ± 2 cm we can choose a timing window of 40 μsec and therefore collect as many as 4000 electron charges in the case of a 4 MeV electron. Of course the trigger does not depend on the detection of a $t = 0$ signal from the grid, since the information is continuously recorded by the read-out and stored in a memory . The trigger is then generated with the help of a fast processor which searches for a specified pattern in the read-out of the event images.

Table 7 .Typical signal levels collected by the detector

Type of event	# of Electrons	Collected Charge
2 mm long track	12,000	2 fC
10 MeV electron	250,000	40 fC
P Decay (900 MeV)	$2.2 * 10^7$	3600 fC

Let us now consider the read-out electrodes for the imaging of the event (Fig. 43). There are three main read-out planes, each collecting information from both sides. The grid structure is also shown in Fig. 43. The length of 30 m, the wire spacing of 2 mm, and the drift length of 2.3 m represent a volume of about 0.14 m^3, which is read out by one wire. Thus 4500 m^3 result in 33,000 wires for each

Table 8. Main Parameter List

Parameter	Value
Active Volume	4600 m^3
Diameter	14.0 m
Length	30.0 m
Number of Planes	3 x 2
Drift Length	2.30 m
Stereo Angle	10 degrees
Drift field	1.0 kV/cm
High Voltage	230 kV
Max. Drift Time	1.2 msec
Number of Channels	100,000
Spatial Resolution	2.0 mm
Magnetic Field	2.0 Tesla
Total Memory	200 Mbytes

direction or a total of 100,000 electronic channels. The distance between consecutive read-out wire planes is 2 mm and the potential difference about 300 V. With a wire spacing of 2 mm and 100 mm wires the grids are largely transparent to drifting electrons. The pulse of a single electron is 0.87 μsec.

4.4. Mechanical Design. The mechanical design of the detector is strongly influenced by the requirement of installing such a gigantic device deep underground. In particular the dewar and the detector components must be assembled out of smaller parts which can be transported through the access tunnel .

In order to keep the leak and out-gassing rates to a minimum and to provide for the necessary mechanical strength, the liquid has to be contained in an all-welded stainless steel or Aluminum vessel with as few ports as possible. We prefer the solution of man-holes to the possibility of a large removable flange which permits full access to the components inside the dewar, since the extreme cleanliness conditions require a special access procedure. This means that a major disaster, which would require to replace a large component of the inside cannot be corrected without cutting and rewelding the main dewar.

The cathode planes will be grids stretched in self-supporting frames. Around the sensitive volume of the detector, field-shaping wires will insure a homogeneous drift field. The sense-wires will cross the detector in the full length of 30 m. A mechanical support has to be provided every few meter to avoid a displacement of the wires under the influence of gravity and the electric field. The sense-wires can be thick (~100 μm) compared with typical gas wire chambers, as there is no gas amplification.

Another important requirement to the design of the detector comes from the thermal contraction from room temperature to the one of Liquid Argon. A 30 m long stainless steel wire will contract as much as 160 mm because of the thermal effect. Clearly the consequences of using different materials with different expansion coefficients has to be studied very carefully. Individual read-out wires must be kept under tension using a spring loaded device. Likewise the high voltage and the read-out planes must not deform under the cool-down and their contraction (as much as 10 cm for a 17 m long plane) must be accomodated by the supports. It is also very important to insure that the actual positions of the read-out planes are accurately known, when cold, to about few hundred microns.

Finally a very large number of feed-through connections must be made between the inside of the tank and the outside world. Simple glass-Kovar feed-throughs are adequate and relatively cheap. However, they must be placed in such a way that if one of these devices actually breaks, there should be no appreciable leak of liquid. Therefore the feed-throughs must be concentrated in the region immediately above the tank.

4.5. Cryogenics and Purity . The main dewar must be well insulated thermally to insure a modest liquid boil-off. The most obvious solution would be the one of using a vacuum insulation between the dewar and the ouside. Although in principle such solution is possible, the extraordinary dimensions of the tank may transform such an immense evacuated volume in a potential hazard unless appropiate measures are taken. Therefore the possibility of other types of insulation, like perlite, have been considered. The heat leak of a perlite insulation is considerably larger, of the order of 4 Watt/m^2 . The area of the tank is about 1650 m^2, and the corresponding leak rate is 6.5 kWatt, equivalent to about 100 l/hour of liquid boil-off. If in itself this seems to be a large number, in actual fact it represents only a very tiny fraction of the liquid inside the tank, corresponding to a lifetime of the tank of 42,000 hours, or 4.8 years !

The heat losses of the dewar must be restored by boiling off some Liquid Nitrogen. The liquid may either be manufactured inside the tunnel with a liquefier (of about 600 kW power consumption) or preferably brought in periodically from the outside. A standard 10 m^3 dewar could then suffice for some 100 hours of operation.

One of the main problems in constructing a large volume cryogenic detector as described here is to guarantee the high purity level of the liquid. Tests with a small Liquid Argon chamber at Harvard (Appendix II) showed that this problem is not as severe as assumed in the past. The experience from these tests can be extrapolated as a guideline for a large detector. The surfaces in the test chamber consisted of about 87% stainless steel, 11% ceramic, and 2% other materials (e.g. electronic solder). The ratio of steel surfaces to all the other surfaces will be about the same in a 4500 m^3 detector. New materials which were not used in the test chamber have to be tested for out-gassing. Comparing steel surfaces will give a good estimate of the out-gassing rate. In the small chamber the out-gassing rate was $5.2 \cdot 10^{-12}$ torr l / sec / cm^2. In the 4500 m^3 detector the surface will be in the order of 2000 m^2 including the chamber vessel, wires of read out planes and cathode grids. The expected gas flow into the volume by out-gassing will be therefore in the order of 10^{-4} torr l /sec, which is negligible. Out-gassing will be an even smaller effect in a large detector due to the fact that impurity concentrations are reduced according to the volume, while out-gassing increases with the area.

Argon in quantities needed to fill the detector will be shipped from the supplier in a liquefied form. We assume a " raw " Argon with an impurity level of about 10 ppm Oxygen equivalent. For a filling time of the detector of one month, the purification system has to be capable of handling about 1 liter/sec of liquid. Such a flow rate is also largely sufficient to insure the steady purification during normal operation. Comparing this system to the purifier of the tests at Harvard, we need at present a flow rate 400 times faster for a volume $4.0 \cdot 10^6$ times larger.

Purification will proceed in two steps. First, the bulk of Oxygen will be removed; afterwards the residual impurities (e.g. O_2 , H_2O , CO_2, etc.) will be brought below the 1 ppb level. In the first step, Argon is passed through a material which can be easily oxidized (e.g. NaK, Oxisorb[4], reduced Magnesium-Oxides or the like). The second step relies on the strong absorption of electro-negative impurities by molecular sieves. This technique will be also the used for the re-circulation of the liquid during operation. Molecular sieves are used in large quantities in industrial processes. After usage, they are usually regenerated by baking them out at high temperature (250 °C) under vacuum .

4.6. Electronics and read-out. Unlike gas detectors, a liquid imaging chamber has no amplification around the sense wire. Much smaller signals have to be detected. The minumum ionizing track segment of 2mm length, which is the smallest information signal to be collected by sense wires corresponds to about 12,000 electrons. A low noise charge-sensitive pre-amplifier is connected to to each wire. The amplifier has to integrate the signal from the pick-up grid in order to obtain an approximately triangular signal due to the image charge effects of the electrons passing near by. Special care has taken in designing the amplifier and in matching it to the sense wires. There are two important design parameters, namely :

(1) matching between the source and the amplifier and
(2) low noise.

Sense wires have an impedance of about 50 - 100 Ω and a capacitance of 50 - 100 pF / m, and they are approximately matched to the input impedance of the amplifier, which is purely resistive and given by :

$$Z = \frac{1}{\omega_0 C}$$

where ω_0 is the frequency of unit gain and C is the capacitance in the feed-back. For $f_0 = \omega_0/2\pi$ = 900 MHz and C = 1 pF we find Z=170 Ω which is adequate. Therefore even very long pick-up lines like in our application are acceptable. Note that the propagation time over a 30 meters long line in the liquid Argon is about 100 nsec and therefore multiple reflections can significantly alter the pulse shape.

In order to optimize the signal to noise ratio, the input capacitance of the amplifier C_F should be comparable to the capacitance C_D of the sense wire, typically 1000 - 2000 pF. Ordinarily, FET input amplifiers have input capacitances of the order of 15 - 30 pF, which is too small. A step-up transformer is sometimes used to improve the matching. Then the apparent input capacitance is scaled up like N^2, where N is the transformer ratio, and the charge of the signal is reduced by the factor N , resulting into a signal to noise dependence for $C_F << C_D$ of the type $[C_D]^{-1/2}$ rather than $[C_D]^{-1}$. This theoretical prediction is very hard to acheive in practice, since it neglects the stray capacitance of the transformer itself. In our case the necessity of recording long pulses and the presence of the strong magnetic field makes the use of a transformer not practical. Instead we prefer to use an input stage with a large input capacitance obtained using appropriate type of FET and whenever necessary a number of FET's in parallel. A very interesting device is the new (and inexpensive) 2SK147 produced by Toshiba. This FET has a very low noise figure down to very low frequencies, namely 1 dB at f = 1 Khz and 5 dB at f = 100 Hz, and a large input capacitance, typically 75 pF. We have performed extensive studies on such a FET in a cascode, charge integrating configuration (Fig. 44).

" PRODUCTION" Preamplifier Scheme

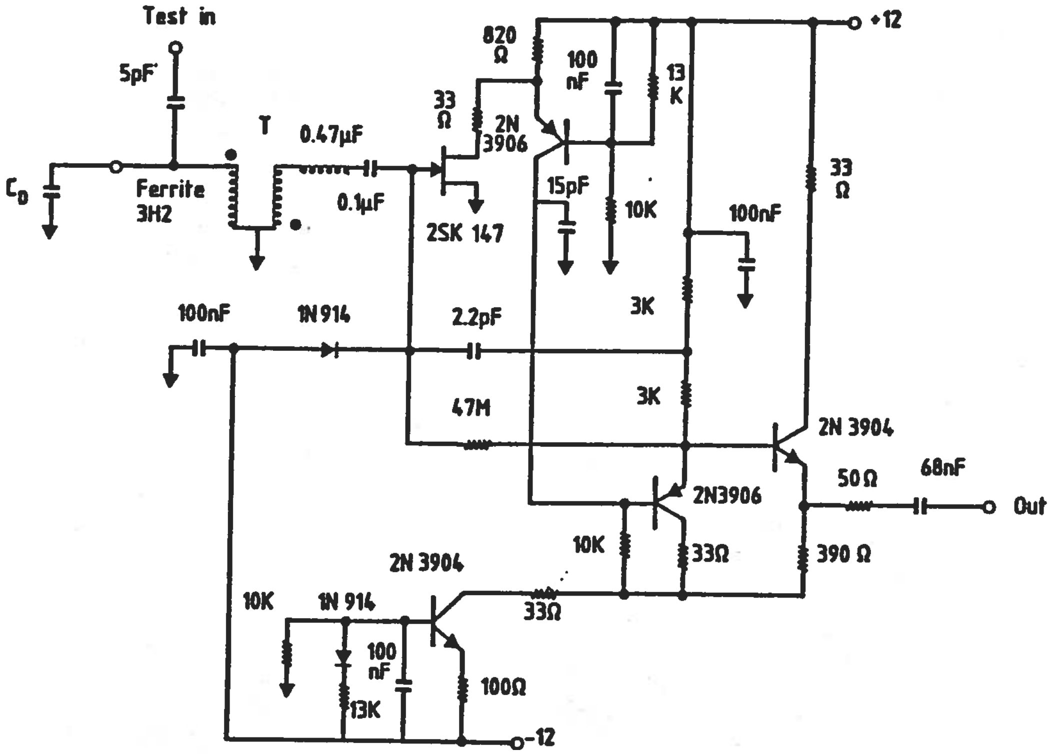

Figure 44. Low noise amplifier using large input capacitance FET.

Results are shown in Fig. 45, where one can see that starting at a minimum level of ≈ 500 electrons for small values of C_D, we observe a linear dependence on C_D of the type ≈ 2.3 electrons / pF. Measurements with a frequency spectrum analyzer have shown that the noise spectrum is "flat", corresponding to thermal noise. For a ≈1500 pF electrode capacitance this corresponds to about 3,500 electron r.m.s. noise, to be compared with the typical signal of 12,000 electrons. There are additional ways of further reducing the thermal noise. The transformer solution has been studied, as shown in Fig. 46. One can see that the practical benefits are significantly smaller than the naive theoretical expectations, mainly due to the stray capacitance of the transformer. We plan instead to :

i) operate the FET and the resistor at the front end at Liquid Argon temperature. This has been tried out and shown to work at Harvard(see Appendix II) and it should reduce the noise by as much as a factor two.

ii) to use several FET's in parallel. In order to overcome the problems associated with the spread of the gate bias voltage we plan to develop a simple custom integrated circuit with a large number of identical FET's on it, all connected in parallel and implanted on a single substrate. In this way, perhaps another factor 2 can be gained for large detector capacitances.

In this way we expect to bring down the noise level to a negligible value with respect to the minimum ionizing signal.

The signal from the preamplifiers will be digitized with flash ADC's. The recording is performed sequentially, namely the charge received between digitizations is serially stored in a memory bank. In this way the shape of the pulse from each element of the detector is recorded continuously for the duration of the drift time. As pointed out in the previous paragraph, the signal for an electron δ-function is about 0.9 μsec at the base. A variety of pulse shapes are expected for real tracks and they depend on the orientation as well the position of the event, as shown in Fig. 41. For this reason we prefer to record the complete pulse shape without filtering with a wave form analyzer technique and to perform a **digital** filtering off-line. Therefore each signal after amplification is periodically sampled by a Flash-ADC and recorded into a digital memory. A sampling frequency adequate to the speed of the incoming signals is about 4 - 5 MHz. The drift velocity of electrons for Argon and Argon-Methane

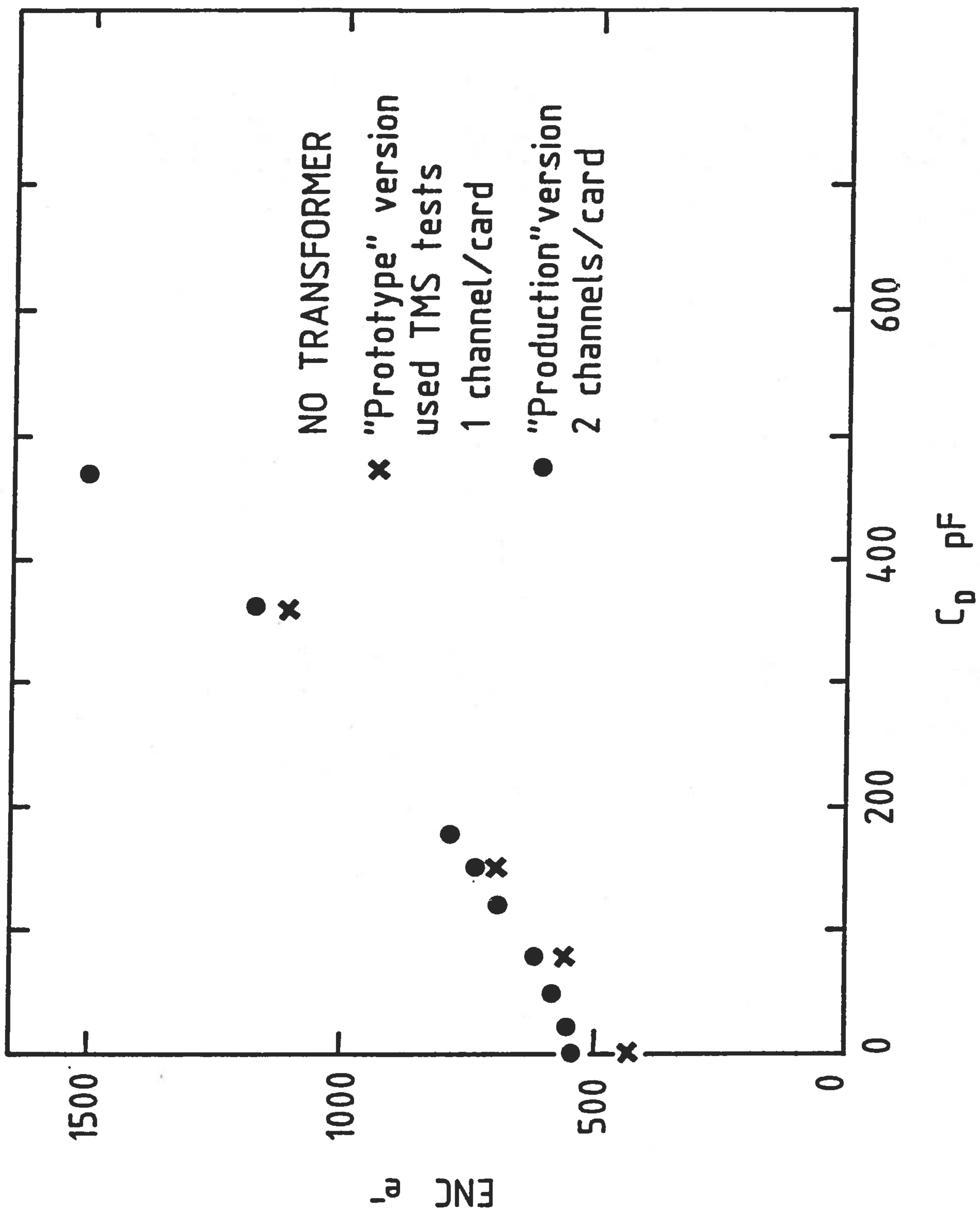

Figure 45a. Noise in dependance of detector capacitance for the amplifier of Fig. 44.

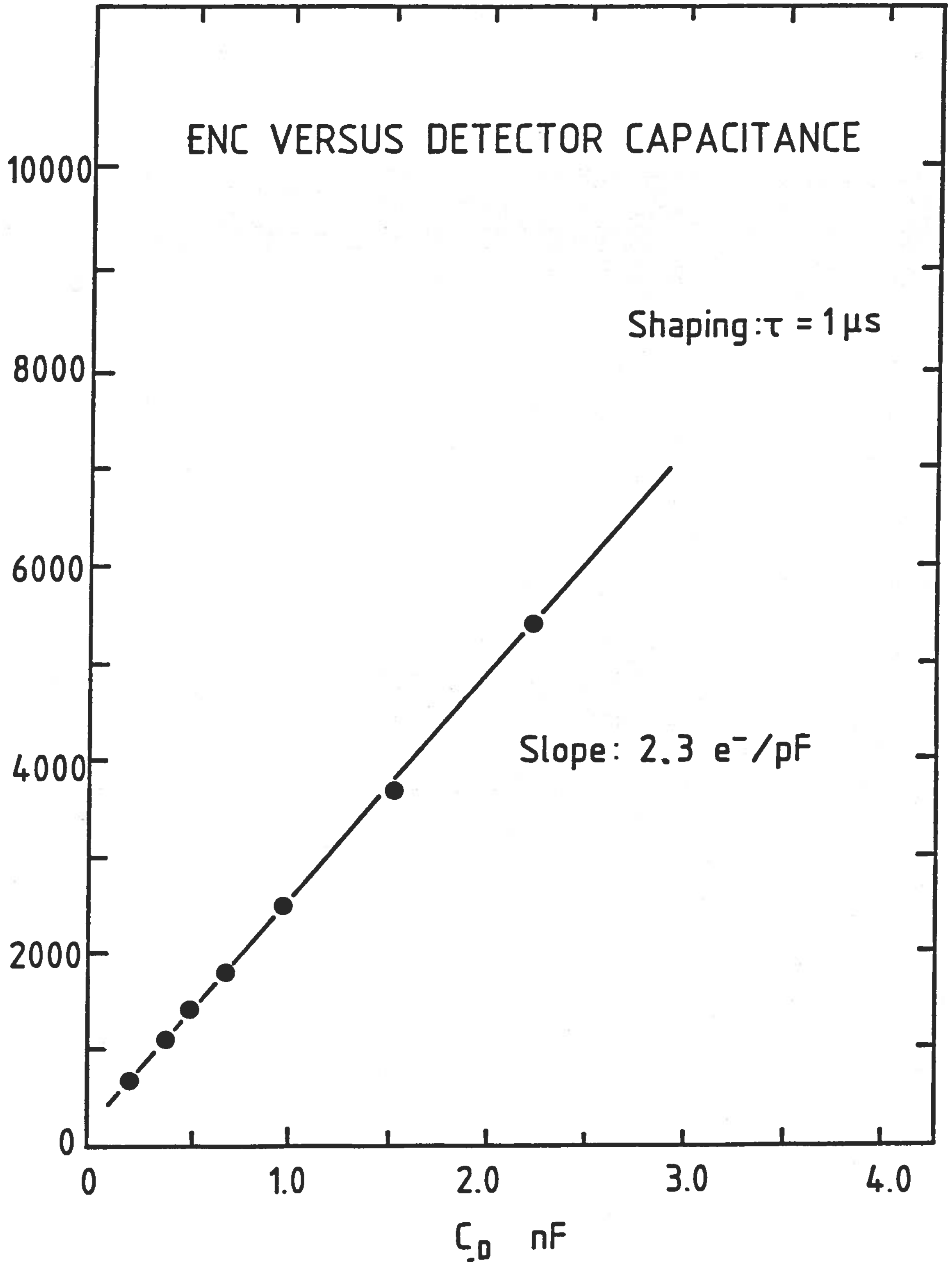

Figure 45b. The same as in Fig. 44a, except for larger values of the capacitance of the detector.

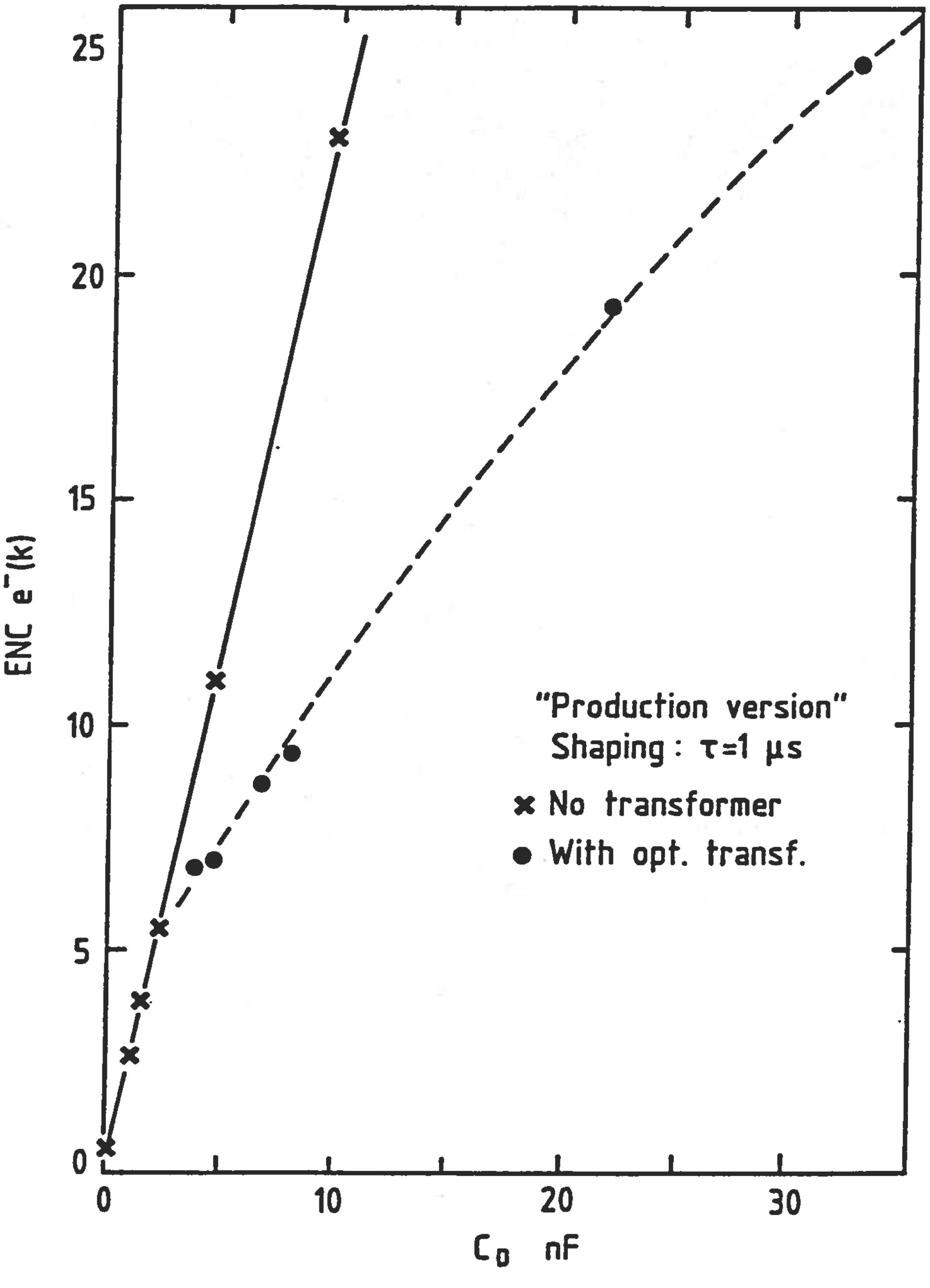

Figure 46. Effects of a matching transformer on the equivalent input noise for the amplifier of Fig. 44, a function of the detector capacitance. The transformer ratio has been optimized at each point.

mixtures is shown in Fig. 47. For a drift path of 230 cm and the slowest case of pure Argon, we need a time window of at least 1.3 msec in order to record the most distant electrons. In order to insure a reasonable safety margin we propose to use **8K memory units**, corresponding to a time window of 1.64 msec at a sample rate of 5 MHz. It would be very convenient to have two independent memory banks. In this way we can read-out the first bank while the second is active. The dead time of the read-out is then effectively zero.

We have tested a 8 bit Flash ADC model EF8308 by Thomson-EFCIS, which has a small power consumption (750 mWatt) and a speed of 20 MHz. The device has an accuracy better than 6mV at the lowest input level, 1.5 Volt for full scale. The speed of this commercially available FADC is much higher than the required digitization rate. Therefore it is advisable to multiplex several (for instance 4) input channels to a single digitizer . We arrive therefore to an over-all digitizing rate of 20 MHz and a memory size of 32 K. The read-out should remove all empty channels in order to keep the amount of information to be recorded to a sufficiently small volume.

The trigger of the event can be performed stopping the clock before the new information overrides the beginning of the event, which is about 1.6 msec after the occurrence of the event. In this amount of time a fast trigger processor must decide if the event pattern, namely energy, geometry, etc., are such as to justify its permanent recording.

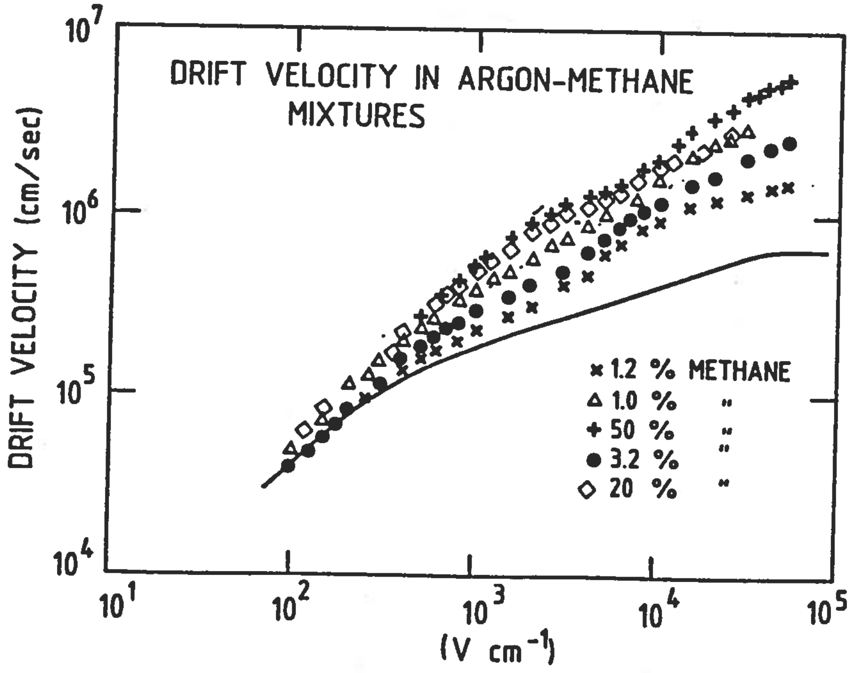

Figure 47. Electron drift velocity for Argon and Argon-Methane mixtures.

5.- The Magnet design.

The initial design of the detector has been based on the idea of using a superconducting solenoid magnet. Later considerations on the feasibility of such a large scale superconducting device and the necessity of operating it deep underground have indicated that serious problems may be encountered and that its cost could become prohibitive. Furthermore a significant fraction of the time, the experiment will be operated without a magnetic field or at a much reduced value, namely when low energy phenomena, like solar neutrinos are investigated. Finally the stray field of a 2 Tesla magnet is likely to be prohibitive for the surrounding equipment and the other experiments in the Laboratory.

For all these reasons we have finally decided that at least in an initial phase of the experiment a warm solenoid of a considerably lower field, namely 0.5 Tesla, will be constructed. The field volume proposed for the present experiment is about 7000 m^3 and it is unprecedented in the field of Elementary Particle Physics. A detailed discussion on the choice of the design parameters is therefore worth presenting.

The solenoid is 25 meter long and has a diameter of 17 meter. In order to achieve a central field value of 0.5 Tesla we must have in total $1.08 \cdot 10^7$ Ampere-turns. The material of the coil is good quality, soft Aluminum, for which a resistivity $\rho = 2.8\ 10^{-8}$ is assumed. The power dissipation is then a function of the inverse of the conductor thickness t, namely:

$$P(MW) = 6.36 / t(m)$$

where t is given in meter and the power is in MWatt. The total weight of the conductor is also a simple function of t, namely:

$$W(tons) = 3.29 \cdot 10^3 \cdot t$$

Setting $t = 0.75$ m, we find $P = 8.5$ MWatt and $W = 2470$ tons. If we put instead $t = 0.50$ m the power consumption grows to 12.7 MWatt and the conductor weight drops to $W = 1650$ tons. Clearly a cost optimization procedure must be performed as soon as the exact costs of power and of the conductors will be known for the conditions prevailing in Italy.

The current density inside the conductor is extremely low, namely $i = 0.43 / t$ (A/mm^2). For $t = 0.50$ m we find $i \approx 0.9$ (A/mm^2), or a power dissipation of 0.48 Watt/cm^3 . The thermal conductivity of Aluminum is about 2.3 Watt/cm/°C and therefore the cooling tube distribution inside the coil can be very sparse.

The number of turns depends on the parameters of the power supply. A good choice could be $I = 1.5 \cdot 10^4$ A and a corresponding voltage of 850 V for $t = 0.5$ m. The total number of turns is then 720 and the conductor cross section is 173 cm^2, corresponding to a square section of 13 x 13 cm^2.

The construction of the coil is relatively straightforward and it involves no new problems, except for its weight and the fact that it must be brought inside the tunnel through the relatively narrow tunnel. The coil can be realized in the form of several separate pancakes. Assuming that the complete coil is subdivided into 24 pancakes each about 1 m wide, the unit weight will be in the excess of 65 tons. Once vertical the pancakes are held in place by structures directly attached to the walls of the cave. There are no major magnetic forces to consider, except the pressure of the near units to each pancake. The pancakes can be either wound inside the tunnel, or alternatively brought inside in separate angular segments which are small enough to pass through the tunnel and which can then be welded in place.

The energy stored in the magnetic volume is as expected rather large, but not prohibitive, namely $2.37 \cdot 10^8$ Joules. This corresponds to the comfortable time constant of 18.8 seconds for the coil shorted on itself. The inductance is 2.42 Henry. A potentially serious problem is represented by the the huge stray magnetic field. In principle, a large underground leakage field is not harmful. However, in absence of a shield, the presence of our magnet will be felt all over the Gran Sasso Laboratory and it will be still a few Gauss at distances of the order of 300 meters from Hall "C". An iron "box" around the detector will remove this stray field. It would consist of an iron cylinder surrounding the solenoid and of a thickness of about 1.5 m. The mass of this shield will however be prohibitive, namely 15,000 tons !

In conclusion it appears entirely possible to construct a practical solenoid capable of producing a respectable field with a reasonable consumption and with a mass of conductor which although very large, is by no means prohibitive.

6.- The External Muon Detector

An external 4π detector surrounding the dewar will be used to record with good angular accuracy charged particles , in particular muons, entering or leaving the detector. By time-of-flight measurements their direction of motion can be determined. This large area (~ 4300 m^2) External Muon Detector (EMD) will be made of Resistive Plate Counters (RPC)[40] of the " double layer " type. These counters have already been tested in the Gran Sasso tunnel. A single counting rate of ~3 $/m^2/sec$ has been recorded[41] .

RPC's are fast, wireless, dc operated, low-cost counters made of parallel electrodes of high resistivity (10^{10} - 10^{11} Ω/cm). They are operated with a gas mixture of 70 % Argon and 30 % Butane at atmospheric pressure and with a strong electric field of about 50 kV/cm in the 2 mm counter gap. The efficiency of the RPC's is 99 %. The pulses have typically 100 mV height and 2.5 nsec rise-time.They are picked up by inductive aluminum strips of typically 3 cm width and 50 Ω impedance glued on the counter walls over the full length. Because of the high electrode resistivity and the large photon absorption of Butane, the electric discharge remains localized to a small region (a few 0.1 cm^2) around the primary ionization electrons. The primary electrons quickly produce in the strong electric field an avalanche followed by a localized streamer. The time resolution provided by the RPC is of the order of 1 nsec.

The EMD will form two coaxial barrels covering the dewar cylinder all around with RPC's of 1 m width and 2 cm thickness. The inner barrel, as close as possible to the outer surface of the dewar, will have a diameter of approximately 14 m; its lateral surfaces will be covered with 44 RPC's each 30 m long. The outer cylinder, as close as possible to the magnet, will have a diameter of about 18 m . Its lateral surfaces will be covered by 57 RPC's each 34 m long . The basis of both barrels will be covered with 64 RPC's of shorter length .

The 30 m and 34 m long RPC's will be made of 2 m long units, joined together on site. Then 30 m and 34 m long Al pick-up strips will be glued on. These pick-up electrodes will be read-out at the two opposite ends. By comparing the read-out times, the longitudinal coordinate of any crossing ionizing particle can be determined with an accurcy of some 5 cm. The accuracy in the measurement of the transversal coordinate is 1.5 cm for 3 cm wide pick-up strips by using a simple read-out electronic.

Problems related to security and to the mechanical support require a further detailed study.

7.- Timescale and Milestones

The experimental hall 'B' of the Gran Sasso laboratory has been completely excavated and hall 'A' has been started. Hall 'C' was completely redesigned to match the requirements of the here proposed Liquid Argon experiment. The excavation of the complete Gran Sasso Laboratory should be finished by the end of 85.

A prototype test has started at CERN to develop a 1.5 ton Liquid Argon image chamber with a total drift-length of 1.5 m and several hundred channels of read-out. The major set-up parts like dewar, power supplies, and magnet coils have been located. Results from this test are expected for the mid of 1986. All difficulties in constructing a large volume detector will be studied with this prototype. The detector will be placed in a beam-line at the CERN SC to prove that the behaviour of particles, especially low energy pions and muons, in a large image chamber is fully understood. The requirements on a large purification system will be checked.

At the same time detailed design studies on the proposed detector will be conducted. In the middle of 1986 the construction of the proposed detector should start with the winding of the magnet coils in the experimental hall and with assembling the experimental dewar. In parallel the read-out planes, the electronics, and the purification system will be developed. The full detector should be operational during 1988.

8.-Cost Estimates.

Detector Dewar (including electrodes)	2.5 M
Electronics & Read-Out	2.5 M
Storage Dewar	1.0 M
Magnet, Cooling and Power	6.0 M
External Muon Identifier	2.0 M
Cooling and Purification System	1.5 M
Argon and Methane Liquids	1.0 M
Safety	0.5 M
	17.0 M
Contigency	3.0 M
Total	20.0 M

ALL COSTS ARE GIVEN IN US DOLLARS.

9.-References.

1. C. Rubbia ; CERN-EP internal report **77-8** (1977)
2. W.A. Huffman, J.M. LoSecco and C. Rubbia, IEEE Trans.Nucl.Sci **NS-26** (1979) 64
   E.Aprile, K. Giboni and C. Rubbia, Appendix II, and paper submitted to Nucl. Instr. and Methods
3. H.H. Chen and J.F. Lathrop, Nucl. Instr. and Meth. **150** (1978) 585
   P.J. Doe, H.J. Mahler, H.H. Chen; Nucl. Instr. and Meth. **199** (1982) 639
4. A. Zichichi, The Gran Sasso Project; invited paper to the ICOMAN83, Frascati (1983)
   A. Zichichi, The Gran Sasso Project; INFN / **AE-82** / 1 (1982)
5. E. Gatti et al., IEEE Trans. Nucl. Sci. **NS-26**, (1970), 2910
6. T.A. Gabriel and B.L. Bishop, Nucl. Instr. and Meth.,**169** (1980),427
   M.S. Goodman et al., IEEE Trans. Nucl. Sci. **NS-28** no 1 (1981),524
7. T. Doke et al. "A pure Liquid Argon Calorimeter with high energy resolution for electromagnetic showers", KEK preprint and submitted to Nucl. Instr. and Methods
8. W. Fowler, Astrophys. J. **127** (1958) 551
   B. Pontecorvo, Sov. Phys. Usp. **6** (1963) 1
9. R. Davis Jr. et al., Phys. Rev. Lett. **20** (1968) 1205
10. J.N. Bahcall et al., Rev. Mod. Phys. **54** (1982) 767
11. B. Pontecorvo, Sov. Phys. JETP **26** (1968) 984
12. J.N. Bahcall et al., Phys. Rev. Lett. **28** (1972) 316
    F. Reines et al., Phys. Rev. Lett. **32** (1974) 180
13. R.T. Rood, BNL Solar Neutrino Conf. BNL **50879.1** (1978) 175
14. F.J.Kelly and H.Uberall, Phys. Rev. Lett. **16** (1966) 145
15. L.Krauss et al., HUTP-83/A076
16. P.Lagage, contributed paper to "Underground Physics", St. Vincent, Italy (1985)
17. A.Burrows, theoretical preprint, Suny, Stony Brook
18. T.K.Gaisser and T.Stanev, preprint BA-85-9
19. A.M.Hillas, Nature 312 (1984) 50
20. M.Samorski and W.Stamm, Ap. J. Lett. 268(1983)L17
21. J.Lloyd-Evans et al., Nature 305 (1983) 784

22. S.Danaher et al., Nature 289 (1981) 56
23. R.J.Protheroe et al., Ap.J. 280 (1984) L47
24. M.L.Marshak et al., preprint ANL-HEP-PR-85-19
25. G.Battistoni et al., submitted to Phys. Lett. B. (1985)
26. B. Cabrera et al., Phys. Rev. Lett. 51, 1933 (1983).
27. S. Ahlen 1983 in Magnetic Monopoles, R. A. Carrigan and W. P.Trower,Eds., Plenum: New York, N. Y.
28 B. Price et al., Phys. Rev. Lett. 52, 1265 (1984).
29. E. Parker, Astrophys. J. 160, 383 (1970).
30. Raphaeli and Turner, Phys. Lett. 121B, 115 (1983).
31. J. Harvey, M. Ruderman and J. Shaham, Columbia University preprint (1985).
32. See for example, M. Turner, FNAL preprint CONF 85/72A, 1985.
33. C. Goebel, Proceedings of the Monopole Seminars, U. of Wisconsin, 1981, edited by D. Cline, p. 51.
34. We thank Prof. Cabibbo for pointing out to us such a fundamental property of the Euclidiean Geometry.
35. J. Arafune and M. Fukugita, Phys. Rev. Lett. 50, 1901 (1983).
36. Il traforo del Gran Sasso, ANAS and Cogefar editors, (1979)
37. Campo Venuti et al. , Frascati Internal report LNF 82/78
38. E. Fiorini, private communication, March 1985
39. E. Gatti et al . IEEE Trans . Nucl. Sci. **NS-26** (1970) 2910
    O. Bunemann et al. Can. J. Res. **27** (1949) 191
40. R. Santonico and R. Cardarelli; Nucl Instr. and Meth. **187** (1981) 377
41. M. Bertino, R. Cardarelli, L. Dicaccio, A. Lucci and R. Santonico; Nota Interna n.**788** IFU, Rome (1982)
    M. Conversi; Hadronic Journal **6** (1983) 1103; and invited talks to the workshop "Science Underground", Los Alamos (1982); "8th European Cosmic Ray Symposium" Rome (1982); Technoprint Bologna (1983) 159

APPENDIX I. SAFETY ISSUES.

Table of contents.

1.-Introduction.

The main hazard of operation of the underground experiment is associated with the presence of the huge amount of cryogenic liquids. They can vaporize in contact with warm parts of the detector and cause the release of massive amounts of cold gases. In the initial mode of operation these gases will be inert and non toxic. However they can impair visibility because of the formation of condensation of the humidity of the air in form of fog. They are exceedingly cold, thus affecting muscular activity. Finally, if in huge amounts, they can reduce the fraction of Oxygen in the atmosphere below a vital minimum. In a second phase of experiments, liquefied Argon may be partially or totally replaced by liquefied Methane, thus adding to the dangers the one of explosive gases.

In order to insure a completely safe operation of the underground detector we shall follow a number of clear guidelines :

(1) During operation with cold liquids, the cryogenic cave and the main tunnel are geographically very distant and hermetically separated. No gas mixing can occur under any circumstance. Thick, multiple, pressure holding doors are the key to this scheme.

(2) The cryogenic cave can resist to large gas overpressures safely and for an indefinite period of time. Its pressure boiler's shape and the strength and the compactness of the rocks out of which the laboratory is constructed insure containment of any conceivable pressure within the volume of the cave. Deep underground, high pressures are a very common natural phenomena. For instance the unperturbed water pressure at our depth was in excess of 60 atm. In case of an "ultimate disaster scenario" we must assume, that somehow the totality of the cryogenic liquid inside the cave evaporates instantly. This corresponds to an overpressure of 20 atm. of cold (100 °K) gas which must be safely contained and disposed.

(3) The recovery from an accidental pressurization of the cave is performed with the help of a vertical, independent exhaust pipe, connected directly to the top of the mountain. The pipeline, of the type used for extracting natural gas and oil can of course handle safely the large pressure drop and the huge gas flow. Even in the most concerning case of the loss of the

pure Methane filling, considerable experience exists, since the natural gas industry handles safely every day amounts of Methane gas which are much larger than the one considered here and at much higher pressures.

(4) Human access to the main cave will be severely restricted during the periods with cryogenic liquids. In the case of Methane, it may be advisable to remove most of the Oxygen of the cave, flushing out the air in the cavity with Nitrogen or Argon. Air can be established in few hours before access, with the help of the ventilation of the tunnel, capable of providing as much as 80,000 m^3/hour of fresh air. During the flushing operations, the air-inert gas mixtures can be evacuated through the exhaust pipe or if in not too large quantity, dumped directly in the tunnel, after diluting it with many volumes of fresh air in order not to impair the quality of the underground environment.

2.-Emission of cold gases.

Liquid Argon at normal pressure boils at a temperature of 87.3 °K. The latent heat of evaporation is 39 cal/gr, corresponding to 163 J/gr. The critical point is at 150 °K and a pressure of 48 atm. Normal operation is quite close to the triple point, T_t = 84 °K, p_t = 0.67 atm. Therefore the Argon can be easily solidified at a temperature of 83 °K, with a considerable increase of density, from d_{liq} = 1.42 gr/cm^3 to d_{solid} = 1.62 gr/cm^3. The melting heat is modest, 7 cal/gr corresponding to 29 J/gr.

The possibility of an accidental freezing out of the Argon has to be considered very carefully, since it may become a source of safety hazard. In fact due to the large decrease in density it might produce stresses on the piping system. If a significant amount of liquid comes into contact with room temperature materials, instant vaporization occurs. The heat available in these materials is typically 0.83 J/ °C/gr for rock or concrete and 0.46 J/ °C /gr for steel. Integrating the heat capacity from room temperature to 87.3 K° we find that each gram of rock or steel has enough heat to vaporize either 1.0 gr or 0.55 gr of Liquid Argon, respectively. Since the mass of material inside the cave is very large, a massive spill of liquid can lead to a considerable vaporization. The effect of the surrounding rocks can be considerably reduced with even a modest insulation coating. Cheap, styrofoam based insulators have a heat leak of about 10 Watt/m^2 between Liquid Argon and room temperatures. Assuming that the walls of the cave are coated all around and that 3000 tons of liquid are spilled out of the detector dewar into the inside of the cave such as to fill its lowest 4 meters, over the 1100 m^2 of isolation we bring in enough heat as to vaporize only 0.24 tons/hour, which is negligible when compared with the contact vaporization. Convection effects and thermal contact of the cold gas within the cave are relatively slow and the cave will pressurize and cool down rapidly. The empty volume of the cave is 30,000 m^3. The density of cold (100 °K) Argon gas is about 5 gr/ cm^3 and and vaporization of 100 tons of Argon will rise the internal pressure of the cave by 0.67 atm. Complete, instantaneous vaporization of 3000 tons of Argon would then rise the internal pressure to 18 atm. Of course this eventuality is only hypothetical. Assuming a complete spill and 150 tons of unshielded material, we expect an initial rise of 1 atm, followed by a slow build up due to conduction over the total 5200 m^2 of the walls of the cave of 52 kWatt, corresponding to a vaporization rate of 1.15 ton/hour or a pressure rise of 1 atm in 130 hours, provided of course that no exhaust facility is operational. However, **no matter how improbable the complete vaporization might be we shall take it as reference for evaluating the ultimate safety requirements.** Therefore the exhaust system must be capable of disposing in a relatively short time and safely an overpressure of about 18 atm of gas at the temperature of 100 °K.

3.-Exhaust of cold gases.

The cold gas is evacuated through a 1.5 km long steel pipe connecting the cave to the top of the mountain. The flow J in turbulent flow regime is given by:

$$J = d \left\{ \frac{\pi^2 \, 20}{16 \cdot 3.2} \; \frac{d^3 (p_0^2 - p_2^2)}{2 \cdot L} \right\}^{4/7} (R \, T_0)^{3/7} \left(\frac{4}{\pi \, \eta} \right)^{1/7}$$

where J is the gas flux in volume · pressure,

d is the tube diameter ,

p_0 and p_2 are the initial and final pressures,

L is the tube length,

h is the viscosity coefficient, which for Argon at room temperature is 209.6 mpoises; it drops to 70 mpoises-180 °C (for air it is 62.7 mpoises at -180 °C)

Inserting numerical coefficients we find:

$$J = C\, d \left\{ \frac{d^3}{L} \, \frac{(p_0^2 - p_2^2)}{2} \right\}^{4/7} \qquad \mathrm{Torr\,.\,l/s}$$

where units for d and L are cm, p are in Torr and the coefficient C has different values according to the gases, namely :

$C =$ 140. for Air at $T = 20^{o}\mathrm{C}$
81.4 for Air at $T = 90\ ^{o}\mathrm{K}$
144. for Argon at $T = 20\ ^{o}\mathrm{C}$
84.2 for Argon at $T = 90\ ^{o}\mathrm{K}$

Setting now the initial pressure to 20 atm = $1.52\ 10^4 \cdot$ Torr, $L = 1.4 \cdot 10^5$ cm $d = 50$ cm and for cold Argon we find $J = 1.6 \cdot 10^8$ Torr l/s, equivalent to a flux of 14.0 $\mathrm{m^3/sec}$ of evacuated material and to a 1/e decay time of less than one hour. For the more realistic alternative of an overpressure of 1.0 atm and $T = -\ 50\ ^{o}\mathrm{C}$ for an equal mixture of air and Argon we find $J = 7.99\ 10^7$ Torr l/s, equivalent to a a flux of 8.6 $\mathrm{m^3/sec}$ or a 1/e decay time for the pressure of 30 minutes.

4.-Computer simulations.

The phenomenology inside the cave in case of an accidental spill of liquid can be accurately simulated with the help of computer programs. In the "model" we have assumed that because of an accidental spill out a certain amount of Liquid Argon is spilled on warm surfaces and it evaporates immediately upon contact. It is assumed that these components reach rapidly the temperature of the liquid Argon. In addition there is a source of heat flow from the outside world (20 ºC) of a specified amount which produces additional Argon boil-off. The cold Argon gas mixes with the warm air inside the cave and it comes in contact with other hot parts of the apparatus which further warms up the gases,increasing the pressure. There is very little or no heat contact, apart from convection, between the Liquid Argon and the cold gas in the cave in order to cool it back down. The exhaust pipe has been approximated with the classic formulae for turbulent flow. The viscosity coefficient, takes into account the temperature and the composition of the gas mixture. We may either assume that a fraction of the Argon has safely stored in the back-up dewar, or that the totality of the Argon has been spilled inside the cave.

In the simplest approximation a large quantity of Argon is spilled and instantly vaporized inside the cave. The pressure decay curves are shown in Fig.48, where

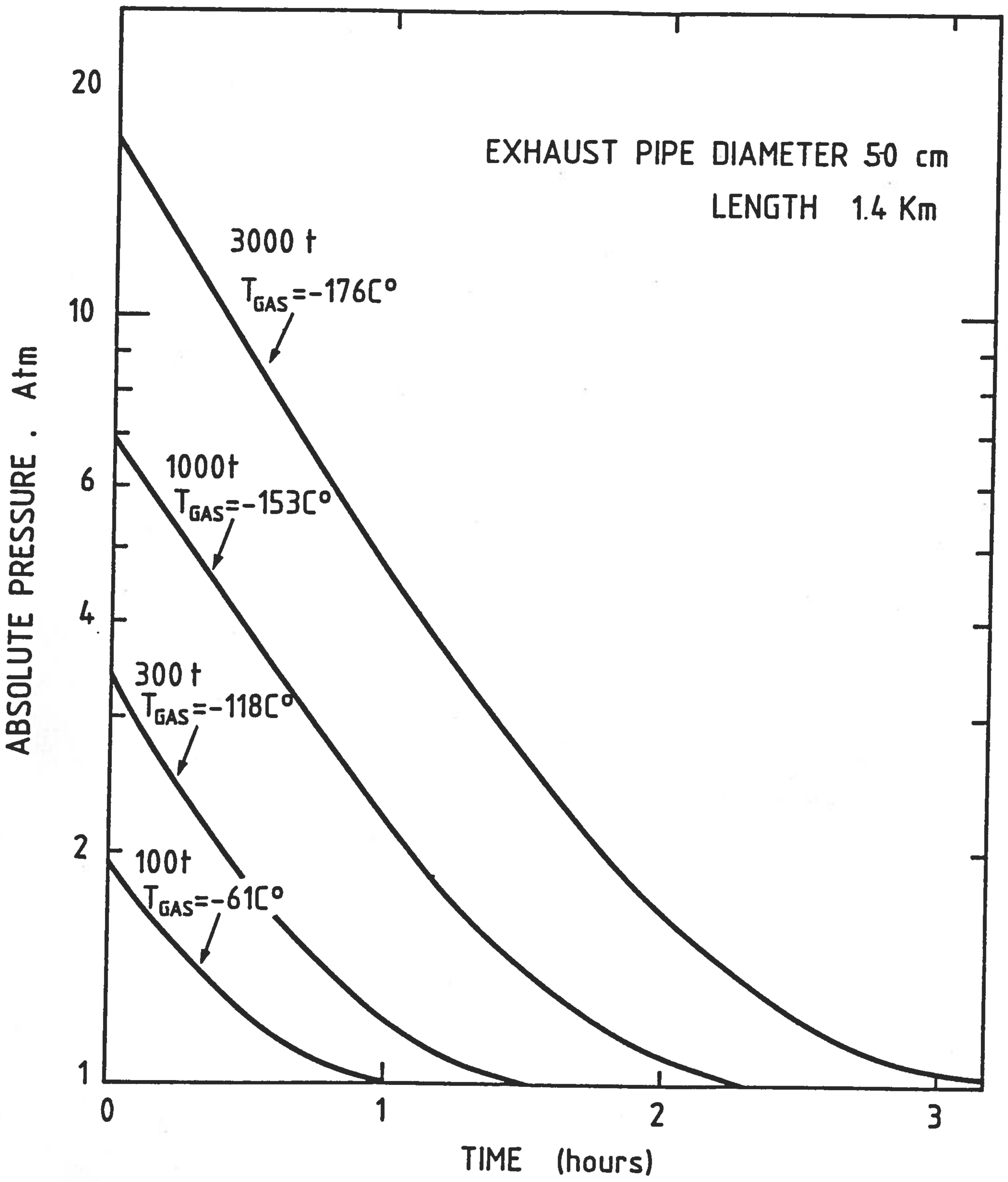

Figure 48. Decay of the pressure with time in the case of instant evaporation of all the spilled liquid. The pressure curve depends on the amount of liquid.

one can also see that the ejected gas becomes progressively colder for larger spills. Whilst a 100 tons spill can be dissipated in less than one hour, the loss of all the 3000 tons with complete and instant vaporization needs about three hours. The initial maximum pressure is then about 18 atm. This calculation does not take into account the origin of the heat supply.

A more sophisticated approach, shown schematically in Fig. 49, assumes warm parts which supply instantaneous heat (e.g. 150 tons of concrete + steel) in contact with the liquid and a number of massive warm components in contact with the gas after vaporization (e.g. 50 tons of steel). A massive heat flow from the outside keeps evaporating the Argon at a fast rate. Pressure decay curves are shown in Fig. 49, where one can see a rapid rise until all the Argon has evaporated followed by a decay. Very large amount of heat must be supplied in order to vaporize all the liquid in a few hours. Heat supplies in excess of 300 MWatt are equivalent to instant vaporization and produce the maximal pressure rise of about 18 Atm. Lower heat supplies produce longer transition curves. For instance at 75 MWatt input heat supply, the Argon is boiled off in about two hours at a peak pressure rise of 8.6 atm (Figure 49). Note that even the most rudimentary insulation on the walls of the cave gives a heat supply as low as 10 Watt/m^2. Therefore, unless a massive destruction of the insulation has occurred, only a few kWatt (namely a heat flow three orders of magnitude smaller) are generated by the walls of the cave. In this case, after an instantaneous vaporization of few hundred ton of Argon, due to the contact with warm parts of the cave (raising the pressure to a few atmospheres) followed by a short recovery the pressure drops to very low values and the liquid will remain in the cavity for a very long time, slowly boiling away for many weeks. Indeed, the main problem is now how to vaporize the remaining liquid!

During a spill-out the temperature in the cave drops considerably and it approaches the one of the liquid Argon (Fig. 50). It is not easy to bring it back to normal temperature, unless a large controllable heat flow is provided. A heating system capable of supplying about 20 MWatt is recommended in order to recondition the cave and to insure a safe access after a reasonable period of time. It could be derived from the abundant water supply inside the cave, with an heat exchanger in order to avoid freezing. Also some of the air of the tunnel must be forced through the cave and the exhaust pipe before human access after an emergency.

In conclusion it appears that even the most catastrophic events in the cryogenic cave can be safely handled.

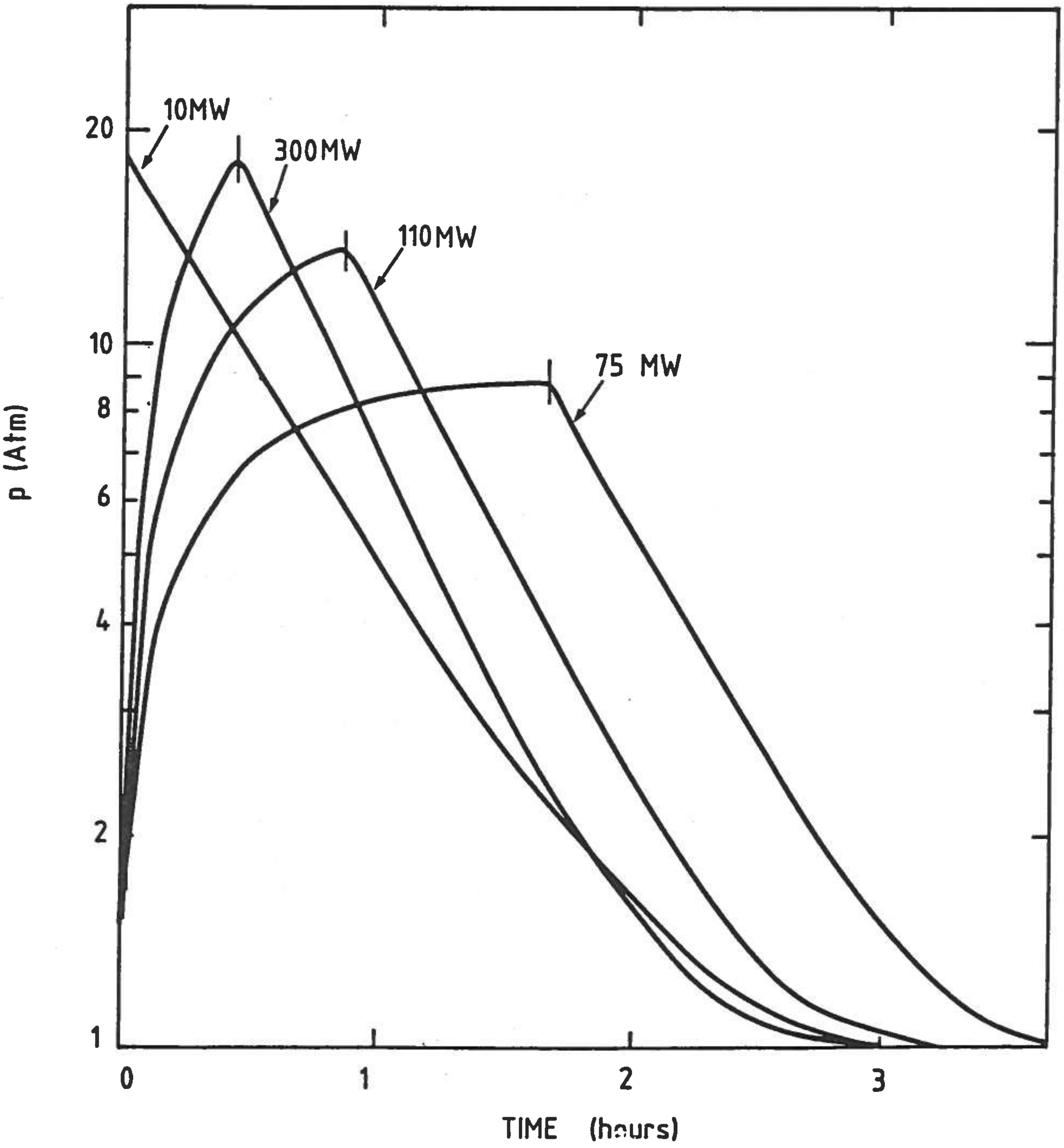

Figure 49. Pressure in the cave in dependance of time after the spill considering different limited heat supplies to evaporate the liquid.

5.-Methane fillings.

During the second phase of the experiments we intend to replace either completely or partially the Argon with Methane. Methane gas, when mixed with Air is explosive in the range from 5% to 15%. The parameters of Methane are compared with the ones of Argon in Table 9.

Table 9. Main Parameters of Argon and Methane.

Quantity		Methane	Argon
Boiling Point	K	111.7	87.3
Melting Point	K	90.7	84.0
Density, Liquid	kg/l	.425	1.394
Density,Gas/Air		.555	1.38
Vaporization Enthalpy	kJ/mole	8.18	6.18
Melting Enthalpy	kJ/mole	.941	1.19
Heat capacity @ 25 C	J/K/mole	27.43	12.47

One can see that there are relatively small differences in the relevant parameters. Therefore most of the conclusions for Argon remain valid both for pure Methane and for Methane-Argon mixtures. Of course, if the content of Methane in the detector exceeds the 10%, mixing with air may reach the condition of explosive mixture. It is therefore advisable to replace the air of the cave with inert gas, either Argon or Nitrogen prior to the utilization of the explosive mixtures. Note that a similar precaution has been taken by the BEBC chamber group with large amounts of Liquid Hydrogen at CERN. We do not envisage major problems disposing massive amounts of Methane through the exhaust pipe. Note that even a major explosion in the detector cave can be buffered if a "muffler" arrangement is situated in the access gallery. Of course we do not see how such an explosion could ever take place if the precautions indicated here are followed.

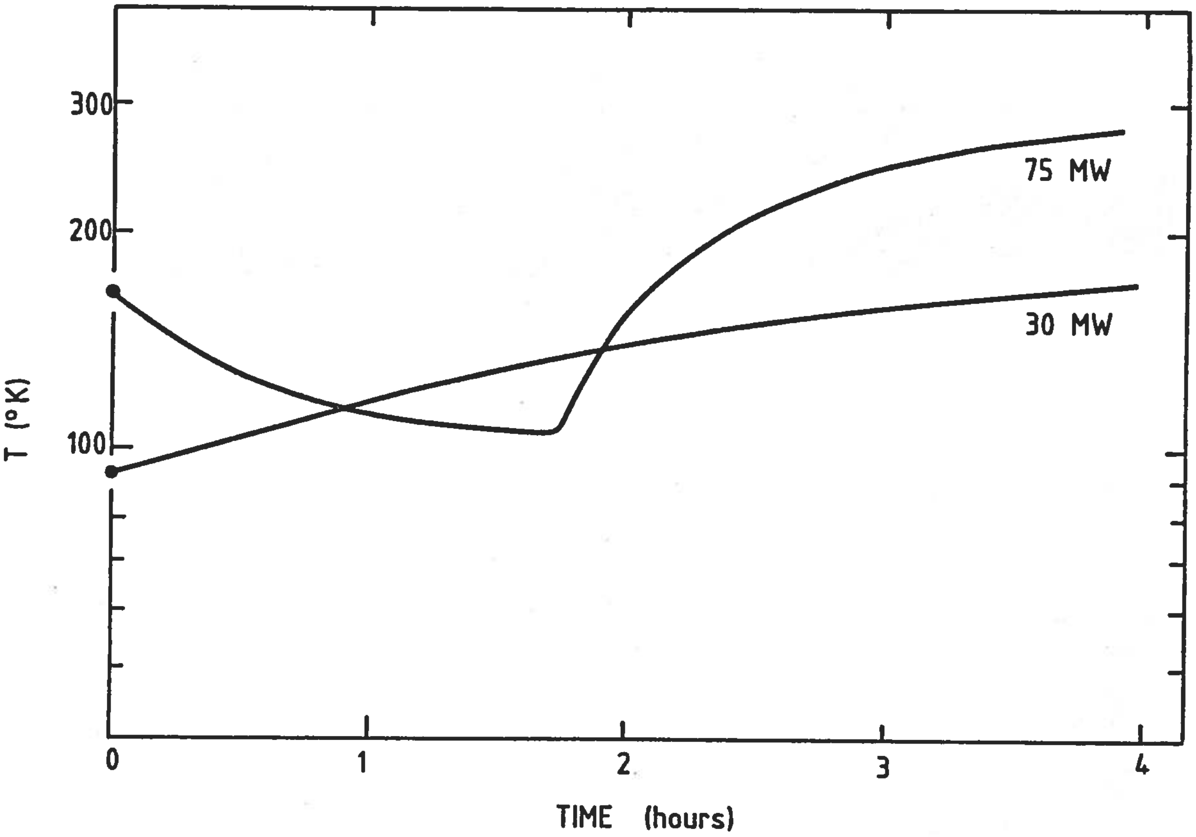

Figure 50. Time dependance of the temperature in the cave after a spill.